# INDUCED CURRENT MEDICAL ELECTRO-THERMAL IMAGING

A THESIS SUBMITTED TO
THE GRADUATE SCHOOL OF NATURAL AND APPLIED SCIENCES
OF
MIDDLE EAST TECHNICAL UNIVERSITY

BY

VOLKAN TANRIVERDİ

IN PARTIAL FULFILLMENT OF THE REQUIREMENTS
FOR
THE DEGREE OF DOCTOR OF PHILOSOPHY
IN
ELECTRICAL AND ELECTRONICS ENGINEERING

JANUARY 2024

Approval of the thesis:

## INDUCED CURRENT MEDICAL ELECTRO-THERMAL IMAGING

submitted by **VOLKAN TANRIVERDİ** in partial fulfillment of the requirements for the degree of **Doctor of Philosophy in Electrical and Electronics Engineering Department, Middle East Technical University** by,

Prof. Dr. Halil Kalıpçılar
Dean, Graduate School of **Natural and Applied Sciences**

Prof. Dr. İlkay Ulusoy
Head of Department, **Electrical and Electronics Engineering**

Prof. Dr. Nevzat G. Gençer
Supervisor, **Electrical and Electronics Engineering, METU**

**Examining Committee Members:**

Prof. Dr. Yusuf Ziya İder
Biomedical Eng., Başkent University

Prof. Dr. Nevzat G. Gençer
Electrical and Electronics Eng., METU

Prof. Dr. Cengiz Beşikci
Electrical and Electronics Eng., METU

Assoc. Prof. Dr. Yeşim Serinağaoğlu Doğrusöz
Electrical and Electronics Eng., METU

Assoc. Prof. Dr. Emine Ülkü Sarıtaş Çukur
Electrical and Electronics Eng., Bilkent University

Date: 24.01.2024

**I hereby declare that all information in this document has been obtained and presented in accordance with academic rules and ethical conduct. I also declare that, as required by these rules and conduct, I have fully cited and referenced all material and results that are not original to this work.**

Name, Last name : Volkan Tanrıverdi

Signature :

# ABSTRACT

## INDUCED CURRENT MEDICAL ELECTRO-THERMAL IMAGING

Tanrıverdi, Volkan
Ph.D., Department of Electrical and Electronics Engineering
Supervisor: Prof. Dr. Nevzat G. Gençer

January 2024, 120 pages

Breast tumors generate more metabolic heat than surrounding healthy tissues. However, detecting deep tumors using infrared (IR) imaging is challenging. This study proposes creating induced currents by applying a time-varying magnetic field to the tumorous breast since an additional temperature contrast occurs due to the electrical conductivity and specific heat differences between the tumors and healthy tissues. The main objectives are: 1) to investigate the feasibility of the method for surface and deep tumors with numerical studies and 2) to demonstrate the use of this method through different experiments conducted with phantoms that mimic breast tissues.

Tumorous breasts were modeled numerically, and the active and passive modes were simulated in three dimensions. In simulation studies, the induced current altered the temperature contrast on the imaging surface, resulting in a 4 mm increase in tumor detection sensitivity. An 11-turn, 70 mm long solenoid coil was constructed for the experimental studies, and a 20 A current was applied at 745 kHz. A temperature difference of up to 0.4 °C in the tumor location was observed compared with the absence of the tumor. Similarly, a 23-turn multilayer coil was utilized in serial resonance at 755 kHz with a 3.75 A current, and a 0.4 °C temperature difference at the tumor location was observed. It was concluded that the temperature contrast on the body surface changed, and the tumor detection depth increased with the induced currents in breast IR imaging. The proposed method was validated using in vitro experiments.

Keywords: Active Thermography, Breast Cancer, Breast Thermography, Infrared Imaging, Electro-Thermal Imaging

# ÖZ

## AKIM İNDÜKLEMELİ TIBBİ ELEKTRO-TERMAL GÖRÜNTÜLEME

Tanrıverdi, Volkan
Doktora, Elektrik ve Elektronik Mühendisliği Bölümü
Tez Yöneticisi: Prof. Dr. Nevzat G. Gençer

Ocak 2024 , 120 sayfa

Meme tümörleri, çevresindeki sağlıklı dokulardan daha fazla metabolik ısı üretir. Bununla birlikte, derindeki tümörleri kızılötesi (IR) görüntüleme kullanarak tespit etmek zordur. Bu çalışma, tümörler ile sağlıklı dokular arasındaki elektriksel iletkenlik ve spesifik ısı farklarından dolayı ek bir sıcaklık kontrastı oluştuğundan, tümörlü memeye zamanla değişen bir manyetik alan uygulanarak indüklenen akımların oluşturulmasını önermektedir. Temel amaçlar şunlardır: 1) yüzeydeki ve derindeki tümörler için yöntemin uygulanabilirliğini sayısal çalışmalar ile araştırmak ve 2) farklı deneylerle, meme dokularını taklit eden fantomlar kullanarak yöntemin kullanımını göstermek.

Tümörlü göğüsler sayısal olarak modellendi ve aktif ve pasif modlar üç boyutlu olarak benzetildi. Benzetim çalışmalarında, indüklenen akım, görüntüleme yüzeyindeki sıcaklık kontrastını değiştirdi ve tümör tespit hassasiyetinde 4 mm'lik bir artışa neden oldu. Deneysel çalışmalar için 11 sarımlı 70 mm uzunluğunda bir solenoid bobin üretildi ve 745 kHz'de 20 A akım uygulandı. Tümörün olmadığı duruma kıyasla tümörün bulunduğu lokasyonda 0.4 °C'ye kadar sıcaklık farkı gözlemlendi. Benzer şekilde, 3.75 A akım ile 755 kHz'de seri rezonansta 23 sarımlı çok katmanlı bir bobin kullanıldı ve tümör konumunda 0.4 °C'lik bir sıcaklık farkı gözlemlendi. IR meme görüntülemede, indüklenen akımlar ile vücut yüzeyindeki sıcaklık kontrastının değiştiği ve tümör tespit derinliğinin arttığı sonucuna varıldı. Önerilen yöntem, cansız deneyler yapılarak doğrulanmıştır.

Anahtar Kelimeler: Aktif Termografi, Meme Kanseri, Meme Termografisi, Kızılötesi Görüntüleme, Elektro-Termal Görüntüleme

To my family

# ACKNOWLEDGMENTS

This study was conducted under the supervision of Prof. Dr. Nevzat G. Gençer. I would like to express my deepest gratitude for his endless guidance, criticism, and support throughout this study. It has been a great privilege and experience working with Prof. Dr. Nevzat G. Gençer.

I would also like to express my sincere appreciation to Ph.D. thesis monitoring members, Prof. Dr. Y. Ziya İder and Assoc. Prof. Dr. Yeşim Serinağaolu Doğrusöz for their valuable and significant guidance throughout the study.

Finally, I would like to express special appreciation and gratitude to my family for their support. I would not have been able to complete this study without their endless patience.

# TABLE OF CONTENTS

CHAPTERS

APPENDICES

# LIST OF TABLES

TABLES

# LIST OF FIGURES

FIGURES

# LIST OF ABBREVIATIONS

| ABBREVIATIONS | |
|---|---|
| 2-D | Two Dimensional |
| 3-D | Three Dimensional |
| ACS | American Cancer Society |
| AC-ETI | Applied Current Electro-Thermal Imaging |
| EIT | Electrical Impedance Tomography |
| FEM | Finite Element Method |
| FIR | Far Infrared |
| FPA | Focal Plane Array |
| HD | Heterogeneous Dense |
| ICNIRP | International Commission on Non-Ionizing Radiation Protection |
| IC-ETI | Induced Current Electro-Thermal Imaging |
| IEC | International Electrotechnical Commission |
| IR | Infrared |
| IRT | Infrared Thermography |
| LWIR | Long-Wave Infrared |
| MF | Magnetic Field |
| MIT | Magnetic Induction Tomography |
| MRI | Magnetic Resonance Imaging |
| MWIR | Medium-Wave Infrared |
| NDT | Non-Destructive Testing |
| NETD | Noise Equivalent Temperature Difference |

| | |
|---|---|
| NIR | Near Infrared |
| PET | Positron Emission Tomography |
| QWIP | Quantum Well Infrared Photodetector |
| RF | Radio-Frequency |
| RGB | Red Green Blue |
| SAR | Specific Absorption Rate |
| SFG | Scattered Fibroglandular |
| SWIR | Short-Wave Infrared |
| TVDT | Tumor Volume Doubling Time |
| US | Ultrasonograph |
| WHO | World Health Organization |

# CHAPTER 1

# INTRODUCTION

Medical infrared (IR) imaging has emerged as an alternative breast imaging method with the potential to overcome some drawbacks of standard imaging techniques [1]. IR imaging is portable, non-ionizing, comfortable, and more economical than other methods and provides information on the tissue's thermal conditions [2]. In IR imaging, a thermal sensor array obtains radiation from a body surface [3]. Tumorous tissues produce higher metabolic heat than healthy tissues, and this heat source generates a temperature contrast on the body surface [4]. However, early diagnosis depends on the tissue characteristics (malignant tumor size, tumor location, and surrounding tissues) and camera parameters (sensitivity and spectral bands). Thermal imaging techniques that use different energy sources, such as optical or electrical, have been used to enhance IR imaging detection capabilities via hybrid imaging methods.

This thesis examines a novel approach to active medical IR imaging. In the Introduction section, we present the motivation for this thesis, the proposed method, the contributions and novelties, breast cancer and its imaging modalities, breast thermography with its historical background, active medical IR thermography, electro-thermal imaging, applications of induced current active thermography, dielectric properties of the breast, and the relevant literature.

## 1.1 Motivation of the Thesis

Depending on their type and overall health, body tissues have varying electrical properties, including conductivity, permittivity, and thermal parameters. Implementing electromagnetic fields above the body's surface and inducing currents within the body tissue can enhance the diagnostic ability of standard IR imaging. Simultaneously, tumors can be detected at greater depths using thermal IR imaging.

The objective of the imaging method in this study was to enhance the temperature difference created by the formation of malignant tissue in typical IR imaging by applying electromagnetic fields while maintaining non-contact imaging characteristics. The externally induced heat was lower within the tumor and at the boundary on the imaging side, owing to perturbations in the induced current related to the differences in electrical conductivity and permittivity. Moreover, malignant tumorous tissue experienced a lower temperature increase than healthy tissue owing to its lower specific heat capacity. Considering the local specific absorption rate (SAR) and temperature safety limits, this additional temperature difference enhanced the diagnostic capabilities of standard medical IR imaging and confirmed the presence of tumors.

## 1.2 Proposed Method

We propose the Induced Current Electro-Thermal Imaging (IC-ETI) method to improve the temperature contrast generated by malignant tumors in standard breast IR imaging. This can be achieved by inducing currents in the body using time-varying electromagnetic fields and recording the thermal distribution.

Induced currents have previously been studied for non-destructive testing applications in the industry. In this study, we investigated the behavior of the induced currents for diagnostic purposes, focusing on breast cancer detection. This is the first study exploring IC-ETI's use in medicine through simulation and experimental studies.

A block diagram of the IC-ETI method is illustrated in Figure 1.1. We have recorded the temperature distributions on the breast surface under both the passive and active conditions.

In the passive mode, the temperature distribution primarily arises from the metabolic heat sources within the breast. In the active mode, the electrical currents induced by the coils near the breast change the temperature distribution in addition to metabolic heat sources and thermal parameters. The IC-ETI method uses the refraction (per-

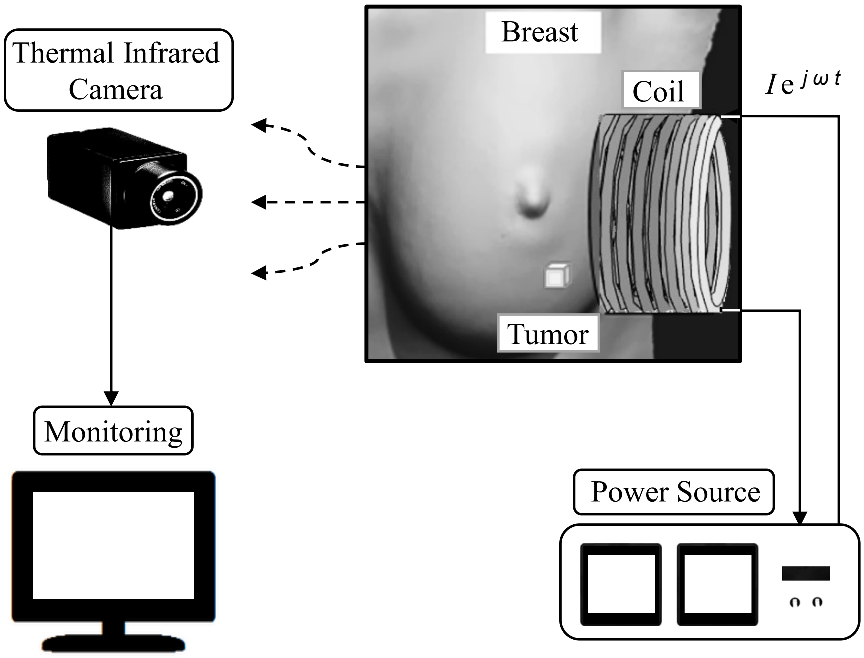

Figure 1.1: IC-ETI method for breast cancer detection. IR images are recorded in active and passive modes. In active mode, a sinusoidal current with angular frequency $\omega$ $(\mathrm{rad/s})$ is applied to the coil to induce an electrical current inside the breast [5].

turbation) of the induced current around a more conductive tumor. The temperature increase varied on and around the tumor, owing to the induced current distribution and specific heat properties.

## 1.3 Contributions and Novelties

The contributions of this study are as follows:

- This study demonstrated the theory and feasibility of a novel medical active thermal imaging technique, IC-ETI, for breast tumor detection using induced current refraction and breast tissue parameters.

- Multiphysics simulations of a three-dimensional (3-D) tumorous breast model were performed using COMSOL software. The performance and sensitivity of the IC-ETI method were investigated by numerically simulating in vivo conditions based on local SAR and temperature limits.

- The simulation studies investigated changes in temperature distribution using in vivo breast tissue parameters, simple coil geometries, and sinusoidal current excitations.

- Two circular coil configurations were specifically designed and implemented for the simulation studies, and these coils were excited in serial resonance to implement the IC-ETI method.

- Tumorous breast phantoms were created using gelatin-based and mashed potato-based materials, and their conductivities were determined using two different measurement methods. The results of the three experiments were compared to validate the IC-ETI method.

- Finally, experiments were performed to confirm the simulation results' accuracy and demonstrate the IC-ETI method's feasibility.

## 1.4 The Outline of the Thesis

Chapter 2 introduces the theory of IC–ETI, covering electromagnetic and thermal issues in detail, and discusses Pennes' Bio-heat equation for the breast. This chapter presents a theory of IR radiation and explains how the refraction of the current density vector changes the power distribution in and around the tumor.

Chapter 3 describes the numerical breast model and presents the simulation results, including the temperature distribution of the breast tumor. This chapter includes results from 3-D simulations and related experimental simulations, including simulations of current density refraction.

Chapter 4 provides information on the experimental studies, including a detailed explanation of the experimental setup, excitation coil, resonant circuit, and tumorous phantom used. This section discusses an analysis of the results of the tumorous breast phantom images.

Chapter 5 provides a thesis summary, a discussion section, and an outline of future work.

## 1.5 Breast and Breast Cancer

The 3-D breast structure and its layers housing a tumor are illustrated in Figure 1.2b. The breast is primarily composed of the mammary glands and fat tissues. It comprises lobules that produce milk and is surrounded by fatty tissue. The breast lobules are empty in the duct and nipple tissues, as shown in Figure 1.2a.

Breast cancer expansion generally begins in lobule tissues or milk ducts. Breast cancer is described by abnormal cell growth in breast tissue. Breast cancer can spread to vital organs. Breast cancer is a type of cancer that is commonly diagnosed among women in the USA, accounting for 30% of all cancers. Lung and bronchus cancers follow this at 13%, and colon-rectal cancers at 8% [7]. 2.3 million new breast cancers and 685000 deaths were reported in 2020 by the World Health Organization. By the end of 2020, breast cancer was diagnosed in 7.8 million women in the previous five

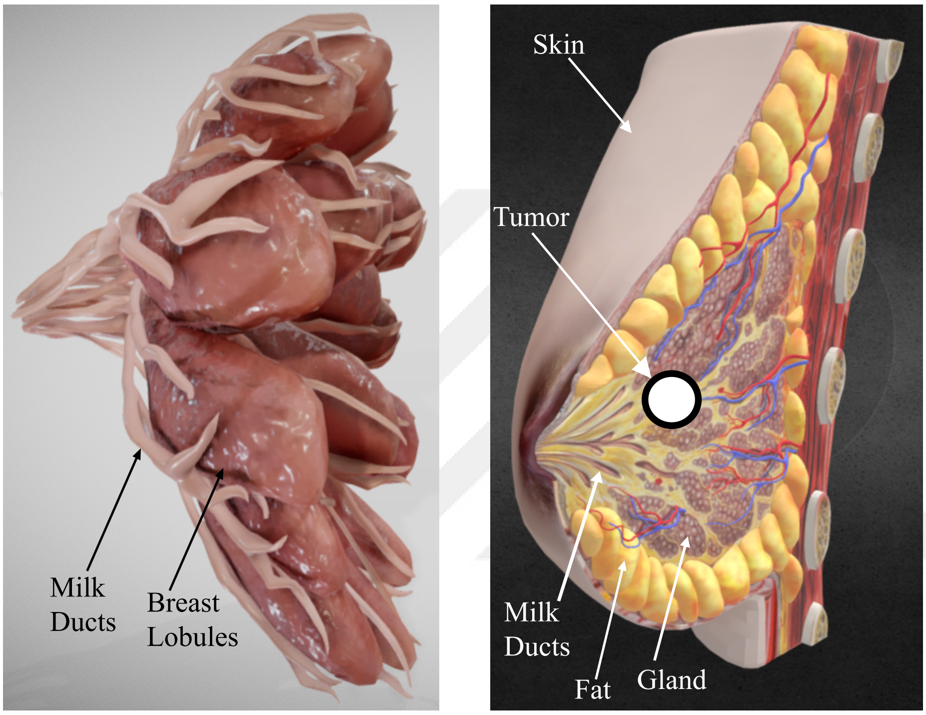

(a) (b)

Figure 1.2: (a) The 3-D structure of the breast includes the breast lobules and milk ducts. (b) In visual representation, the breast comprises the mammary gland, adipose tissue, milk ducts, tumor, and other tissues [6].

years, making it the most widely diagnosed cancer [8].

## 1.6 Imaging Modalities Utilized for Breast Cancer

There are several imaging techniques available to detect breast cancer. Mammography is a standard screening method used in medical imaging. Ultrasonography (US), magnetic resonance imaging (MRI), positron emission tomography (PET), electric impedance tomography (EIT), and IR thermography are other important breast imaging tools. These modalities are either complementary or alternative to mammography in breast imaging [9].

### 1.6.1 Mammography

Mammography screening tools are widely used to detect breast cancer. Its significance is its ability to identify small breast tumors, often invisible to the patient, at an early stage when the remedy is more effective [10]. However, this technique also has several limitations:

- The false-negative rate of mammography can be high; this rate can be as high as 35% in younger breasts having dense breast tissue [11, 12]. Mammography is less sensitive to dense breast tissue, which is dominant in young women's breasts. Thus, mammography is more likely to miss fast-growing tumors in younger women with dense breasts [13].
- The rate of false positives in mammography can be high, reaching up to 50%, resulting in unnecessary operations, such as biopsies or treatments, in women who do not have breast cancer [14].
- Mammography involves breast compression and radiation exposure, which can be uncomfortable for patients and potentially increase radiation-related risks with frequent exposure [15].

Thus, the practical application of mammography is limited, especially when dealing with younger women with dense breast tissues. Various imaging techniques have been developed to manage this issue and to enhance accuracy and precision. The main aim of breast imaging is to determine the presence of breast cancer during early developmental stages [12].

### 1.6.2 Other Breast Imaging Modalities

Other imaging methods that are generally used to screen breast tumors are ultrasound and MRI. Ultrasound works as a standalone tool for screening women's breasts, or it can be combined with mammography [16]. Ultrasound is more sensitive than mammography in detecting tumors with denser breast tissue. In practice, the use of ultrasonography has been expanded to distinguish between benign and malignant masses. Therefore, it reduces the risk of overdiagnosis and excessive treatment associated with mammography [15]. Although ultrasound is non-invasive and radiation-free, it is not often used alone for tumor screening [17].

MRI is another screening tool for breast cancer detection. Research performed on high-risk women has revealed that MRI exhibits relatively higher sensitivity than mammography but has lower specificity [18]. This lower specificity results in a higher rate of false positives and an increased need for additional tests. Therefore, MRI is typically not used for routine breast health screening [19]. The American Cancer Society guidelines recommend MRI as a supplementary screening method, primarily for specific age groups rather than for the broader population at risk for breast cancer [17, 20].

The performance of mammography, US, and MRI imaging modalities in breast tumor diagnosis was compared. Mammography had an average sensitivity of 54.5% (range: 27% to 86.8%) and an average specificity (proportion of true negative results among all negative results) of 85.5% (range: 62.9% to 98.8%). The US had an average sensitivity of 67.2% (range: 26.9% to 87.5%) and an average specificity of 76.8% (range: 18.8% to 96.9%). When considering other imaging modalities, MRI demonstrated an average sensitivity of 94.6% (range: 85.7% to 100%) and an average specificity of 74.2% (range: 25% to 100%) [21].

PET is based on the principle that tumor cells exhibit higher glucose uptake than surrounding tissues. Thus, PET imaging can efficiently identify malignant masses [22]. PET imaging exhibits a higher accuracy in detecting larger and more aggressive tumors. However, the cost of PET limits its use as a routine diagnostic tool [23].

EIT is another imaging tool that uses electrical conductivity parameters to determine the conductivity distribution of tumorous breast tissues. This is valuable for breast cancer detection, particularly in young women with dense breast tissues. Stojadinovic et al. investigated to evaluate the feasibility of EIT for early breast cancer detection in young women [24]. However, studies are in progress to reveal the potential of EIT as a screening tool for breast tumors.

## 1.7 Thermography

IR thermal imaging is a non-ionizing, non-invasive, cost-effective, and complementary imaging tool for breast cancer detection. With an average sensitivity of 90%, IR thermal imaging can detect breast cancers quite early, up to ten years in advance, compared to alternative imaging techniques [3, 25]. Thus, IR thermal imaging has become a practical tool for the identification of breast cancer at an early stage [26].

Thermography visualizes temperature distribution on the surface of an object. This is based on the principle that different materials emit different amounts of IR radiation depending on their own temperature. IR thermal imaging cameras can detect IR emissions and generate thermograms. In practice, IR thermography has several applications, including environmental, maintenance, non-destructive testing, and medical [27].

The radiation recorded by the thermal IR camera is at the infrared wavelengths of the electromagnetic spectrum, as shown in Figure 1.3. Thermography can detect minor differences in body temperature by using high-performance IR camera technology [27].

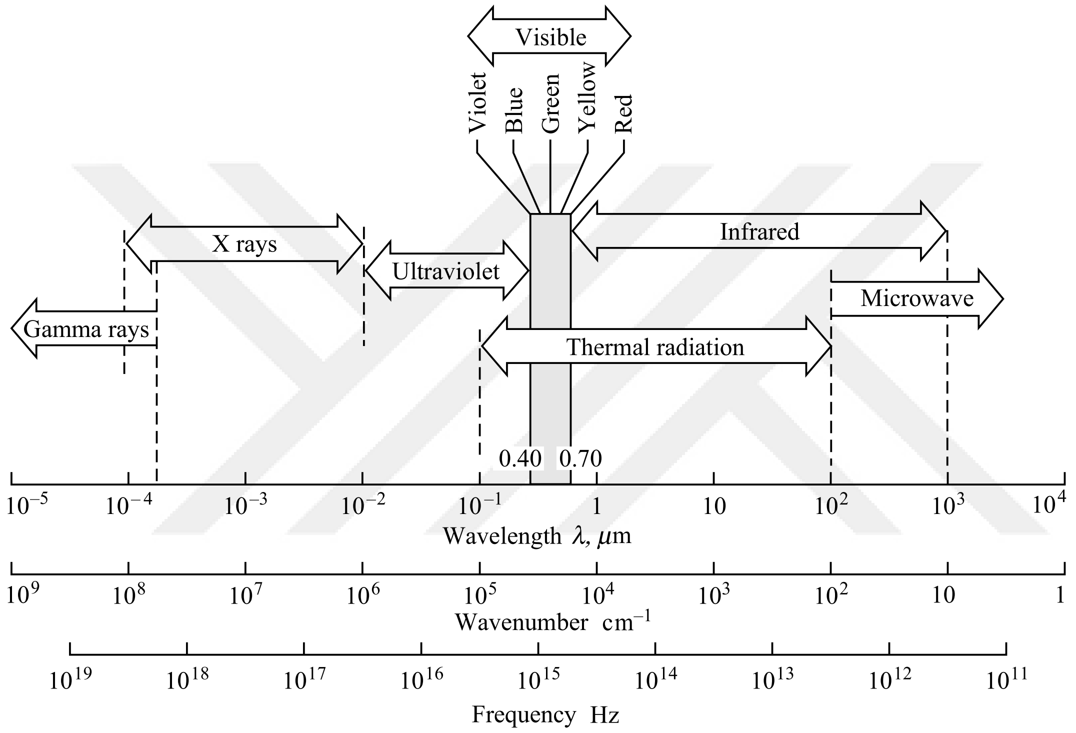

Figure 1.3: Electromagnetic spectrum (for radiation traveling through a vacuum), thermal radiation frequency bands, and wavelengths [28].

### 1.7.1 Infrared Technology for Thermography

William Herschel discovered the electromagnetic spectrum in the 1800s using a thermometer. He used a glass prism to study the heating effect of different colors. Herschel identified the part of the visible spectrum that exhibited the greatest heating effect. In 1800, Herschel demonstrated the existence of a far-infrared region [29]. Thermometers were the primary instruments used for radiation detection until 1829 when Nobili introduced a thermocouple. During this period, Melloni developed an initial thermopile by linking multiple thermocouples in series. These thermocouples were used to detect heat from a person at a distance of three meters. John Herschel made an influential innovation by producing the first heat image and transferring it to paper, which he called a thermogram in 1840. In addition to these advances, Langley developed bolometers in 1880, and James Dewar introduced liquefied gases as cooling materials for detectors in 1892. In the 1930s, lead sulfide (PbS) detectors were introduced. The invention of indium antimonide (InSb) detectors in the 1940s enabled operation in the mid-wave band. In the 1960s, mercury cadmium telluride detectors (HgTeCd) were developed [29, 30].

Detectors used in IR camera technology can be either cooled or uncooled. Cooling is not required when the microbolometer detectors are used. Detectors also rely on scanning technologies such as single-element or multi-element practices. Focal Plane Array (FPA) technology with multiple rows of detectors is widely adopted, offering improved thermal imaging with high resolution [29, 31]. Advances in IR camera technology and image-processing algorithms have renewed IR imaging in medicine since the 1980s. Quantum well-infrared photodetectors (QWIP) are hardware utilized in IR cameras with excellent pixel operability, uniformity, and stability [32, 33]. The main drawback of the standard QWIP technology is its relatively low conversion efficiency due to weak quantum efficiency [32].

A study conducted by R. Joro et al. evaluated the efficiency of infrared cameras in detecting breast cancer. The researchers tested the ability of three types of detectors, including QWIP, microbolometer, and photovoltaic detectors, in patients with breast cancer. The results showed that the InSb photovoltaic camera outperformed the other detectors in identifying vasomotor and cardiogenic frequency differences between cancerous and healthy breast tissues. The GaAs QWIP camera demonstrated an imaging performance that was satisfactory and comparable to that of photovoltaic cameras in terms of sensitivity; however, the integration time of the QWIP cameras was longer [34].

## 1.8 Breast Thermography

The integration of IR thermal imaging into medicine for breast cancer detection began in the 1960s, primarily influenced by advances in military IR methods. This technique was studied until 1970 [25, 35]. R. Lawson reported the practical results of this new application in 1957 [36]. To our knowledge, this is the first known report of IR imaging for breast cancer. It was discovered that the skin temperature of breast tumors is higher than that of normal healthy tissues. Williams and Handley found that breast cancer had a temperature rise of up to 1–2 °C in 1961. They suggested that the rise in tumor temperature was associated with increased blood flow and a higher metabolic rate [37].

IR imaging has emerged as a promising and evolving tool for breast cancer detection since the 1980s [38]. In 1982, Gautherie et al. conducted a comprehensive study comparing mammography and IR thermography for breast cancer detection [39]. Keyserlingk et al. found that using breast thermography combined with mammography has significantly improved the sensitivity of detecting breast cancer [40]. Consequently, IR imaging has become an important breast imaging tool due to its cost-effectiveness and practical use in medicine [33, 41]. The noise equivalent temperature difference (NETD) of current IR cameras provides a satisfactory resolution for measuring the thermal differences on the skin surface caused by tumorous tissues.

The temperature differences in breast thermography have a physiological basis. Heat is transferred from the inside of the breast to the skin's surface in two ways. These are vascular circulation and thermal conduction. Later, the heat on the surface reaches balance through various heat-exchange mechanisms involving radiation, convection, and evaporation. In addition, several physiological and pathological factors associated with breast tumors affect the body surface temperature distribution. These factors include increased blood flow and higher metabolic rates in the tumorous tissue. The initiation and growth of tumor formation are associated with neovascularization around the tissue. The development of new blood vessels before tumor appearance is known as angiogenesis, and this process enhances the supply of nutrients to tumorous tissue [42, 43]. These mechanisms increase the heat on and around the tumor, raising the surface temperature in this region. Ng et al. showed that temperature distribution has a symmetrical pattern concerning the body's midline for healthy people [44]. Even a slight deviation in the thermographic distribution changed the symmetrical pattern. Thus, the difference in symmetry could indicate the possibility of a tumor inside the body. Its ability to detect temperature differences on the surface of the breast makes IR thermography a potential tool for detecting abnormal regions [45].

Passive mode IR thermography does not use an external heat source. Thermal changes observed on the skin surface in passive mode images are generally associated with increased tumor blood flow and metabolic heat. In active mode IR thermography, an external heat source is applied to the patient to obtain the surface temperature distributions. Interactions between internal factors and external heat sources produce active mode images [46].

Dynamic IR thermography uses time-varying images, whereas passive thermography employs breast temperature measurement in which a single image is obtained. Differences in internal and external thermal factors result in changes in thermal distribution over time [47, 48]. This technique involves monitoring and analyzing variations in breast temperature, particularly during temporary events, such as exposure to cold stress and hot stress [49]. Dynamic IR thermal imaging generally focuses on the physiological activity of biological tissues and their response to transient events rather than their stable anatomical characteristics [50].

### 1.9 Active Thermography in Medicine

Arthur W. Guy studied the induced electromagnetic fields on the tissue phantoms in 1971. The dielectric parameters of the fat and bone phantoms were adjusted using aluminum powder. The electrical conductivity of the tissue was adjusted using acetylene black material. The muscle tissue was mimicked with a polyethylene-regulated dielectric constant in a high-water-content phantom. The electrical conductivity was adjusted by varying the NaCl concentration of the solution. These phantoms were prepared to mimic biological tissues excited with electromagnetic sources. Guy employed different body models to apply electromagnetic fields and compared the heating patterns observed in the phantom models at various frequencies [51].

M. Kaczmarek and A. Nowakowski worked on external heat source excitations called active IR-thermal imaging in 2003 [52]. External heat sources were used to enhance the sensitivity of IR imaging. External heat sources include electromagnetic fields, halogen lamps, and lasers. These investigations demonstrated the potential use of electromagnetic and optical sources for external heating [53].

Microwaves have been used as an external heat source for breast tumor detection. R. Tipa and O. Baltag (2006) applied microwave radiation in a 10–12 GHz band and observed up to 2.5 °C temperature increase in the patient's breast for two symmetrical positions [54]. S. Rahmatinia and B. Fahimi used an antenna with a frequency of 2.4 GHz to generate electromagnetic radiation in the direction of the breast. When tumors of size 2.5, 7, and 10 mm located 15 mm below the body surface were excited by an external source, the maximum temperature increase at the surface was 1 °C. According to their study, the size and depth of the tumor and the SAR of the body changed the surface temperature [46, 55]. In 2023, Jessie et al. detected tumorous breast tissue on the surface after an electromagnetic excitation. They conducted simulations and experimental studies using a patch antenna array at 2.4 GHz. They measured the temperature using temperature sensors placed under the antenna probes. They obtained temperature differences between 0.4 °C and 1 °C on the imaging surface [56]. Guo et al. performed a numerical study using a breast model with a 10 cm diameter geometry, including skin, fat, and glandular tissue. Simulations were performed within the 200–800 MHz frequency to detect one 1 mm tumor and two 1.5 mm tumors inside the body. They concluded that a higher operating frequency resulted in more accurate tumor localization [57].

In another application of active thermography, a heat source was applied to the body using a near-infrared (NIR) laser. Tumors absorbed and scattered the NIR light more strongly than the surrounding tissue. Therefore, this external heat source caused an increase in the temperature of the tumor tissue. The temperature difference between healthy and tumor tissue was recorded using an IR camera. A 1064 nm NIR laser was used to heat the body for 5 s at a power density of 0.6 $\mathrm{W/cm^2}$. A rapid temperature increase of 1 $^{\circ}\mathrm{C}$ was observed during this short duration [58].

## 1.10 Electro-Thermal Imaging

Gençer et al. employed another active IR technique called applied-current electro-thermal imaging (AC-ETI) for tumor detection [59]. This study used a low-frequency current (5 mA) to improve imaging performance. They applied a sinusoidal current by placing electrodes directly on the body surface in two dimensions and visualized the temperature difference using a dual-band camera [60]. In the AC-ETI, a tumor of 42.8 $\mathrm{mm}^3$ was detected numerically at a 15 mm distance from an electrode assuming a camera with 2 $^{\circ}$mC NETD [61].

G. Ozdemir applied multi-frequency currents in the electro-thermal imaging technique owing to the frequency-dependent variation of the conductivity of the tissues. Each image represented a different thermal distribution due to the change in the electrical properties of the tissue. Increasing the applied current frequency to 1 MHz resulted in a performance rise in the surface image contrast [62].

Alternatively, to increase the temperature contrast on the surface, we proposed inducing currents without body contact by using current-carrying coils near the body in our previous studies [63, 64]. In the simulation study, the performance of the proposed system was investigated using a Helmholtz coil pair to induce currents at 27.12 MHz. A 10 mm malignant tumor was detected up to a depth of 20 mm with the induced current electro-thermal approach [63]. A solenoid coil was constructed for the experimental study, and the body surface temperature was measured using a hand-held IR thermometer [64].

## 1.11 Induced Current Active Thermography Applications

The non-destructive testing (NDT) technique is an industrial application of induced current (eddy current) active thermography [65, 66]. The NDT method involves the application of an electric current to a coil placed over the surface of the object being tested. The coil generates an electromagnetic field that induces eddy currents in the electrically conductive body [67]. Eddy currents generate heat through ohmic losses. The air in the cracks or slots exhibits zero conductivity in the inspected highly conductive object. The contrast in the electrical conductivity enhances the asymmetry in the current density distributions on and around the slots/cracks of the conductive object. Figure 1.4 illustrates the enhanced temperature contrast along the cracks. The surface temperature distribution was recorded using a standard IR camera [68].

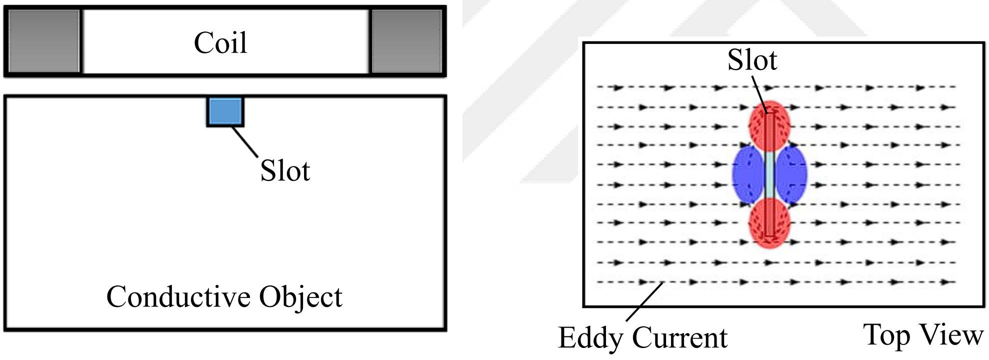

(a) (b)

Figure 1.4: (a) Illustration of NDT application when there is a slot (air gap) on the surface of a conductive object using an excitation coil. (b) The eddy current distribution from the top-side view. The temperature in the red area (top and bottom zones of the slot) was higher than that in the blue area (left and right zones of the slot) [68].

The electromagnetic skin depth provided by equation (1.1) describes the depth of penetration of electromagnetic fields into a material during inspection, where $\sigma$ is the electrical conductivity, $\mu$ is the magnetic permeability, and $f$ is the frequency of the applied field [65].

$$\delta = \frac{1}{\sqrt{\pi \; f \; \mu \; \sigma}} \tag{1.1}$$

Hyperthermia is another application of induced-current (induction) thermography. Increasing the temperature of a tumor for cancer therapy purposes is called hyperthermia. Owing to the induction, the temperature ranges from 39 °C to significantly higher levels. Magnetic nanoparticles have been used for cancer therapy in magnetic hyperthermia applications. Various magnetic nanoparticles, described by their unique properties, have proven helpful in magnetic hyperthermia therapy. The main advantage of this method is the regulation of local tumor temperatures [69].

## 1.12 Dielectric Characteristics of Breast Tissues

The dielectric parameters of the tissues can vary depending on their state and excitation frequency. Several investigations have examined the dielectric properties of biological tissues and breasts. Fricke and Morse used tissue examples to explain that tissues demonstrate characteristics similar to a resistor and capacitor in parallel in 1926 [70]. Kenneth S. Cole and Robert H. Cole presented a model that explains the impedance characteristics of tissues [71]. Schwan studied the frequency-dependent differences in the dielectric parameters of biological tissues [72].

Surowiec et al. classified breast tissues and investigated the dielectric properties of breast tumors and surrounding tissues within a frequency range of up to 100 MHz. They reported higher permittivity values in the central tumor regions. Surowiec focused on human breast tumors and their surrounding tissue, categorizing them considering their distance from the central part of the tumor [73]. Chaudhary et al. investigated breast tissues and measured the dielectric properties of both healthy and tumorous tissues. Remarkable differences were observed in the dielectric properties of healthy and tumorous breast tissues [74]. In 1996, Gabriel et al. presented a study explaining how the dielectric properties of various tissue types change with frequency [75]. Computer applications were developed to calculate the dielectric properties of human body tissues in the 10 Hz to 100 GHz frequency range using the parameters generated by Gabriel et al. [76, 77]. According to Gabriel's model, Tables 1.1 and 1.2 given below provide dielectric parameters for healthy breast tissue at frequencies between 100 kHz and 100 MHz.

Table 1.1: Electrical conductivities of breast tissues at frequencies between 100 kHz and 100 MHz [73, 75, 78, 79, 80].

| **Conductivity (S/m)** | **100 kHz** | **1 MHz** | **10 MHz** | **100 MHz** |
|---|---|---|---|---|
| **Muscle** | 0.36 | 0.5 | 0.62 | 0.7 |
| **Breast Gland** | 0.54 | 0.6 | 0.72 | 0.79 |
| **Breast Fat** | 0.02 | 0.02 | 0.02 | 0.03 |
| **Dry Skin** | 0.0004 | 0.013 | 0.2 | 0.49 |

Table 1.2: Electrical permittivities of breast tissues at frequencies between 100 kHz and 100 MHz [73, 75, 78, 79, 80].

| **Permittivity (F/m)** | **100 kHz** | **1 MHz** | **10 MHz** | **100 MHz** |
|---|---|---|---|---|
| **Muscle** | 8090 | 1840 | 1710 | 66 |
| **Breast Gland** | 3300 | 1430 | 163 | 68.8 |
| **Breast Fat** | 70.6 | 23.7 | 7.9 | 5.7 |
| **Dry Skin** | 1120 | 991 | 362 | 73 |

# CHAPTER 2

# INDUCED CURRENT ELECTRO-THERMAL IMAGING

## 2.1 Introduction

The materials and methods used in IC-ETI are discussed in this Chapter. The first section discusses the dielectric properties of tumorous breast tissue at different operating frequencies. The second section presents the theoretical basis of IC-ETI and comprehensively analyses the basic electromagnetic field equations, Pennes' Bio-heat equation, the magnetic field generated by a finite-length solenoid coil, IR radiation, current density refraction, and absorbed power distribution.

## 2.2 Tumorous Breast Model

Different geometric models of multilayered breasts can be created using different tissue compositions. These can be extremely dense, heterogeneously dense, scattered fibro-glandular, or predominantly fat. The diagram illustrates a cross-sectional view of the breast model shown in Figure 2.1, which provides tissue percentages for each layer [81].

The number of breast cancer cases increases after the age of 35, and this age group includes individuals with scattered glandular and heterogeneously dense breasts. The breast model for this age group includes a 40% glandular layer, 40% fat layer, and 20% muscle layer as shown in Figure 2.1. In equation (2.1), $\theta_i$ is the volumetric ratio of parameter $\sigma_i$ (conductivity) for a given tissue in the breast. In this structure, a breast tumor is a point heat source, and healthy tissues and tumors are assumed to be homogeneous.

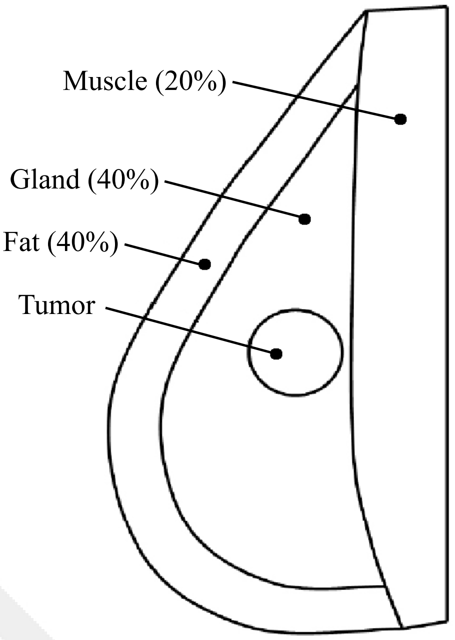

Figure 2.1: An illustration of the cross-sectional view of the breast structure with its layers and containing an internal tumor [81].

$$\sigma = \sum_{i=1}^{n} \sigma_i \, \theta_i \tag{2.1}$$

The volume-averaged breast model used in this study has a 50% gland layer and a 50% fat layer, as the muscle layer is located at the back of the breast, according to the structure of the breast and its layers. The frequency-dependent electrical conductivities of the tumor and healthy breast tissues are listed in Table 2.1.

Table 2.1: Within the frequency range of 100 kHz to 100 MHz, the electrical conductivities of the healthy breast tissues and tumors [73, 75, 78, 79, 80].

| **Conductivity (S/m)** | **100 kHz** | **1 MHz** | **10 MHz** | **100 MHz** |
|---|---|---|---|---|
| **Tumor** | 0.6 | 0.75 | 0.85 | 1.1 |
| **Breast Gland** | 0.54 | 0.6 | 0.72 | 0.79 |
| **Breast Fat** | 0.02 | 0.02 | 0.02 | 0.03 |
| **50% Gland, 50% Fat** | 0.28 | 0.31 | 0.37 | 0.41 |

The ICNIRP guidelines have established restrictions on exposure to RF fields within the range of 100 kHz to 10 MHz in terms of current density (due to the risk of neurostimulation and the prevention of its effects on nervous system function) and tissue heating [82]. Owing to the constraints imposed by the current density at frequencies up to 10 MHz, it is advisable to restrict the current applied to the coil in a realistic breast model or to consider frequencies above 10 MHz as an alternative. Magnetic induction tomography (MIT) was performed at frequencies ranging from 10 kHz to 10 MHz [83, 84]. MIT is based on the perturbation of the induced current density by a conducting object, similar to the IC-ETI method. Figure 2.2 illustrates the conductivity contrast between tumor and healthy tissue. From 100 kHz to 10 MHz, the conductivity ratios of the tumor and healthy tissue are similar. However, as the frequency increases, the effect of the permittivity parameter on the external heat source term also increases, and a higher current level is required when the frequency is low. We used an air-core solenoid coil (a helical coil of wire) to induce a current and selected a frequency of 750 kHz to drive the coil resonance circuit with the power amplifier.

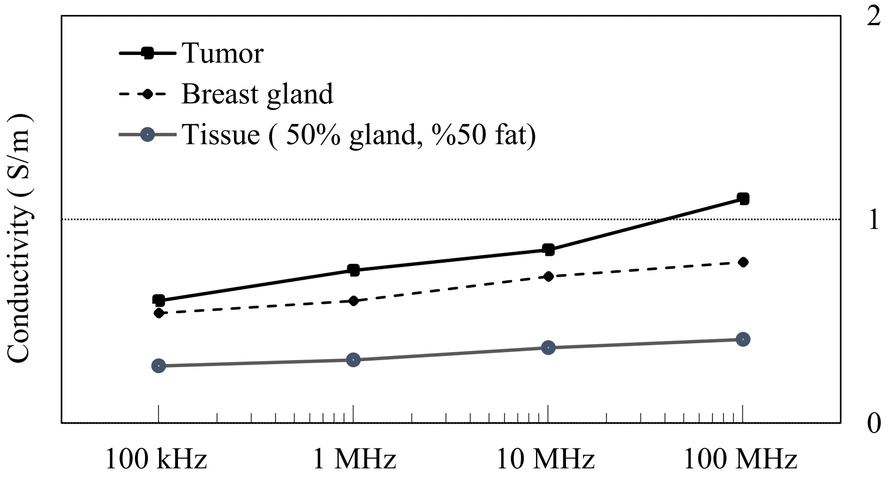

Figure 2.2: Frequency-dependent electrical conductivities of breast tumor, breast gland, and the tissue model used in the study [64].

## 2.3 Theory

### 2.3.1 Basic Electromagnetic Field Equations and $\boldsymbol{A} - \phi$ formulation

A sinusoidal current ($e^{j\omega t}$ dependent) is applied to the coil where $\omega$ $(\mathrm{rad/s})$ is the angular frequency and $t$ (s) is time. $\boldsymbol{A} - \phi$ equations are derived using Coulomb's gauge, and coupled partial differential equations (2.2) and (2.3) are used to solve the electric field $\boldsymbol{E}$ $(\mathrm{V/m})$ in an inhomogeneous medium (tumorous tissue) [85, 86, 87]:

$$\nabla^2 \boldsymbol{A} - j\omega\mu\left(\sigma + j\omega\epsilon\right)\boldsymbol{A} - \mu\left(\sigma + j\omega\epsilon\right)\nabla\phi \;=\; -\mu\boldsymbol{J}_{\mathrm{s}} \tag{2.2}$$

$$\nabla \cdot \left[\left(\sigma + j\omega\epsilon\right)\nabla\phi\right] + \nabla\left(\sigma + j\omega\epsilon\right) \cdot j\omega\boldsymbol{A} \;=\; \nabla \cdot \boldsymbol{J}_{\mathrm{s}} \tag{2.3}$$

Here, $\epsilon$ $(\mathrm{F/m})$ is the electrical permittivity and $\sigma$ $(\mathrm{S/m})$ is the electrical conductivity of the medium. The medium was considered to be isotropic. The electromagnetic boundary conditions are magnetic insulation on the domain boundary, continuity of the tangential component of the magnetic vector potential on the inner (tumor tissue and tissue-air) boundaries, and normal components of the current density are continuous at the tumor-tissue boundary [88, 89, 90]. The source current density $\boldsymbol{J}_{\mathrm{s}}$ $(\mathrm{A/m^2})$ is zero outside the coil. $\boldsymbol{E}$ can be calculated by solving the electric scalar potential $\phi$ (V) and magnetic vector potential $\boldsymbol{A}$ $(\mathrm{Wb/m})$ using the following equation:

$$\boldsymbol{E} \;=\; -j\omega\boldsymbol{A} - \nabla\phi \tag{2.4}$$

### 2.3.2 Bio-Heat Equation

Pennes' Bio-heat equation describes the thermal interactions between tissues and heat sources [91]. The differential equation governing the space and time behavior of the temperature distribution produced by different heat sources can be calculated using Pennes' Bio-heat transfer equation (2.5):

$$\rho c \frac{\partial T}{\partial t} - \nabla.\left(k \nabla T\right) \;=\; q_b + q_m + q_{ext} \tag{2.5}$$

In Pennes' equation, $\rho$ $(\mathrm{g/cm^3})$ is mass density, $c$ $(\mathrm{cal/g}\ ^{\circ}\mathrm{C})$ is specific heat, $k$ $(\mathrm{cal/s}\ ^{\circ}\mathrm{C})$ is thermal conductivity and $T$ $(^{\circ}\mathrm{C})$ is temperature.

The term $q_b$ $(\mathrm{cal/s\,cm^3})$ describes the blood perfusion rate and is expressed by the following equation:

$$q_b \;=\; w\ \rho_b\ c_b(1-k)(T_a - T) \tag{2.6}$$

where, $w$ $(\mathrm{s^{-1}})$ is the blood perfusion rate per unit volume of tissue, $c_b$ $(\mathrm{cal/g}\ ^{\circ}\mathrm{C})$ is the specific heat value of blood, and $T_a$ $(^{\circ}\mathrm{C})$ is the arterial blood temperature. The second source term, $q_m$ $(\mathrm{cal/s\,cm^3})$, on the right-hand side of equation (2.5), describes the metabolic heat generation rate [63].

The external heat source term, $q_{ext}$ $(\mathrm{W/m^3})$ can be calculated according to the conductivity, dielectric parameters, and electric field in the medium because of the sinusoidal current applied to the coil (assuming no magnetic material in biological tissues), as follows [88, 92]:

$$q_{ext} \;=\; \frac{1}{2}\left(\sigma + \omega\, \epsilon^{''}\right) |\boldsymbol{E}|^{2} \tag{2.7}$$

The complex permittivity term can be written as: $\epsilon = \epsilon^{'} - j\epsilon^{''}$ where $\epsilon^{'}$ and $\epsilon^{''}$ are the real and imaginary parts, respectively [88].

### 2.3.3 Specific Absorption Rate (SAR)

The SAR value is a measure of the rate of radio-frequency (RF) energy absorption by the body and is calculated using equation (2.8), where $\Delta V$ is the unit volume, $r$ is the position parameter, and $\rho(r)$ is the mass density [93]. Cubic breast geometry is more suitable for calculating the average local SAR value and determining tumor detection depth. The SAR value was averaged for a 10 g cubic mass using the following equation:

$$SAR = \frac{1}{\triangle V} \iiint \frac{\sigma(r)}{2\,\rho(r)} \,|\, \boldsymbol{E}(r) \,|^{2}\, dV \tag{2.8}$$

### 2.3.4 Magnetic Field Created By a Finite Length Solenoid Coil

The solenoid coil winding generates a magnetic field when an electric current varying over time, denoted by $I$, is applied. $a$ is the radius of the wire, and $h$ is the distance between the loops. The differential element $\boldsymbol{dl}$ is in the direction of $I$, and $\boldsymbol{a_r}$ is a unit vector in the $r$ direction, as illustrated in Figure 2.3. The distance $r$ is between the source and observation point $P(x, y, z)$ [94].

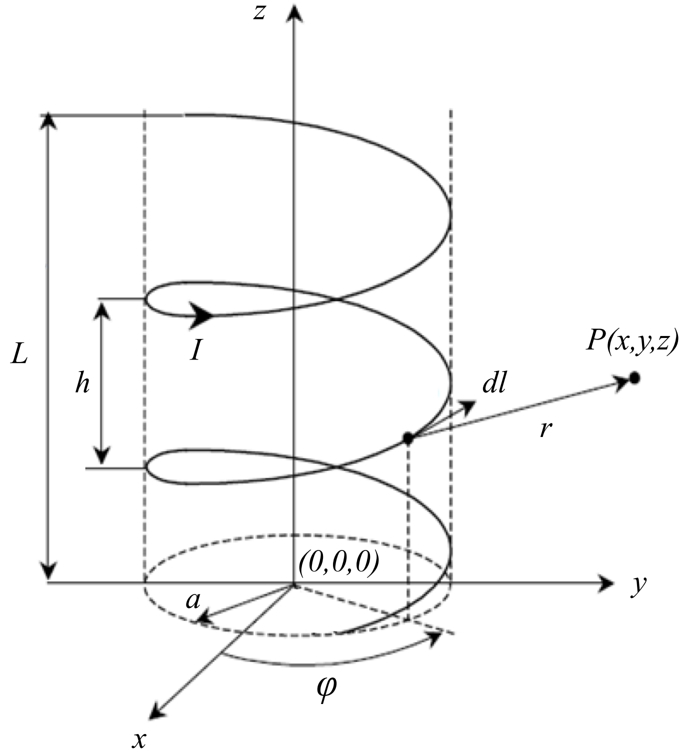

Figure 2.3: A helical line of finite length $L$ is located in the coordinate system. The field at point $P(x, y, z)$ is shown when time-varying current $I$ flows through the wire [95].

$$\boldsymbol{B}\left(x,y,z\right)=\frac{\mu_0\,I}{4\pi}\int\frac{\boldsymbol{dl}\ \times\ \boldsymbol{a_r}}{r^2} \tag{2.9}$$

The parametric equations of the helical coil concerning the angle parameter $\varphi$ indicated in Figure 2.3 are as follows:

$$X\left(\varphi\right)=a\ cos\varphi \tag{2.10}$$

$$Y\left(\varphi\right)=a\ sin\varphi \tag{2.11}$$

$$Z\left(\varphi\right)=\frac{h}{2\pi}\varphi \tag{2.12}$$

$\boldsymbol{a_x}$, $\boldsymbol{a_y}$ and $\boldsymbol{a_z}$ are the unit vectors in the specified directions. $\boldsymbol{a}_r(\varphi)$ and $\boldsymbol{dl}(\varphi)$ are given by the following equations.

$$\boldsymbol{a}_r\left(\varphi\right)=\frac{\left(x-acos\varphi\right)\boldsymbol{a_x}+\left(y-asin\varphi\right)\boldsymbol{a_y}+\left(z-\frac{h}{2\pi}\varphi\ \right)\boldsymbol{a_z}}{\sqrt{\left(x-acos\varphi\right)^2+\left(y-asin\varphi\right)^2+\left(z-\frac{h}{2\pi}\varphi\right)^2}} \tag{2.13}$$

$$\boldsymbol{dl}(\varphi)=-asin\varphi d\varphi\boldsymbol{a_x}+acos\varphi d\varphi\boldsymbol{a_y}+\frac{h}{2\pi}d\varphi\boldsymbol{a_z} \tag{2.14}$$

The components of $\boldsymbol{B}(x,y,z)$ are expressed by the following equations [94].

$$B_x\left(x,y,z\right)=\frac{\mu_0 I}{4\pi}\int_0^{\frac{2\pi L}{h}}\frac{acos\varphi\left(z-\frac{h}{2\pi}\varphi\right)-\frac{h}{2\pi}(y-asin\varphi)}{\left(\left(x-acos\varphi\right)^2+\left(y-asin\varphi\right)^2+\left(z-\frac{h}{2\pi}\varphi\right)^2\right]^{1.5}}d\varphi \tag{2.15}$$

$$B_y\left(x,y,z\right)=\frac{\mu_0 I}{4\pi}\int_0^{\frac{2\pi L}{h}}\frac{asin\varphi\left(z-\frac{h}{2\pi}\varphi\right)-\frac{h}{2\pi}(x-acos\varphi)}{\left(\left(x-acos\varphi\right)^2+\left(y-asin\varphi\right)^2+\left(z-\frac{h}{2\pi}\varphi\right)^2\right]^{1.5}}d\varphi \tag{2.16}$$

The magnetic field $\boldsymbol{H}$ (A/m) is expressed by equation (2.17).

$$\boldsymbol{H}\left(x,y,z\right)=\frac{\boldsymbol{B}\left(x,y,z\right)}{\mu_0} \tag{2.17}$$

### 2.3.5 IR Radiation

An IR camera records and displays the thermograms of an object based on the emitted radiation in the infrared spectrum. All objects emit IR radiation as infrared waves, provided their temperature is above absolute zero [28]. The spectrum in terms of infrared frequencies can be divided into three smaller frequency windows (bands) for the thermal IR range (wavelengths between 0.75–1000 µm). These windows are NIR and SWIR (0.75–3 µm), MWIR (3–8 µm), and LWIR (8–15 µm), as shown in Figure 2.4. The wavelength of the FIR region is between 15–1000 µm [62].

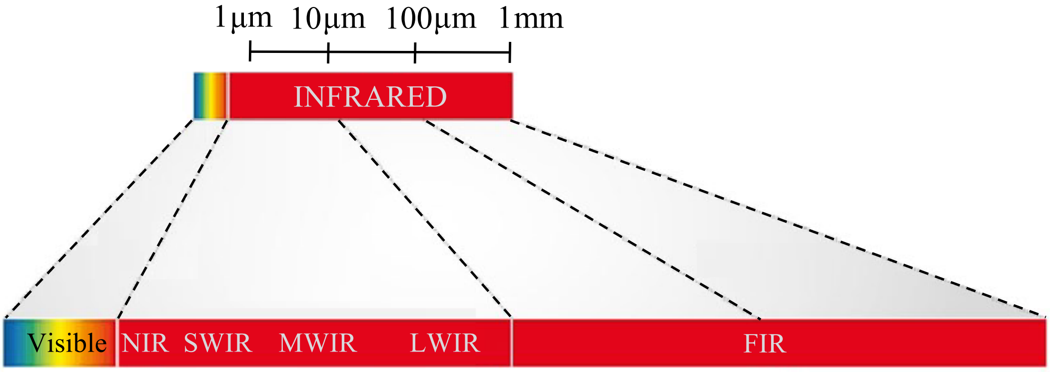

Figure 2.4: The infrared spectral range is subdivided into near-infrared (NIR), short-wave infrared (SWIR), middle-wave infrared (MWIR), long-wave infrared (LWIR), and far-infrared (FIR) frequency windows [96].

Wien's displacement law describes the peak wavelength ($\mu\mathrm{m}$) with equation (2.18). The spectrum's peak shifts to shorter wavelengths when the object's temperature increases. $T$ is the temperature $(\mathrm{K})$ of the object.

$$\lambda_{max} = \frac{2898}{T} \tag{2.18}$$

A blackbody object is a theoretical object that absorbs all the incident radiation. Max Planck introduced the law by defining how the radiation emitted by a blackbody varies with wavelength [28]. Equation (2.19) explains the blackbody emittance with respect to the wavelength $\lambda$ ($\mu\mathrm{m}$).

$$W_\lambda = \frac{2\,\pi\,h\,c^2}{\lambda^5\,(e^{\frac{hc}{\lambda kT}} - 1)} \tag{2.19}$$

where, $c$ is the speed of light ($3 \times 10^8$ $\mathrm{m/s}$), $k$ is Boltzmann's constant ($1.38 \times 10^{-23}$ $\mathrm{Joule/K}$), $h$ is Planck's constant ($6.62 \times 10^{-34}$ $\mathrm{Joule\ s}$). Equation (2.20) describes the total emission of a blackbody, considering all wavelengths and frequencies:

$$W = \sigma\,T^4 \tag{2.20}$$

where $W$ is the total emitted radiation ($\mathrm{W/m^2}$), $\sigma$ is the Stefan-Boltzman constant ($5.676 \times 10^{-8}$ $\mathrm{W/m^2\ K^4}$). When the emissivity of real objects is taken into account, equation (2.20) takes the following form:

$$W = \varepsilon\,\sigma\,T^4 \tag{2.21}$$

The emissivity term, $\varepsilon$, refers to the amount of radiation an object emits compared to a blackbody. Real objects exhibit an emissivity ranging from 0 to 1. Only the perfect blackbody has an emissivity of 1. The emissivity of human skin is approximately 0.972–0.998, making it a nearly perfect absorber in the wavelength range between 3–14 µm [97]. The emissivity values of human skin at infrared wavelengths are listed in Table (2.2).

Table 2.2: The emissivity of human skin at IR wavelengths [33, 98].

| **Tissue** | **Emissivity** |
|---|---|
| Black Skin (3–12 µm) | 0.98 |
| White Skin (3–14 µm) | 0.97 |
| Burnt Skin (3–14 µm) | 0.97 |

The total power collected by an IR camera is shown in Figure 2.5. It is necessary to consider reflections from the surroundings and the transmittance parameter of the atmosphere to explain IR camera measurements. Owing to the emission from the object directly, the power received by the IR camera is ($\varepsilon\,\tau\,\sigma\ T_{obj}^4$), where $\tau$ is the transmittance of the atmosphere. Total collected power, $W_{total}$ by an IR camera, can be expressed with equation (2.22) [99].

$$W_{total} = \varepsilon\,\tau\,\sigma\ T_{obj}^4 + (1-\varepsilon)\,\tau\,\sigma\ T_{refl}^4 + (1-\tau)\,\sigma\ T_{atm}^4 \qquad (2.22)$$

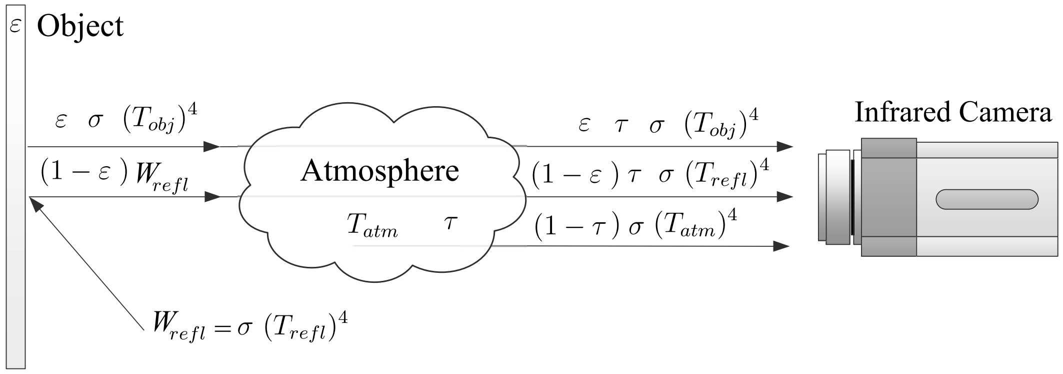

Figure 2.5: The power measured by an IR camera has three components: the power emitted directly by an object, reflections from the surroundings, and radiation from the atmosphere [100].

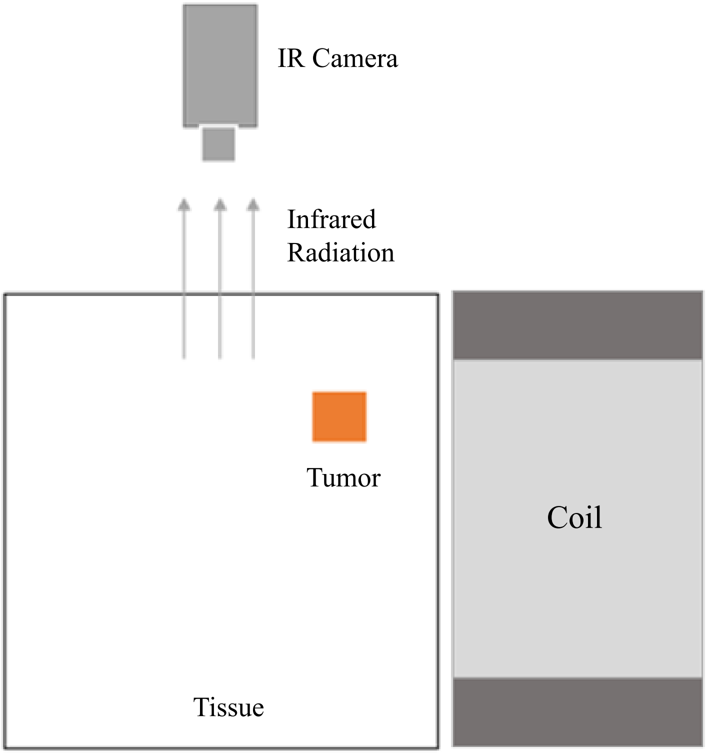

Figure 2.6: Illustration of the infrared radiation emitted from the body surface to the IR camera for the IC-ETI method.

Heat transfer mechanisms are conduction, convection, radiation, and evaporation. The heat transfer from the body is shown in Figure (2.6) owing to air convection, radiation, and evaporation of sweat. The following equation expresses total heat loss [101, 102]:

$$-k\,\frac{\partial T}{\partial n} \;=\; h\,(T_s - T_\infty) + \varepsilon\,\sigma\,({T_s}^4 - T_\infty^4) + Q_e \tag{2.23}$$

where $\boldsymbol{n}$ is the normal vector at the surface-air boundary, $h$ $(\mathrm{W/m^2\,K})$ is the convection heat transfer coefficient. The Stefan-Boltzmann law describes the heat transfer of radiation to the environment and is expressed by the second term on the right side of the equation (2.22). $T_s$ and $T_\infty$ (K) are the skin surface and surrounding boundary wall temperatures, respectively. $Q_e$ $(\mathrm{W/m^2})$ is the evaporative heat loss owing to sweat secretion. The continuity of heat fluxes and temperatures at the layer boundary (tumor tissue) is expressed by equations (2.24) and (2.25), where $k_m$ is the thermal conductivity of layer '$m$' [4]:

$$k_m \frac{\partial T_m}{\partial n} = k_{m+1} \frac{\partial T_{m+1}}{\partial n} \tag{2.24}$$

$$T_m = T_{m+1} \tag{2.25}$$

### 2.3.6 Refraction

#### 2.3.6.1 Refraction of the Plane Wave Direction in Different Media (Snell's law)

A medium's phase constant $\beta$ $(\mathrm{rad/m})$ can be expressed regarding its electrical parameters and operation frequency [85].

$$\beta = \omega\sqrt{\mu\epsilon}\left[\frac{1}{2}\left(\sqrt{1+\left(\frac{\sigma}{\omega\epsilon}\right)^2}+1\right)\right]^{1/2} \tag{2.26}$$

The $\beta$ value is higher in tumors when considering equation (2.26) owing to the higher electrical parameters of the tumor. Snell's law, given in equation (2.27), explains the refraction of plane-wave propagation in different media. In equation (2.27), $\theta_1$ is the incident angle (between the normal axis) of the first medium, and $\theta_2$ is the refraction angle of the second medium.

$$\beta_1 \, sin\theta_1 = \beta_2 \, sin\theta_2 \tag{2.27}$$

The refraction in the second medium depends on the electrical parameter differences between the tumor and its surrounding medium, which affect the direction of the propagated wave, as shown in Figure 2.7.

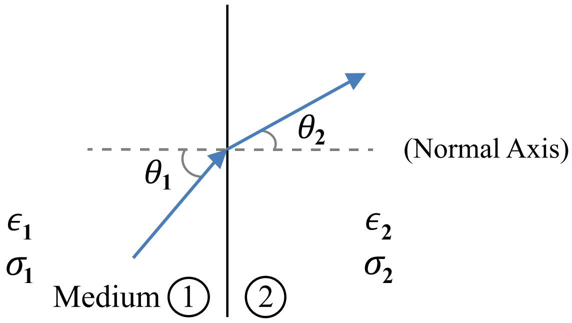

Figure 2.7: Refraction of a plane wave entering from one medium (with dielectric parameters of tissue 1) to another (with dielectric parameters of tissue 2).

#### 2.3.6.2 Current Density Refraction (Using Boundary Conditions)

Snell's law explains the refraction in the plane wave direction. To visualize the refraction of the current density vector $\boldsymbol{J}$ $(\mathrm{A/m^2})$, the tangential part of the electric field $(\boldsymbol{E}_{1t})$ in medium-1 is shown in Figure 2.8. Similarly, the normal component of the current density vector $(\boldsymbol{J}_{2n})$ for medium-2 is given by equation (2.29).

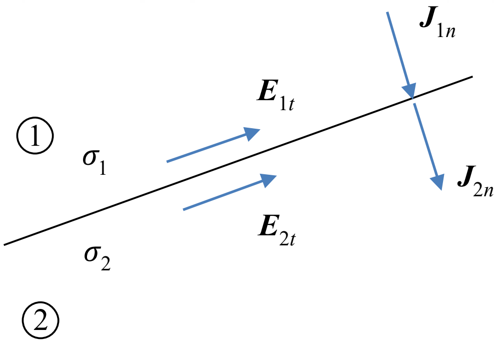

Figure 2.8: The tangential electric field and normal current density vector components were visualized at the boundary of the two different conductivities.

$$\boldsymbol{E}_{1t} = \boldsymbol{E}_{2t} = \boldsymbol{E} \tag{2.28}$$

$$\boldsymbol{J}_{1n} = \boldsymbol{J}_{2n} \tag{2.29}$$

To obtain the refraction relation given in equation (2.34) between the two conductive media, the normal and tangential components provided below can be used [86]:

$$\boldsymbol{E}_{1t} = \frac{\boldsymbol{J}_{1t}}{\sigma_1} \quad \boldsymbol{E}_{2t} = \frac{\boldsymbol{J}_{2t}}{\sigma_2} \tag{2.30}$$

$$\boldsymbol{J}_{1n} = \sigma_1 \boldsymbol{E}_{1n} \quad \boldsymbol{J}_{2n} = \sigma_2 \boldsymbol{E}_{2n} \tag{2.31}$$

$$\boldsymbol{J}_{1n} = \boldsymbol{J}_1 \cos\, \theta_1 = \boldsymbol{J}_2 \cos\, \theta_2 \tag{2.32}$$

$$\sigma_2 \boldsymbol{J}_1 \sin\, \theta_1 = \sigma_1 \boldsymbol{J}_2 \sin\, \theta_2 \tag{2.33}$$

$$\frac{tan\, \theta_2}{tan\, \theta_1} = \frac{\sigma_2}{\sigma_1} \tag{2.34}$$

To derive the refraction relation described in equation (2.37) between two dielectric mediums, the normal and tangential components provided below are employed (assuming no charge density on the interface surface) [86].

$$\boldsymbol{E}_{1t} = \boldsymbol{E}_1\ sin\, \theta_1 = \boldsymbol{E}_{2t} = \boldsymbol{E}_2\ sin\, \theta_2 \tag{2.35}$$

$$\boldsymbol{D}_{1n} = \epsilon_1 \boldsymbol{E}_{1n} = \boldsymbol{D}_{2n} = \epsilon_2 \boldsymbol{E}_{2n} = \epsilon_2\, \boldsymbol{E}_2\, cos\theta_2\ (\rho_s = 0) \tag{2.36}$$

$$\frac{tan\, \theta_2}{tan\, \theta_1} = \frac{\epsilon_2}{\epsilon_1} \tag{2.37}$$

The electrical parameters of the tissues change with operating frequency, leading to variations in the refraction angle. Biological tissues are neither purely conductive nor dielectric. Equation (2.34) is used to calculate refraction in conductive media, whereas equation (2.37) is suitable for dielectric media.

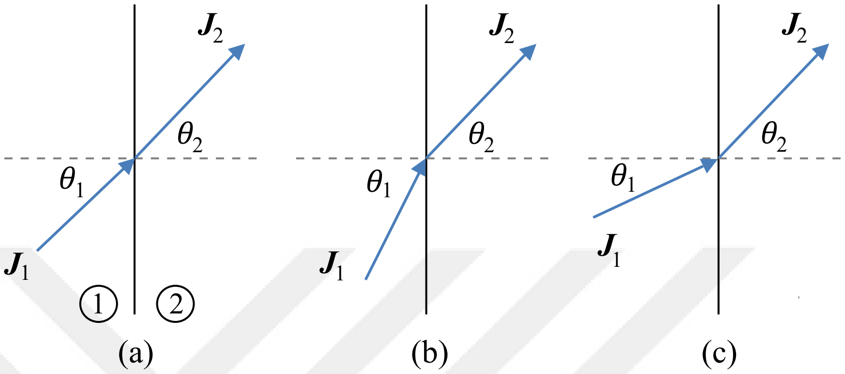

Figure 2.9: (a) Case 1: Current density vector penetrating an equally conductive (or permittivity) medium. (b) Case 2: Current density vector penetrating a medium with a lower conductivity (or permittivity). (c) Case 3: Current density vector penetrating a medium with higher conductivity (or permittivity).

Both electrical conductivity and permittivity terms were higher in the tumors than in the healthy tissues; thus, $\theta_2$ increases when the current density vector enters from the healthy tissue to the tumor. In this case, the proportion of the normal component of the current density vector decreases, and the tangential component increases.

#### 2.3.6.3 External Power Flow at the Tumor Boundary

When considering the power dissipation in biological tissue owing to the electrical conductivity parameter only, the $q_{ext}$ term becomes [103]:

$$q_{ext} = \frac{1}{2}\,\sigma\,|\boldsymbol{E}|^2 \tag{2.38}$$

A biological system absorbs electromagnetic power per unit volume ($q_{ext}$) in two adjacent tissues using equation (2.39) with the following ratio [104]:

$$\frac{q_{ext1}}{q_{ext2}} = \frac{\sigma_1 \, |\boldsymbol{E}_1|^2}{\sigma_2 \, |\boldsymbol{E}_2|^2} \tag{2.39}$$

When the electric field vector is parallel to the medium interface, the electric fields are parallel and equal, as expressed in equation (2.40).

$$\boldsymbol{E}_{1t} = \boldsymbol{E}_{2t} = \boldsymbol{E} \tag{2.40}$$

When the electric field is tangent to the interface between tissues 1 and 2, $\boldsymbol{E}_1 = \boldsymbol{E}_2$ and equation (2.39) becomes:

$$\frac{q_{ext1}}{q_{ext2}} = \frac{\sigma_1}{\sigma_2} \tag{2.41}$$

Similarly, when the current density vector enters the medium interface vertically, the current density vectors are normal to the interface and are equal in magnitude.

$$\boldsymbol{J}_{1n} = \sigma_1 \boldsymbol{E}_{1n} \quad \boldsymbol{J}_{2n} = \sigma_2 \boldsymbol{E}_{2n} \quad \boldsymbol{J}_{1n} = \boldsymbol{J}_{2n} \tag{2.42}$$

$$\boldsymbol{E}_{1n} = \boldsymbol{E}_n = \frac{\sigma_2}{\sigma_1} \boldsymbol{E}_{2n} \tag{2.43}$$

$$\frac{q_{ext1}}{q_{ext2}} = \frac{\sigma_2}{\sigma_1} \tag{2.44}$$

The result obtained in equation (2.44) is opposite to the relationship mentioned in equation (2.41).

#### 2.3.6.4 Refraction of the Current Density Flow at Boundaries

The external heat sources regarding their tangential and normal components absorbed per unit volume in two adjacent tissues are given by equations (2.45) and (2.46).

$$q_{ext1} = \frac{1}{2}\,\sigma_1\,|\boldsymbol{E}_1|^2 = \frac{1}{2}\,\sigma_1\boldsymbol{E}_{1t}^2 + \frac{1}{2}\,\sigma_1\boldsymbol{E}_{1n}^2 \tag{2.45}$$

$$q_{ext2} = \frac{1}{2}\,\sigma_2\,|\boldsymbol{E}_2|^2 = \frac{1}{2}\,\sigma_2\boldsymbol{E}_{2t}^2 + \frac{1}{2}\,\sigma_2\boldsymbol{E}_{2n}^2 \tag{2.46}$$

$$\boldsymbol{E}_{2n} = \frac{\sigma_1}{\sigma_2}\boldsymbol{E}_{1n} = \frac{\sigma_1}{\sigma_2}\boldsymbol{E}_n \tag{2.47}$$

$$q_{ext2} = \frac{1}{2}\,\sigma_2\,|\boldsymbol{E}_2|^2 = \frac{1}{2}\,\sigma_2\boldsymbol{E}_t^2 + \frac{1}{2}\,\sigma_1\frac{\sigma_1}{\sigma_2}\boldsymbol{E}_n^2 \tag{2.48}$$

Using the boundary condition given in equation (2.47), the ratio of the external heat sources absorbed in the tissues becomes:

$$\frac{q_{ext1}}{q_{ext2}} = \frac{\sigma_1\boldsymbol{E}_t^2 + \sigma_1\boldsymbol{E}_n^2}{\sigma_2\boldsymbol{E}_t^2 + \sigma_1\frac{\sigma_1}{\sigma_2}\boldsymbol{E}_n^2} \tag{2.49}$$

Equation (2.49) can be simplified based on various cases of conductivity distribution.

Case 1 ($\sigma_2 >> \sigma_1$):

$$\boldsymbol{E}_{1t} = \boldsymbol{E}_{2t} = \boldsymbol{E}_t = 0 \tag{2.50}$$

There is no tangential component of the electric field vector on either side of the interface. The ratio of the external heat source is expressed as follows:

$$\frac{q_{ext1}}{q_{ext2}} = \frac{\sigma_2}{\sigma_1} \tag{2.51}$$

In this case, a medium with a higher conductivity resulted in lower heating levels.

Case 2 ($\sigma_2 << \sigma_1$):

$$\boldsymbol{E}_{1n} = \boldsymbol{E}_{2n} = \boldsymbol{E}_n = 0 \tag{2.52}$$

There is no normal component of the electric field vector on either side of the interface. The ratio of the external heat source is expressed by equation (2.53).

$$\frac{q_{ext1}}{q_{ext2}} = \frac{\sigma_1}{\sigma_2} \tag{2.53}$$

It is shown that a medium with a higher conductivity leads to increased heating, in contrast to the result in equation (2.51).

#### 2.3.6.5 Incidence Angle and Refraction of Electric Field

Considering that the same power is transferred from medium-1 to medium-2, the refraction of the electric field can be calculated using equation (2.54).

$$\frac{q_{ext1}}{q_{ext2}} = \frac{\sigma_1 \boldsymbol{E}_t^2 + \sigma_1 \boldsymbol{E}_n^2}{\sigma_2 \boldsymbol{E}_t^2 + \sigma_1 \frac{\sigma_1}{\sigma_2} \boldsymbol{E}_n^2} = 1 \tag{2.54}$$

$$\sigma_1 \boldsymbol{E}_t^2 + \sigma_1 \boldsymbol{E}_n^2 = \sigma_2 \boldsymbol{E}_t^2 + \sigma_1 \frac{\sigma_1}{\sigma_2} \boldsymbol{E}_n^2 \tag{2.55}$$

$$(\sigma_1 - \sigma_2) \boldsymbol{E}_t^2 = (\sigma_1 - \sigma_2) \frac{\sigma_1}{\sigma_2} \boldsymbol{E}_n^2 \tag{2.56}$$

$$\frac{E_t}{E_n} = \sqrt{\frac{\sigma_1}{\sigma_2}} \tag{2.57}$$

The refraction of the current density vector was examined by applying equation (2.57) to various conductivity distributions.

Case-1 ($\sigma_1 = \sigma_2$ and $\theta_2 = 45°$): The current-density vector is propagated in an equal-conductivity medium. When the incident angle ($\theta_1$) was $45°$, the absorbed powers in both tissues were equal.

Case-2 ($\sigma_1 = 3\,\sigma_2$ and $\theta_2 = 45°$): The current density vector is propagated into a low-conductivity medium. When $\theta_1$ was $60°$, the absorbed powers in both tissues were equal.

Case-3 ($3\,\sigma_1 = \sigma_2$ and $\theta_2 = 45°$): The current density vector is propagated in a high-conductivity medium. When $\theta_1$ was $30°$, the absorbed powers in both tissues were equal.

The refraction was validated for these three cases in the Simulation Studies section.

# CHAPTER 3

# NUMERICAL STUDY

## 3.1 Numerical Model

This section presents the numerical model, relevant parameters, and the simulations. Tumorous breast tissue and coils in a 3-D geometry were modeled, and the magneto-thermal coupled problem was solved using COMSOL Multiphysics [105]. The electrical and thermal parameters, including metabolic heat and blood perfusion rate, are listed in Table 3.1. At the operating frequency, ($\omega\epsilon/\sigma$) was 0.123 for the tissue and 0.095 for the tumor. Electrical conductivity was dominant for heating, but the permittivity term was not ignored. Malignant breast tumors (malignant) can generate 10–50 times the metabolic heat of healthy tissues. The blood perfusion rate in tumors is high [4]. In the breast tissue model, 50% fat and 50% mammary glands are present. Most electrical and thermal parameters were obtained using the volumetric averaging method [81, 63].

The tissue model was 66 mm in diameter and 10 mm in height, as shown in Figure 3.1a. The diameter and height of the tumors were 10 mm. One millimeter of the tissue model was placed above the coil's upper surface, with a 9 mm length inside the coil. As shown in Table 3.1, the healthy tissue and tumor conductivities were assigned values of 0.3 $\mathrm{S/m}$ and 0.75 $\mathrm{S/m}$, respectively.

The coil was formed using a homogenized multiturn coil feature in COMSOL with 11 turns, as shown in Figure 3.1b. The diameter of each parallel closed loop in the multiturn coil was 5 mm. The coil current values were selected based on the limitations of SAR values determined by the International Electrotechnical Commission (IEC). The SAR value (10 $\mathrm{W/kg}$ for a 10 g mass) was calculated for the cubic phantom using

Table 3.1: Electrical and thermal parameters of breast tissue, tumor, and blood [4, 73, 78, 79, 80, 106, 107, 108, 109].

| **Parameters** | **Unit** | **Tissue** | **Tumor** |
|---|---|---|---|
| **Conductivity** | S/m | 0.3 | 0.75 |
| **Specific heat** | J/kg K | 2700 | 3850 |
| **Density** | $\mathrm{kg/m^3}$ | 950 | 980 |
| **Thermal conductivity** | cal/s °C | 0.45 | 0.45 |
| **Relative permittivity** | – | 885 | 1700 |
| **Blood perfusion rate** | $\mathrm{s^{-1}}$ | 0.0002 | 0.009 |
| **Blood temperature** | °K | 310 | 310 |
| **Specific heat of blood** | J/kg K | 3770 | 3770 |
| **Blood density** | $\mathrm{kg/m^3}$ | 1020 | 1020 |
| **Metabolic heat source** | $\mathrm{W/m^3}$ | 750 | 22 000 |

the selected coil at 750 kHz. Similarly, the IEC's local body temperature limit owing to electromagnetic field exposure is 40 °C [110]. In the simulation studies, the body core temperature was set to 37 °C, and we aimed to maintain the body temperature increase below 3 °C. A heating time of 12 min was used for the simulations.

The tumor volume doubling time (TVDT) was between 126–170 days before age 60. Tumor volume doubling time and diameter parameters are required to calculate the metabolic heat source [111].

The tumor volume doubling time ($t_d$) is calculated using the following equation [112]:

$$D = 0.01\, e^{\,0.002134\,(t_d-50)} \tag{3.1}$$

$D$ is the tumor diameter (mm). For the calculation of metabolic heat source ($q_m$), the following relationship can be used: $q_m \times t_d = C$, where $C$ is a constant ($3.27 \times 10^6$ $\mathrm{W\ day/m^3}$).

## 3.2 Simulations of IC-ETI Method

### 3.2.1 Solenoid Concentric Coil Encircling a Cylindrical Body

The in vivo conditions were modeled in the first simulation using a 3-D cylindrical body. Figure 3.1 shows a cylindrical tissue model within a concentric coil. The coil current was 51 A for a 10 W/kg SAR value (for a 10 g mass; 66 mm diameter and 3.1 mm length cylinder volume on the upper side of the phantom) in the coil body geometry, as shown in Figure 3.1.

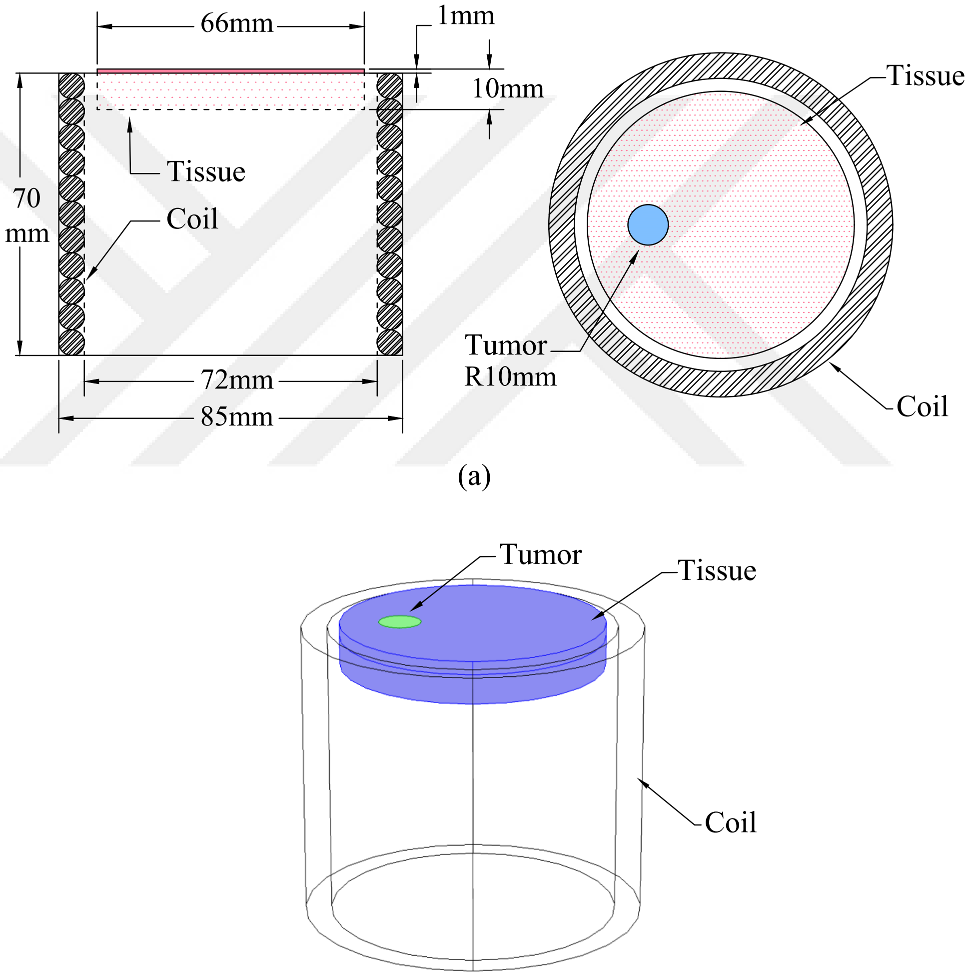

(a)

(b)

Figure 3.1: Geometry of cylindrical tissue model within concentric coil simulation. (a) Front and top views from left to right. (b) The cylindrical tissue model and uniform coil geometry in 3-D.

Bio-heat transfer, ACDC module MF (magnetic fields), and induction heating in the frequency transient mode were used with COMSOL Multiphysics [105]. Figure 3.2a illustrates the generated mesh structure. Figure 3.2b shows the current density and vector distribution.

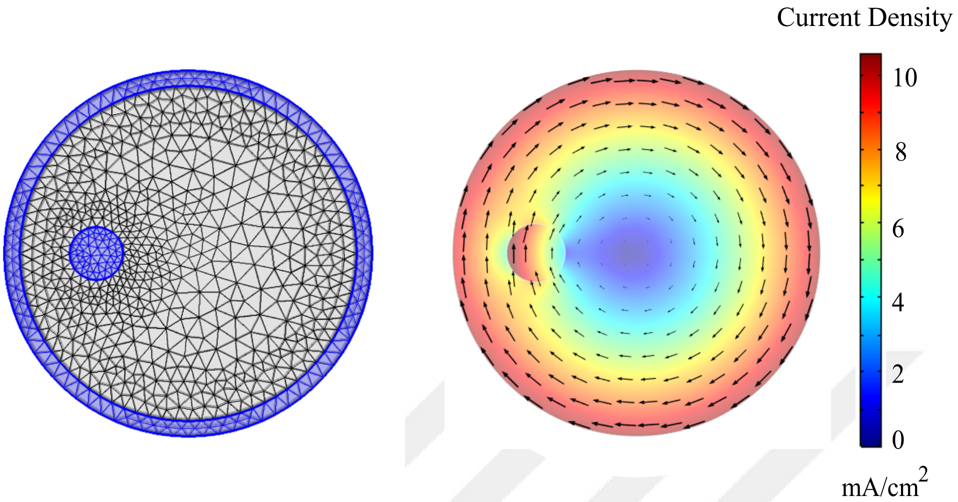

(a)

(b)

Figure 3.2: (a) Mesh structure utilized for the cylindrical geometry. (b) Distribution of current density vector for body surface.

Figure 3.3a illustrates the surface temperature distribution when only metabolic heat sources were present (passive mode). The surface temperature distribution in the active mode (formed with external and metabolic heat sources) is shown in Figure 3.3b. The temperature distribution in the active mode was determined mainly by the applied magnetic fields, conductivity distribution, and specific heat differences between the tumor and healthy tissues. The temperature increase in the tumor was also limited because of its higher specific heat value. The current density distribution due to the conductivity inhomogeneity is shown in Figure 3.3c. The current density was higher on the left inner side of the tumor and lower on the left outer boundary. The circular symmetry of the induced current density was perturbed because the conductivity of the malignant tumor was higher than that of healthy breast tissue.

The current density enters the tumor almost normally in the upper and lower parts, resulting in a local increase in the magnitude of the heat outside the tumor. However, there was a drop in this magnitude on the left-hand side of the tumor, where the

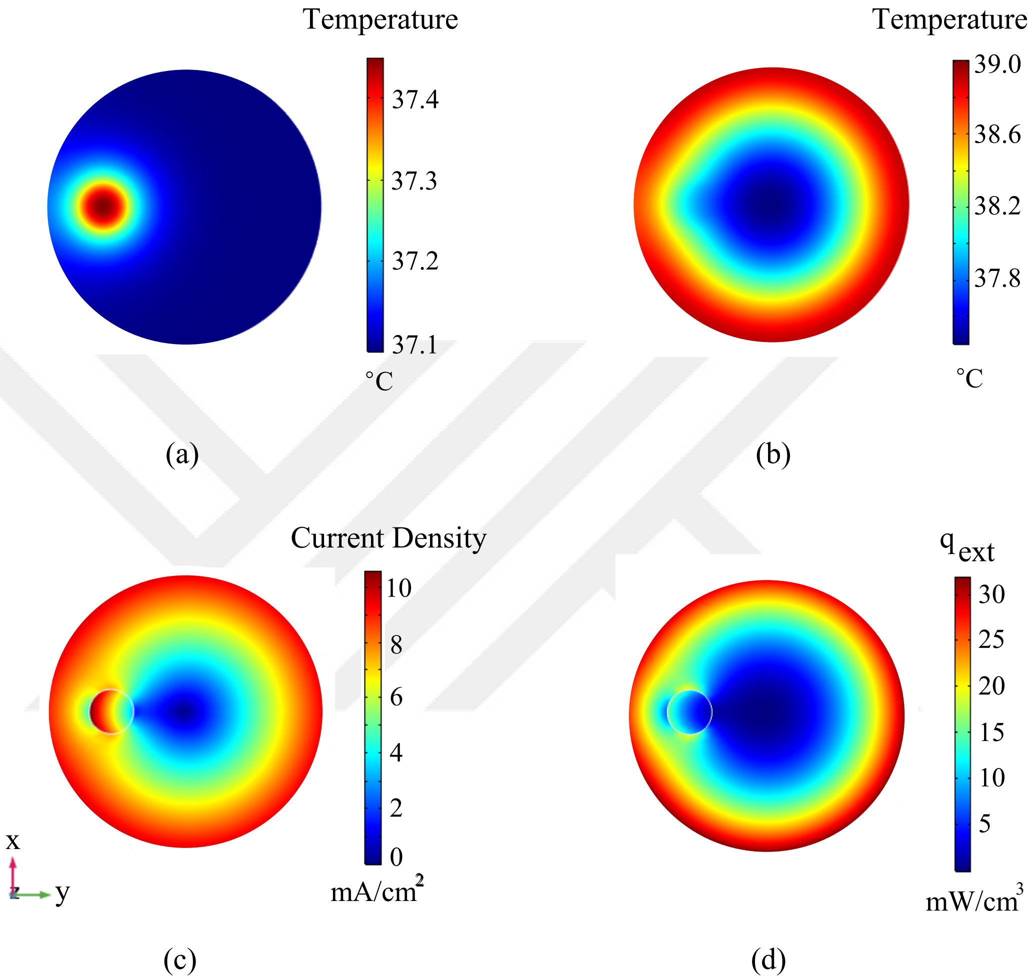

(a) (b)

(c) (d)

Figure 3.3: (a) Surface temperature distribution of tumorous phantom in passive mode. (b) Surface temperature distribution of tumorous phantom in active mode. (c) Current density distribution, $|\boldsymbol{J}|$ $(\mathrm{mA/cm^2})$ on the surface for 51 A (750 kHz) current. (d) External heat source distribution $q_{ext}$ $(\mathrm{mW/cm^3})$.

current density was mainly tangential. The external heat source ($q_{ext}$) distribution is shown in Figure 3.3d. $q_{ext}$ is generally lower inside the tumor, whereas its magnitude changes around the tumor boundary.

### 3.2.2 Solenoid Coil on a Cubic Body

The second simulation simulated in vivo conditions, including the metabolic heat and blood perfusion rates at body temperature (37 $^{\circ}\mathrm{C}$). Figure 3.4a shows a cubic body placed 2.5 mm below the homogenized multiturn coil (the coil used in the first simulation study). The maximum current that could be applied to the coil was 60.5 A for a 10 g mass (2.19 cm is the cube's dimension used for the SAR calculation) in the coil-body geometry shown in Figure 3.4a. Figure 3.4b shows the tumor location in the (y = 2 cm) plane. The resulting temperature distribution is shown in Figure 3.4c.

The temperature rise graphs for the active and passive modes at different measurement positions are shown in Figure 3.4d. The tumor depth (distance between the tumor center and the y = 0 plane) was kept constant at y = 2 cm. The temperatures were measured at different depths, that is, along the dashed line (4.25 cm, y, 1.25 cm), as shown in Figure 3.4a. In the passive mode, a temperature rise of 0.4 $^{\circ}\mathrm{C}$ emerged at the center of the 1 cm$^3$ tumor (with the tumor's metabolic heat source, $q_m$ = 22 000 $\mathrm{W/m^3}$). In the active mode, the temperature increased near the body surface because larger currents were induced near the coil. The temperature rise decreased as the measuring point got closer to the coil axis.

The temperature differences due to the tumor depth were also investigated. Because the IR camera displayed the temperature distribution on the y = 0 plane, the tumor depth changed along the y-axis (with respect to the image plane). The tumor center was (4.25 cm, $y_c$, 1.75 cm), and $y_c$ varied between 1 cm and 3 cm. In each case, the measurement point was fixed at (4.25 cm, 0 cm, 1.25 cm) location on the tissue surface. Figure 3.4e shows the temperature differences relative to the reference temperature at the same location when a tumor-free distribution was used [113]. A larger contrast was observed when the tumor was located near the surface. The contrast decreased as the tumor depth increased because the induced current density decreased with depth. The NETD of standard IR cameras with uncooled detectors ranges be-

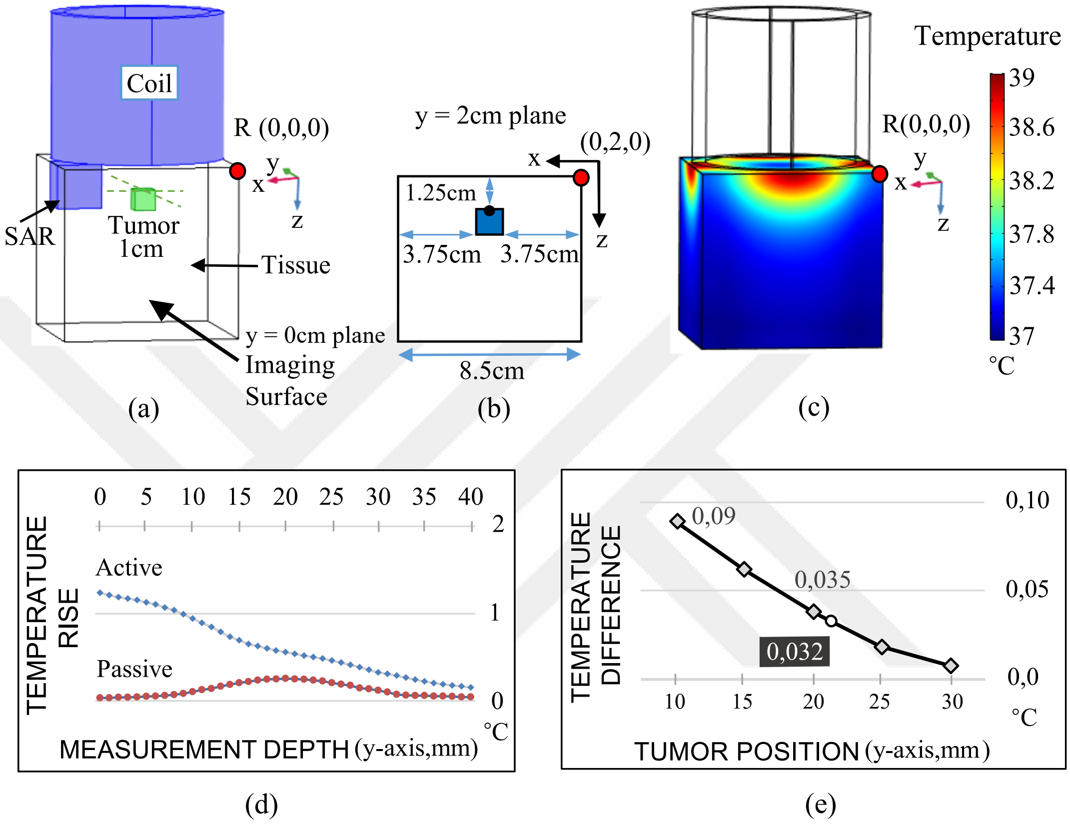

Figure 3.4: (a) Cubic breast model and uniform cylindrical coil. (b) The position of the tumor in the y = 2 cm plane. (c) The temperature distribution on the surface for the y = 0 cm plane. (d) The temperature rise of active and passive modes at different measurement locations (y: 0–40 mm). (e) The temperature differences at different tumor depths.

tween 20 °mC and 50 °mC. In the simulation studies, we assumed that the NETD of the camera is 30 °mC. Consequently, with the assumed NETD and metabolic heat source, the tumor could be detected at a 1.7 cm depth (distance between the tumor center and y = 0 plane) in the passive mode. However, tumors of the same size were detected at a 2.1 cm depth in the active mode.

#### 3.2.2.1 Other Plots for the Cubic Phantom

The temperature differences in the tumor slices and at the tissue surface are shown in Figures 3.5 and 3.6, respectively. Notably, the rise of temperature decreases after 12-15 minutes. The surface temperatures were measured at various tumor locations along the y-depth, and the temperature differences between the active and passive cases were graphically represented. The position of the tumor was altered, ranging from $y = 5$ mm to 35 mm, and $z = 10$ mm to 25 mm, as illustrated in Figure 3.7.

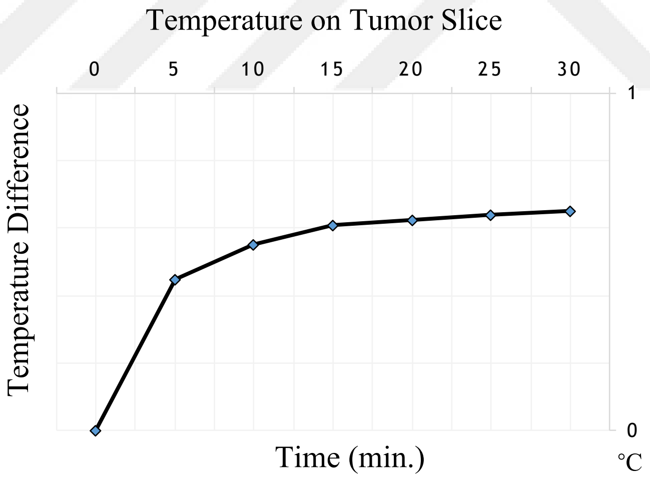

Figure 3.5: The thermal response of the tissue, the variation in temperature over time within the tumor slice.

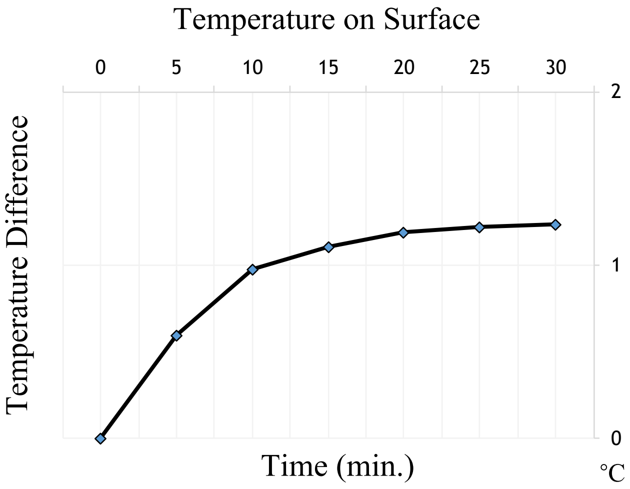

Figure 3.6: The surface temperature differences with time, resulting from the presence of a tumor (tumor is at z = 10 mm).

YÖK

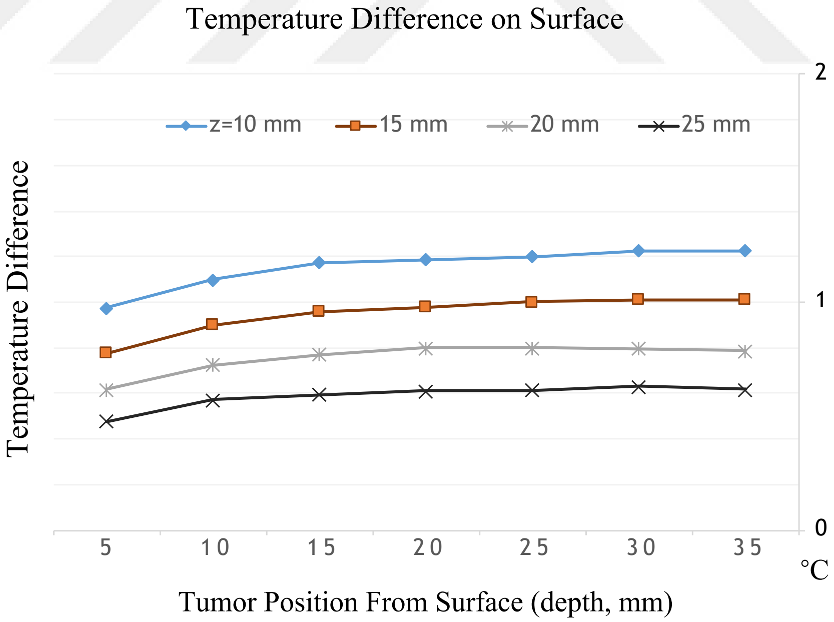

Figure 3.7: Temperature differences were measured for tumors situated at various depths along the y-axis (y = 5 mm to 35 mm.)

As shown in Figure 3.5, the temperature difference in the tumor section initially exhibited a rapid increase and subsequently leveled off after 12 min. It is worth noting that the temperature increase observed on the surface in Figure 3.6 is higher than that of the tumor section owing to the distance from the coil. Similarly, the increase in temperature was sustained for 12-15 min. As shown in Figure 3.7, the measured temperatures varied depending on the position of the tumor along the z-axis. Notably, the external temperature increased as the tumor approached the coil. The temperature rise curves were parallel and compatible. As the tumor moved away from the coil, the temperature measured on the outer surface decreased, as expected. In conclusion, the time required to heat the tumorous tissue was more than 10 min, and the temperature difference at the surface decreased as the depth of the tumor increased and the tumor moved away from the coil.

## 3.3 Simulations of Induced Current and Refraction

Numerical results were analyzed for various conductivity contrasts, including current density distribution, external power transfer, and temperature distribution, through numerical studies. In addition, the refraction of the induced current density vector was investigated.

### 3.3.1 Numerical Model for Induced Current and Refraction

The coil, consisting of parallel loops of wires, was numerically energized to produce an induced current below 1 MHz within a cubic breast tumor model while considering the local SAR values and temperature limitations [110].

The solenoid coil created a circular current density distribution within homogeneous tissue, with a null point at its center. This study explored the normal and tangential components of the current density vector and their effects on tumorous tissues and the surrounding regions.

In the simulation study, we utilized the same metabolic heat sources and blood perfusion rates for both tissue-1 and tissue-2 to demonstrate the effect of an externally applied electromagnetic heat source. The breast tissue model comprises equal percentages of fat and mammary gland tissues. Volumetric averaging was employed to determine the electrical parameters of the tissue [81, 63]. The electrical and thermal parameters used in the simulations are listed in Table 3.2.

Table 3.2: The electrical and thermal parameters for tissue-1, tissue-2, and blood were used in the numerical model to simulate the induced current and refraction [4, 73, 78, 79, 80, 106, 107, 111].

| **Parameter** | **Unit** | **Tissue 1** | **Tissue 2** |
|---|---|---|---|
| **Electrical conductivity** | S/m | 0.3 | 0.9 |
| **Relative permittivity** | – | 885 | 1700 |
| **Relative permeability** | – | 1 | 1 |
| **Specific heat** | J/kg K | 2700 | 2700 |
| **Density** | $kg/m^3$ | 950 | 950 |
| **Blood perfusion rate** | 1/s | 0.0002 | 0.0002 |
| **Metabolic heat source** | $W/m^3$ | 750 | 750 |

The tissue model is a cubical geometry with dimensions of 50 mm and was 10 mm deep, as shown in Figure 3.8. The right-hand side of the tissue is called tissue-1 (healthy tissue) in Figure 3.8b, whereas the adjacent side is called tissue-2 (tumorous tissue). The conductivity of tissue-1 was set as 0.3 S/m, whereas the conductivity of tissue-2 changed in each simulation. The results of the simulations, depending on the conductivity contrast between tissue-1 and tissue-2, are shown in Figures 3.9, 3.10 and 3.11.

A homogenized multiturn coil was formed with ten turns, as shown in Figure 3.8a. The diameter of each parallel closed loop was 6 mm. The current applied to the coil was determined by considering the SAR value limitations set by IEC. The SAR value (10 W/kg) was computed using cubical phantom geometry. The exposure time of the coil was 10 min. The core body temperature was set at 37 °C, and the IEC's local body temperature limit owing to electromagnetic field exposure was 40 °C [110].

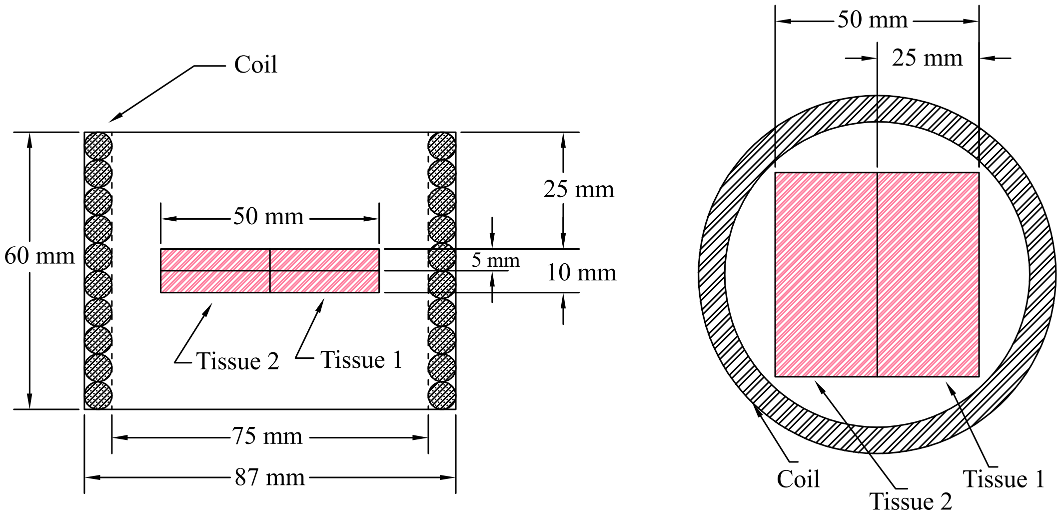

(a) (b)

Figure 3.8: (a) Front view of the tissue model (tissue-1, tissue-2) with excitation coil geometry. (b) Top view of tissue model and coil geometry.

#### 3.3.1.1 Current Density Flow and Externally Induced Power

The 3-D rectangular tissue geometry was excited using the in vivo parameters. The tissue model was then placed in a concentric coil.

Figure 3.9 shows the results when 44 A was applied to the coil with a 10 W/kg SAR value in tissue-1 and tissue-2. The conductivity values were $\sigma_1 = 0.3$ S/m and $\sigma_2 = \sigma_1$.

Figure 3.10 shows the results when 34 A was applied to the coil with a 10 W/kg SAR value in tissue-1 and tissue-2. The conductivity values were $\sigma_1 = 0.3$ S/m and $\sigma_2 = 3\,\sigma_1$.

Figure 3.11 shows the results when 23.5 A was applied to the coil with a 10 W/kg SAR value in tissue-1 and tissue-2. The conductivity values were $\sigma_1 = 0.3$ S/m and $\sigma_2 = 10\,\sigma_1$.

The direction of the current density vector did not change when it entered the boundary in the vertical direction as it passed from the first medium to the second medium. However, if the current density vector angle is close to zero, it refracts and cannot pass to the second medium. The amount and direction of refraction of the current density vector vary depending on the conductivity contrast between tissue layers. In Figure 3.9, it is observed that there is no refraction in the current density. However, refraction is evident in Figure 3.10. Furthermore, Figure 3.11 illustrates that the current density forms a closed loop in the area of high conductivity.

In the region where the current density is close to the right angle, the current density accumulates in one area because of refraction and unwanted hotspot regions are formed. Determining the refraction angles of current density vectors and concentration zones is possible using knowledge of the electrical properties of the tissues surrounding a tumor.

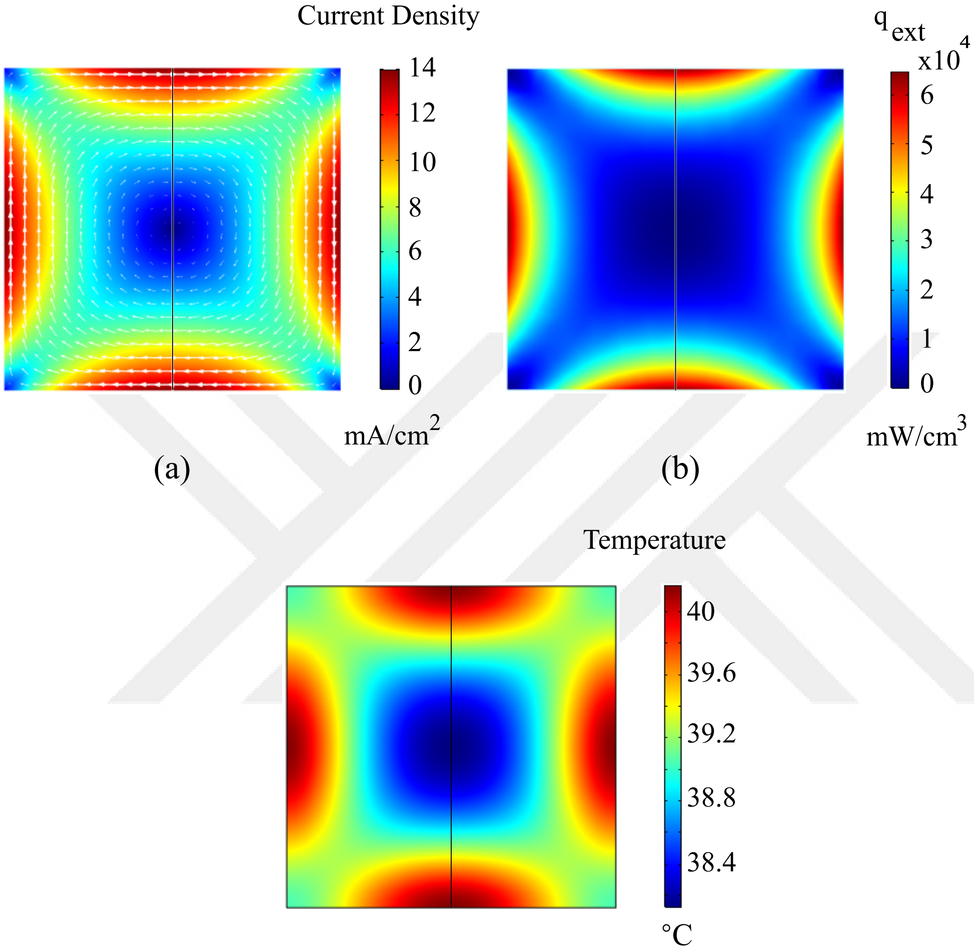

(a) (b)

(c)

Figure 3.9: Case 1: The current density vector enters the equally conductive region ($\sigma_1 = \sigma_2$). (a) Current density distribution, $|\boldsymbol{J}|$ (mA/cm$^2$) at a depth of 5 mm. (b) External heat-source distribution $q_{ext}$ (mW/cm$^3$) at a depth of 5 mm. (c) Temperature distribution at 5 mm depth owing to induced currents (in active case).

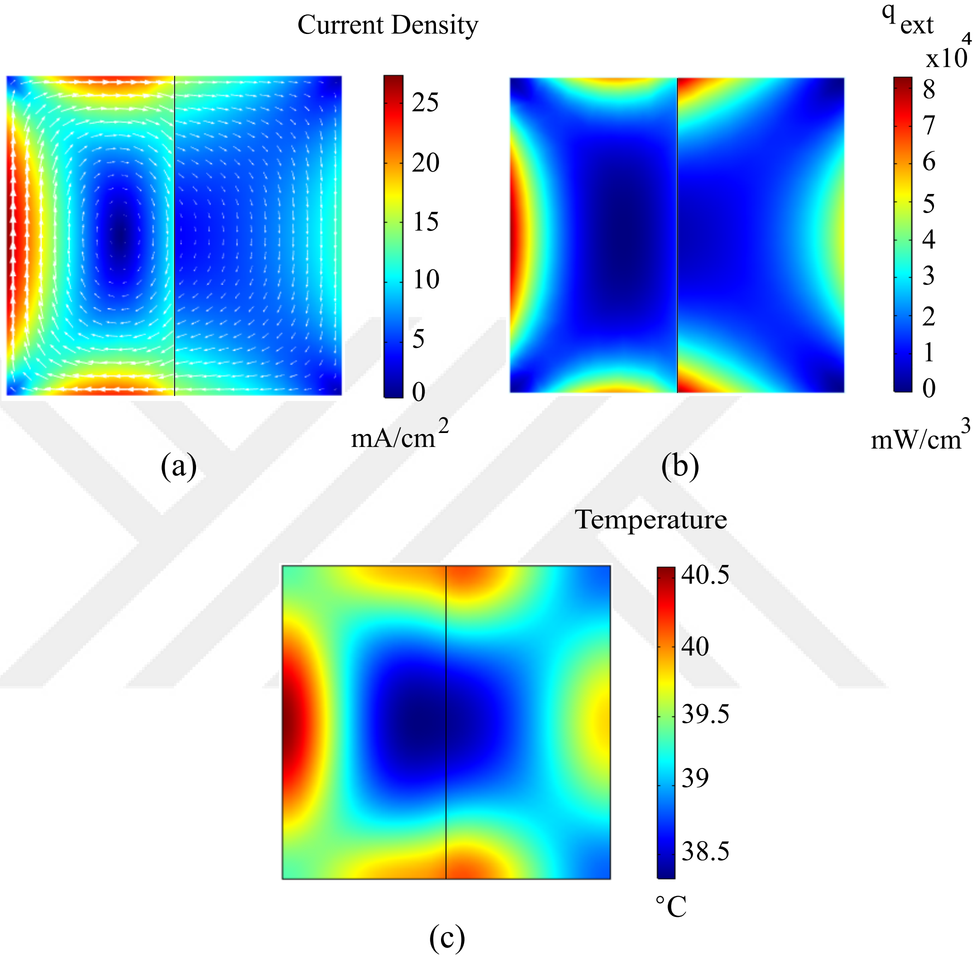

(a) (b) (c)

Figure 3.10: Case 2: The current density vector enters the higher conductivity region ($\sigma_2 = 3\,\sigma_1$). (a) Current density distribution, $|\boldsymbol{J}|$ (mA/cm$^2$) at a depth of 5 mm. (b) External heat-source distribution $q_{ext}$ (mW/cm$^3$) at a depth of 5 mm. (c) Temperature distribution at 5 mm depth owing to induced currents (in active case).

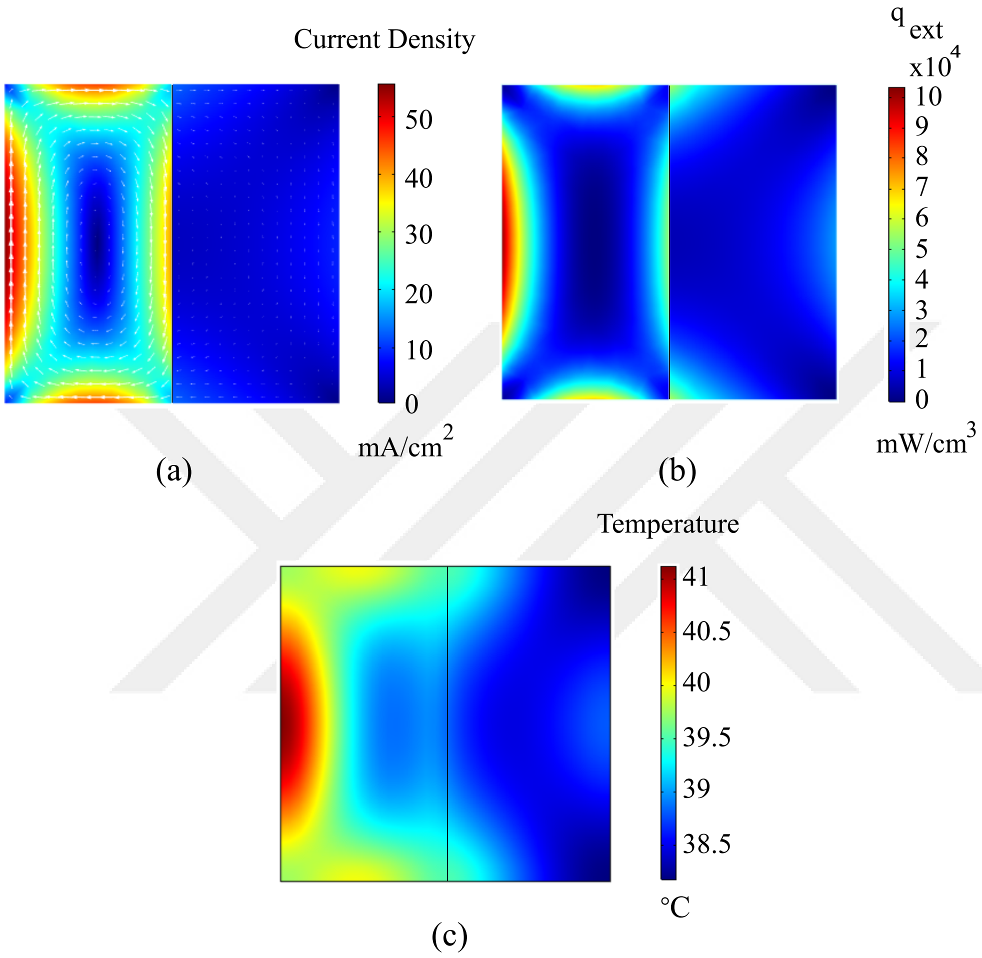

(a) (b)

(c)

Figure 3.11: Case 3: The current density vector enters the higher conductivity region ($\sigma_2 = 10\,\sigma_1$). (a) Current density distribution, $|\boldsymbol{J}|$ (mA$/$cm$^2$) at a depth of 5 mm. (b) External heat-source distribution $q_{ext}$ (mW$/$cm$^3$) at a depth of 5 mm. (c) Temperature distribution at 5 mm depth owing to induced currents (in active case).

#### 3.3.1.2 Current Density Refraction

Considering equal power-transfer locations, the input angle ($\theta_1$) was determined according to the situation in which the output angle $\theta_2$ was 45°. Equal power transfer locations were specified at the tissue-1 tissue-2 boundary. The refraction of the current densities of the three cases described in Chapter 2 (In the Incidence Angle and Refraction of Electric Field Section) was validated for the three cases. The simulation results are shown in Figure 3.12.

Case 1 ($\sigma_1 = \sigma_2$): The current density vector propagates into the equal-conductive region. There was no refraction in this case, and the power transfer was equal across the entire tissue-1 tissue-2 boundary.

Case 2 ($\sigma_1 = 3\,\sigma_2$ and $\theta_2 = 45°$), and the current density vector propagates into the lower conductive region. The external powers are equal when $\theta_1 = 60°$ and $\theta_2 = 45°$.

Case 3 ($3\,\sigma_1 = \sigma_2$ and $\theta_2 = 45°$), and the current density vector propagates into the higher-conductivity region. The external powers are equal when $\theta_1 = 30°$ and $\theta_2 = 45°$.

When the current density vector enters a more conductive region, it is refracted, and the $J_{2n}$ component decreases. The $J_{2t}$ component increases in the region with higher conductivity. In contrast, the $J_{2t}$ component decreased when the current density vector entered the lower conductive medium. The $J_{2n}$ component increased in a medium with lower conductivity.

The temperature increase in the tumor was confined owing to its higher specific heat value. As shown in Figure 3.13, the specific heat contrast significantly influences the temperature increase at the outer boundary of the tumor, particularly in the hotspot region. Similarly, the density contrast of tissues amplifies the temperature difference in the hotspot region.

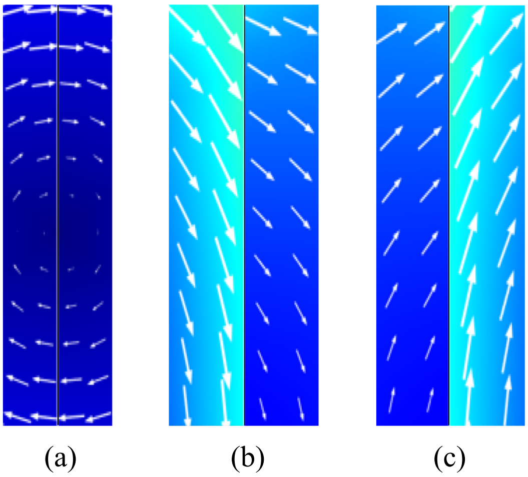
(a) (b) (c)

Figure 3.12: Current density refraction at the tissue-1 and tissue-2 boundaries for the three conductivity contrasts. (a) Case-1, when $\sigma_1 = \sigma_2$. (b) Case-2, when $\sigma_1 = 3\,\sigma_2$ and $\theta_2 = 45°$. (c) Case-3, when $3\,\sigma_1 = \sigma_2$ and $\theta_2 = 45°$.

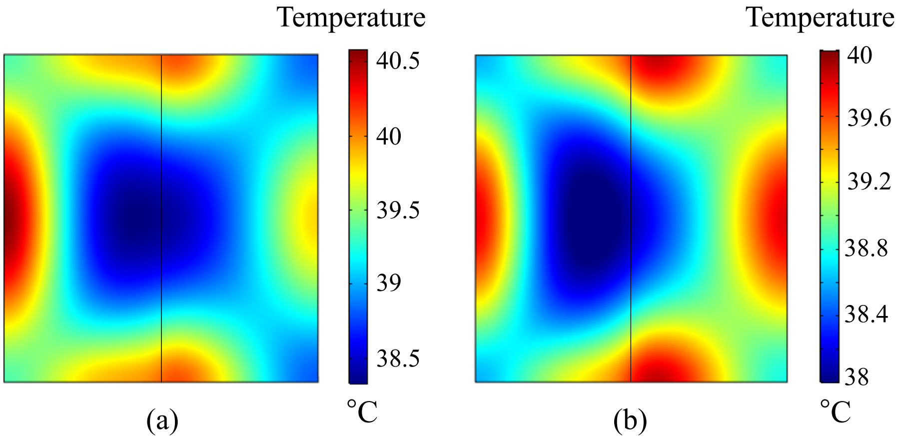

(a) (b)

Figure 3.13: (a) Temperature distribution owing to the specific heat contrast of case-1 ($c_1 =$ 2700 J/kg K, and $c_2 =$ 2700 J/kg K). (b) Temperature distribution owing to the specific heat contrast of case-2 ($c_1 =$ 2700 J/kg K, and $c_2 =$ 3850 J/kg K).

The refraction of the propagation direction depends on the electrical parameters of the tumor and surrounding layers, as governed by Snell's law, for plane-wave frequencies. When a plane wave enters a medium with a high refractive index, the refraction angle along the normal axis decreases. In our case, in which a magnetic field was applied using a solenoid coil, we examined the refraction of the current density vector using the boundary conditions and electrical parameters of the tissue layers. In this scenario, the refraction angle of the current density vector increases when it enters a more conductive or permittivity medium, such as a tumorous tissue.

## 3.4 Simulation of Realistic Breast Model

The physical structure of the breast can be modeled using a cylinder or hemisphere to form a more realistic geometry. The surface temperature distribution was obtained by stimulating the modeled tumor breast with a 25-turn Helmholtz coil with a current of 4 A at 750 kHz. The geometry of the breast model is illustrated in Figure 3.14.

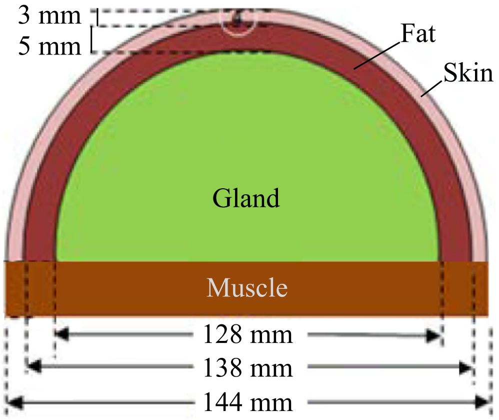

Figure 3.14: Realistic breast model (semi-spherical) with skin, muscle, fat, and gland layers [114].

In this simulation, the geometry of the breast was modeled as a hemisphere using a layered tissue structure. This model has skin, fat, and gland layers; each tissue layer has its own separate electrical and thermal parameters. The simulation parameters are listed in Table 3.3.

Table 3.3: Electrical and thermal parameters of breast tissues and tumor [4, 73, 78, 79, 80, 106, 107, 108, 109].

| **Parameters** | **Unit** | **Muscle** | **Skin** | **Fat** | **Gland** | **Tumor** |
|---|---|---|---|---|---|---|
| **Conductivity** | $\mathrm{S/m}$ | 0.48 | 0.008 | 0.025 | 0.58 | 0.75 |
| **Specific heat** | $\mathrm{J/kg\ K}$ | 3421 | 3391 | 2348 | 2960 | 3850 |
| **Density** | $\mathrm{kg/m^3}$ | 1090 | 1109 | 911 | 1028 | 980 |
| **Thermal conductivity** | $\mathrm{cal/s}\ ^{\circ}\mathrm{C}$ | 0.49 | 0.37 | 0.21 | 0.44 | 0.45 |
| **Relative permittivity** | $-$ | 2500 | 1030 | 26 | 1740 | 1700 |

Figure 3.15 shows the breast model and the simulation results. The use of a Helmholtz coil pair offers several advantages. It reduces the current flow through each coil and allows a greater tissue volume to be heated simultaneously. Additionally, the coils were more sensitive in the areas between and close to them. However, the electric field strength varies depending on the distance from the coil, as shown in Figure 3.15d. Despite this, the low conductivity values of the skin and fat tissue resulted in a lower current density induced in these tissues, as shown in Figure 3.15e. Consequently, the temperature increase was less in the skin and fat tissue and more remarkable in the gland tissue, as shown in Figure 3.15c. Figure 3.15b shows the asymmetry of the isotherm–temperature curves. The stimulation parameters and coil geometry should be optimized to utilize the Helmholtz coil in multilayer tissue models effectively.

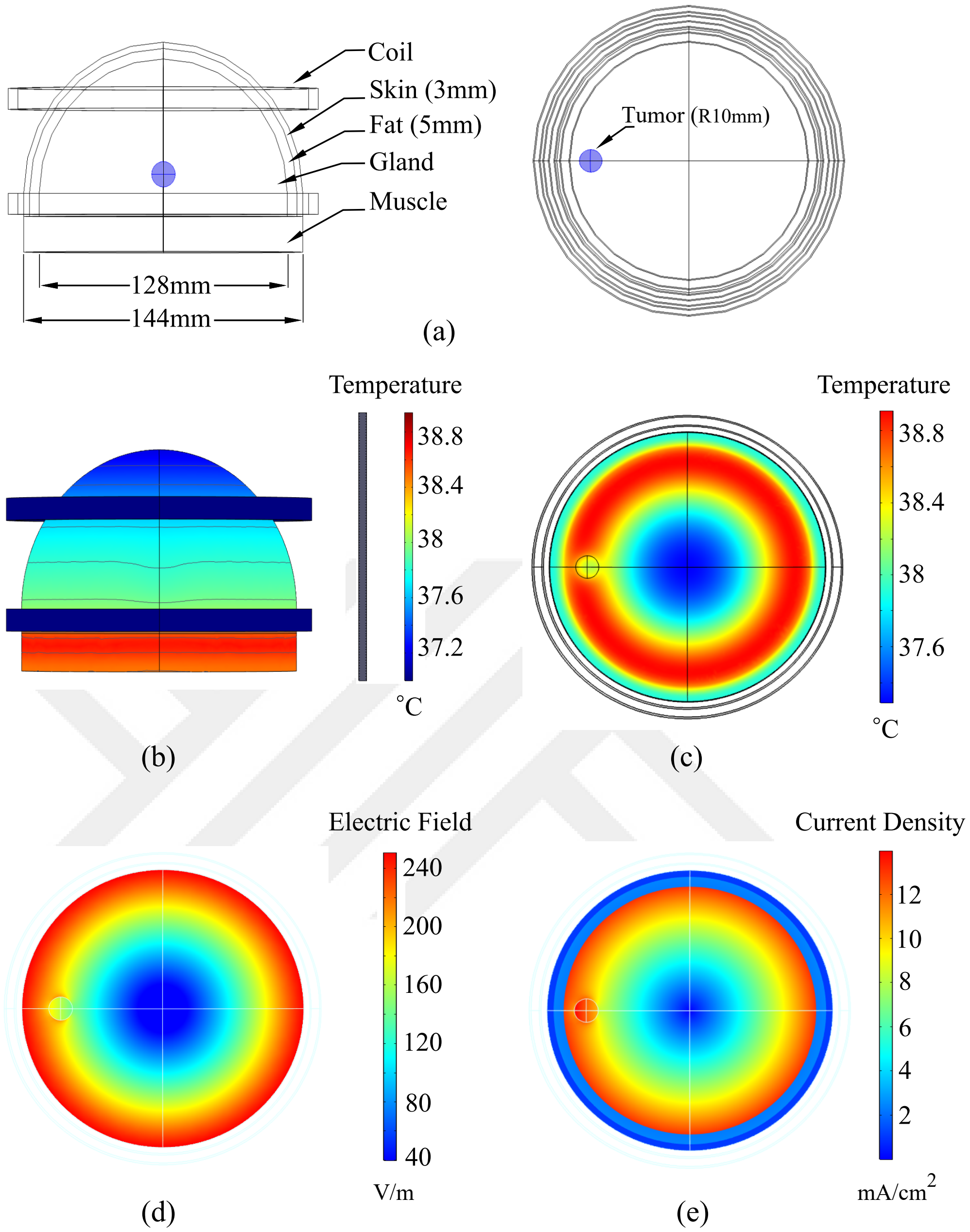

Figure 3.15: (a) Semi-spherical breast model with skin, muscle, fat, and gland layers. (b) Temperature distribution on the spherical surface of the semi-spherical breast model. (c) Temperature distribution of tumor slices (at 12 min). (d) Electric field distribution of the tumor center slice. (e) The electrical current density of the tumor center slice.

YÖK

# CHAPTER 4

# EXPERIMENTAL STUDY

We conducted experiments using solenoid and multilayer coils to investigate the temperature distributions of tumor-free and tumorous breast phantoms. In the first experiment, a solenoid coil encircling a cylindrical phantom with a surface tumor was used to investigate the basic properties of the method, as shown in Figure 4.1a. The second experiment utilized a cubical phantom and solenoid coil, as shown in Figure 4.1b, to test the depth performance of the method. Finally, the third experiment used a large-diameter eccentric multilayer coil encircling a cylindrical phantom for practical applications, as shown in Figure 4.1c.

(a) (b) (c)

Figure 4.1: Experimental setups. (a) Solenoid concentric coil encircling the cylindrical phantom. (b) Solenoid coil above the cubic body. (c) Multilayer eccentric coil encircling the cylindrical phantom.

The experiments were performed in a temperature-regulated environment (approximately 22 °C). The light level in the room remained constant during imaging. The IR camera used in the experiments had a long-wave uncooled microbolometer sensor with a 320×240 pixel resolution and a noise-equivalent temperature difference (NETD) of 40 °mC. The spectral range of the camera is 7.5–13 µm, as listed in Table 4.1.

Table 4.1: Technical specifications of the IR thermal camera used in the experiments [115].

| **Parameter** | **Unit** | **Property** |
|---|---|---|
| **Detector Type** | – | Microbolometer |
| **Resolution** | pixel | 320×240 |
| **Dynamic Range** | bit | 14 |
| **NETD** | °mC | 40 |
| **Spectral Range** | µm | 7.5–13 |
| **Focus Distance** | cm | 40 |
| **Max Frame Rate** | Hz | 60 |

In the experimental setup illustrated in Figures 4.1a and 4.1c, the distance between the IR camera and phantom was 90 cm. In the setup shown in 4.1b, the distance between the phantom and the camera was 100 cm. Additionally, a Styrofoam board was placed behind the cubic phantom to provide thermal insulation, and a thermal insulation rubber was positioned between the phantom and coil in all setups.

## 4.1 Voltage Amplifier

An input voltage was applied to the broadband (0–800 kHz) AB-class voltage amplifier (AL-1400-HF-A) to drive the coil, as shown in Figure 4.3. The amplifier, with a gain of 14, increased the input voltage (0–2 $V_{rms}$) fed by the signal generator to the output voltage (0–28 $V_{rms}$). The output power was shared equally by the four amplifiers, which divided the output currents. The power was converted to 55 V in direct current (DC) and inverted using FETs in the amplifier modules, as shown in Figure 4.2. The amplifier's output impedance is negligible because it is close to zero. The output current was obtained by adjusting the output impedance.

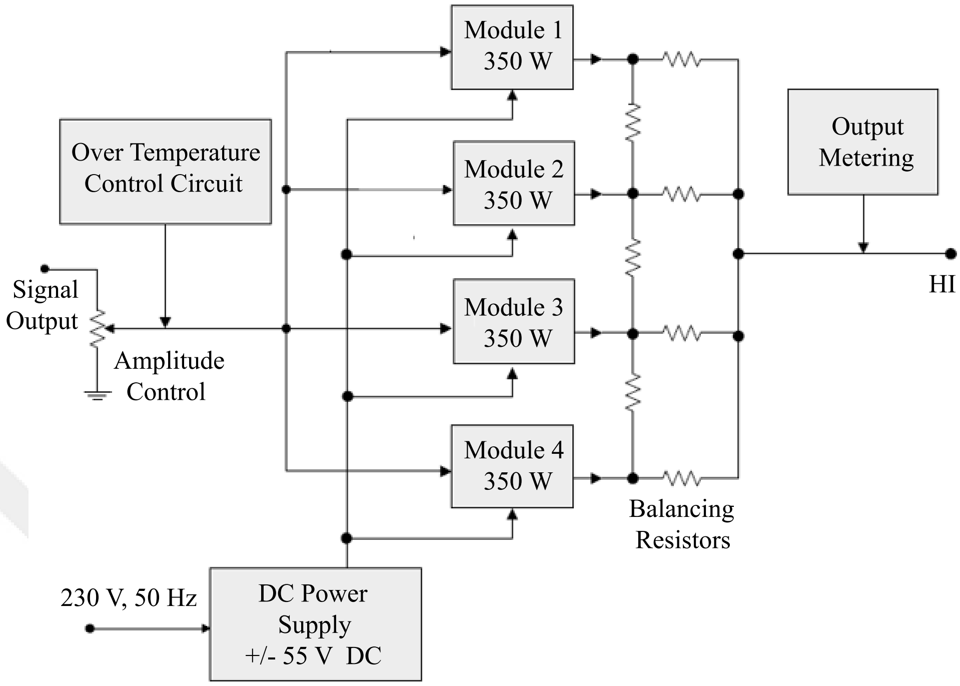

Figure 4.2: The Ampline-1400 W voltage amplifier's block diagram; FET modules, control units, and input and output components [116].

## 4.2 Coils for the Experimental Setup

The initial two experiments utilized an 11-turn solenoid coil with a wire length of 70 mm, coil inner diameter of 72 mm, and coil wire diameter of 5 mm. The coil was wound using a non-insulated pure copper wire. Before winding, the wire was insulated with an external plastic insulation sheath. The solenoid coil inductance was measured to be 6.25 μH. A low equivalent series resistance (ESR) ceramic capacitor group with an equivalent capacitance of 7.3 nF tuned the coil, resulting in resonance at 745 kHz. A resistor group was formed using 50 W power resistors to control and measure the current applied to the coil.

A 5-layer, 12.5 cm inner diameter, 23-turn solenoid coil was equipped for the third ex-

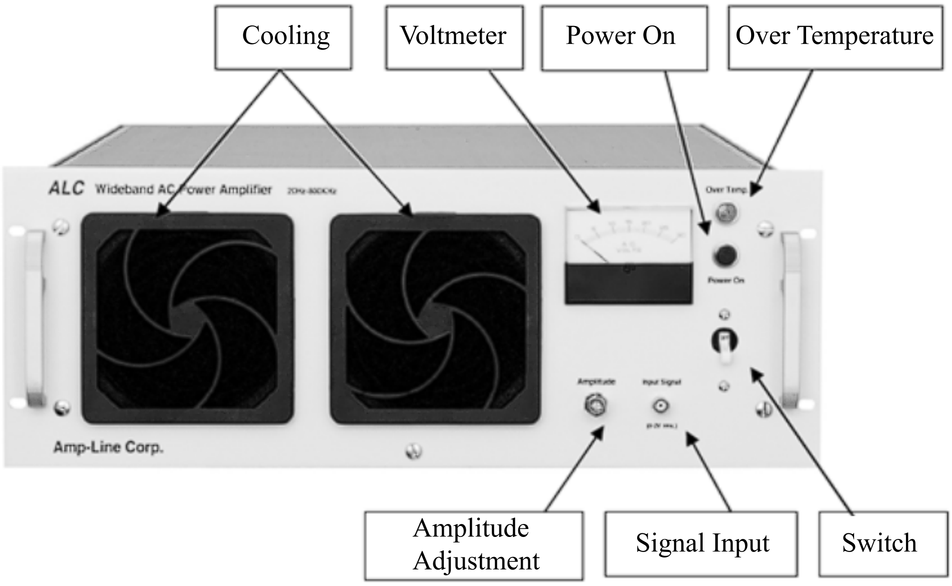

Figure 4.3: Ampline-1400 W voltage amplifier and user interface [116].

periment. Using a multilayer coil geometry reduced the current required to energize the coil. However, an increase in the coil diameter results in increased inductance, making applying the necessary current to the coil circuit more challenging. The diameter of the coil wire was 2 mm, and the inductance of the multilayer coil was measured to be 119.8 μH. Resonance was acquired through the serial connection of a capacitor group to the coil with an equivalent capacitance of 0.37 nF at 755 kHz.

### 4.2.1 Inductance of the Solenoid Coil

R. Weaver's inductance calculation method was employed to evaluate the inductance of the solenoid coil [117]. Equation (4.1) calculates the inductance of an air-core solenoid coil $L_{coil}$ (μH) for a given number of turns, loop diameter, and wire diameter.

$$0.002\,\pi D N^2 \left[ In\left(1+\frac{\pi D}{2l}\right) + \left(2.3 + 3.437\frac{l}{D} + 1.76\left(\frac{l}{D}\right)^2 - \frac{0.47}{\left(0.75+\frac{D}{l}\right)^{1.44}}\right)^{-1} \right] \tag{4.1}$$

In equation (4.1), $N$ is the number of turns (11), $D$ is the inner diameter of the loop

(72 mm), and $d$ is the wire diameter (5 mm). The inner coil diameter was 7.2 cm, and the outer coil diameter was 8.2 cm. The diameter of the pure copper wire was 5 mm, and that of the insulated wire was 6.3 mm. The coil length, $l$ was 70 mm, and the calculated inductance was 6.65 μH.

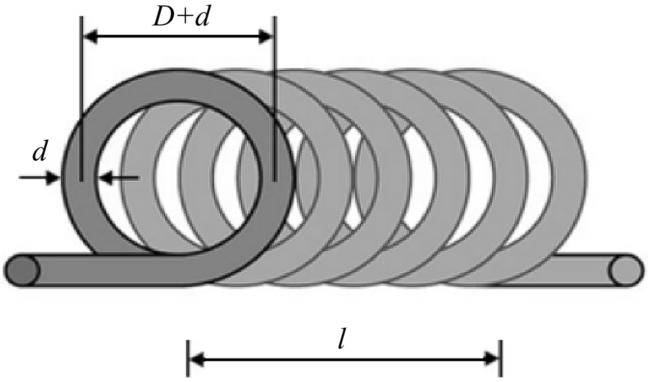

Figure 4.4: Geometry and dimensions of a single-layer air-core coil to show the parameters used in the inductance calculation [118].

Figure 4.5: The geometry and dimensions of the constructed solenoid coil: 72 mm inner diameter, 82 mm outer diameter, 70 mm coil length, 5 mm pure copper wire diameter, and 6.3 mm copper wire diameter (including insulation band between windings).

### 4.2.2 Inductance of the Multilayer Coil

Equation (4.2) calculates the inductance of air-core multilayer coil shown in Figure 4.6 for the given parameters [119]. The inductance of multilayer coil, $L_{coil}$ was computed as 119.9 µH.

$$L_{coil} = 31.6 \, \frac{N^2 \, R^2}{6R + 9l + 10c} \tag{4.2}$$

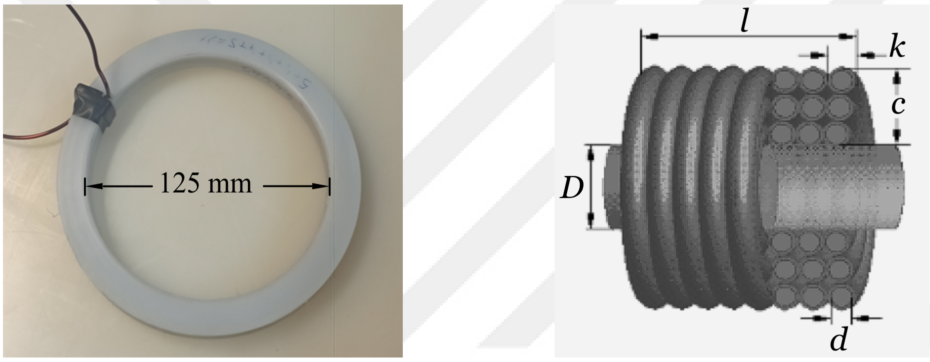

(a) (b)

Figure 4.6: (a) The multilayer coil utilized in the experimental study. (b) Geometry and dimensions of the multilayer air-core coil to demonstrate the parameters used in the inductance calculation [119].

The parameters of the multilayer coil used in the experimental setup are as follows:

$R$: mean radius of the winding, which is 6.75 cm.
$D$: inner radius of the winding, which is 6.25 cm.
$l$: the winding length, which is 1.1 cm.
$c$: the thickness of the winding, which is 1 cm.
$N$: number of turns, and 23.
$n$: the layer number, which is five.
$d$: the distance between consecutive layers, which is 2 mm.

### 4.3 Coil Resonance Circuit

Figure 4.7 demonstrates the series resonance circuit regulating the output current. This circuit was energized using a capacitor group that introduced resonance in the desired frequency. The resistance of the coil resonance circuit was acquired using Vishay VY1 AC ceramic disk capacitors.

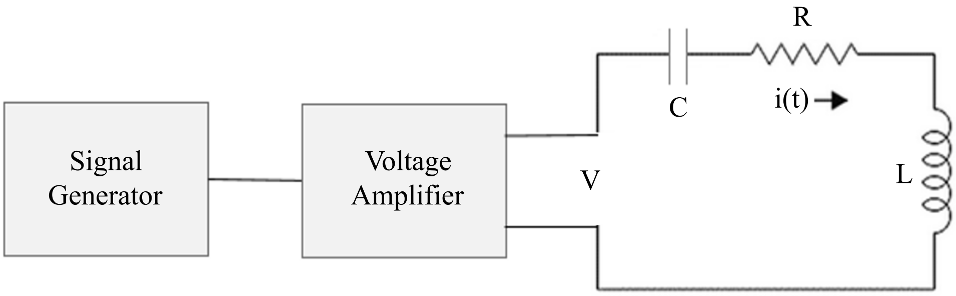

Figure 4.7: Diagram of the coil driving circuit employed in the experimental study.

$$Z_{coil} = R + jwL \tag{4.3}$$

$$f_{resonance} = \frac{1}{2\pi\sqrt{LC}} \tag{4.4}$$

$$C = \frac{1}{w^2 L} \tag{4.5}$$

The total resistance of the six parallel resistors shown in Figure 4.8 (each aluminum sink had three parallel resistors) was 0.15 Ω. The total resistance of the three parallel resistors used in the experiment was 0.35 Ω. The circuit's resonant frequency was determined by measuring the voltage in the resistor group at different frequencies, as listed in Table 4.2.

The simulation of the circuit using MATLAB Simulink is shown in Figure 4.9, with a 7.3 nF capacitor group and an inductance of 6.25 µH. The current and impedance graphs of the simulated circuit in the 550–950 kHz frequency band are shown in Figure 4.10.

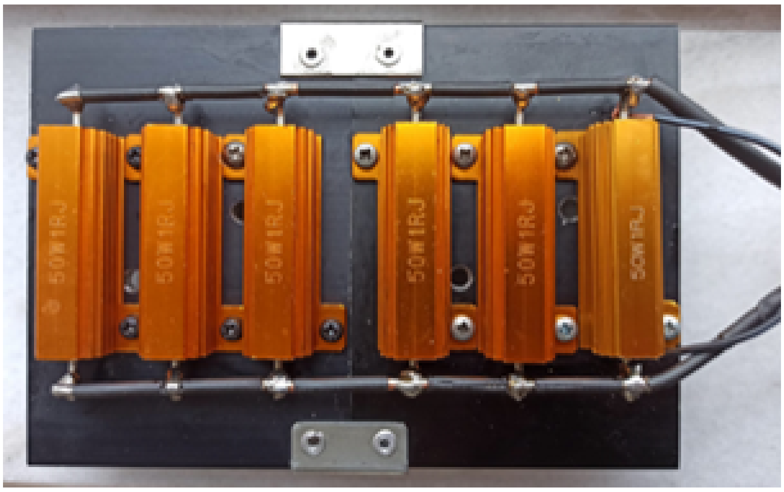

Figure 4.8: An assembly of 50 W 1Ω resistors was mounted on an aluminum heat sink. A resistor group was used to measure and control the output current of the voltage amplifier.

YÖK

Table 4.2: The voltages measured in the resistor group at different frequencies to determine the circuit resonant frequency.

| **Frequency** | **Voltage** |
|---|---|
| 690 kHz | 1.70 V |
| 700 kHz | 1.80 V |
| 710 kHz | 2.59 V |
| 720 kHz | 3.16 V |
| 730 kHz | 3.73 V |
| 740 kHz | 4.83 V |
| **745 kHz** | **6.85 V** |
| 750 kHz | 4.80 V |
| 760 kHz | 3.68 V |
| 770 kHz | 3.12 V |
| 780 kHz | 2.50 V |

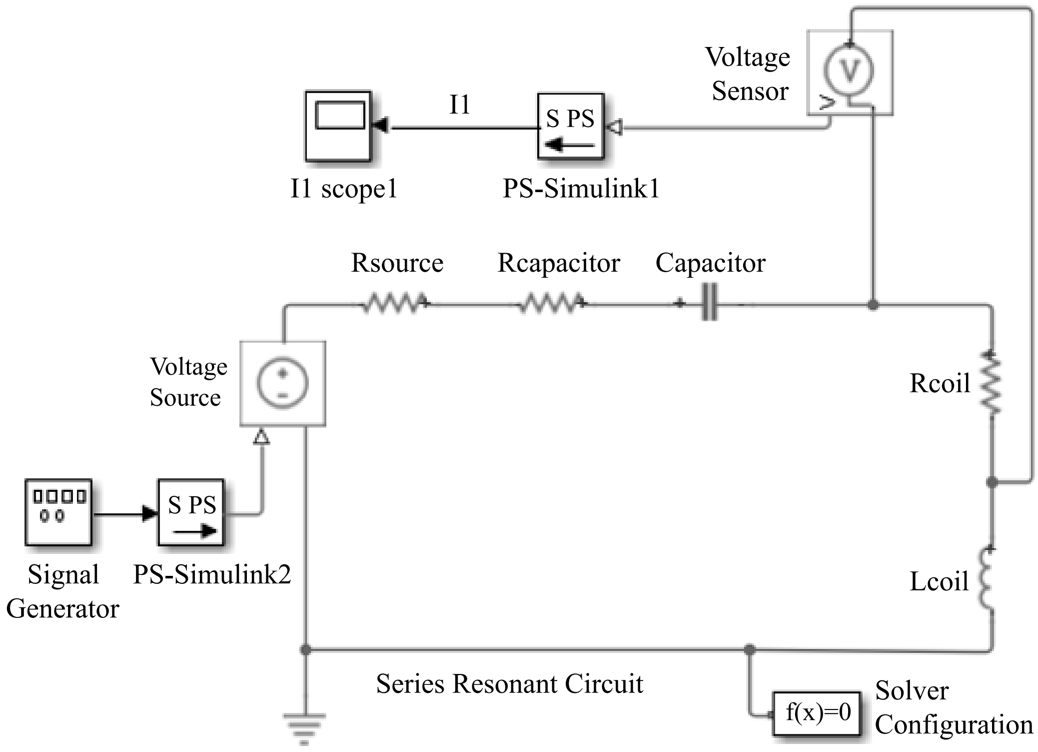

Figure 4.9: The coil driving circuit utilizes a 7.3 nF capacitor group and 6.25 µH coil inductance in the simulation. The serial resistance of the circuit was 0.35 Ω, and the simulation was operated at a frequency of 745 kHz [120].

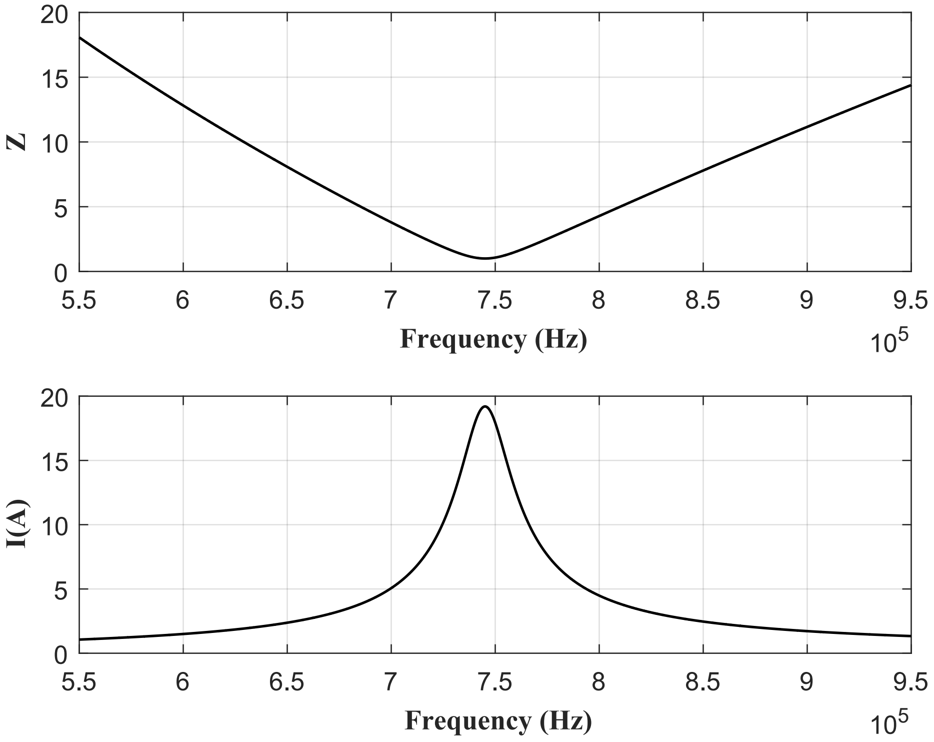

Figure 4.10: Impedance and current graphs of the resonance circuit simulated in the frequency range 550–950 kHz [120].

## 4.4 Tumorous Breast Phantom

This section describes the preparation of a material that mimics tumorous breast tissues. Vegetables can be used as phantoms owing to their suitable thermal and electrical properties [62, 121]. The specific heat of the vegetables depends on water ($c$ = 4180 $\mathrm{J/kg\ K}$) and other factors [122]. We created a healthy breast tissue phantom by using mashed potatoes. When raw potatoes are mashed, their high water content is reduced and they can be filled into containers. At $85\%$ water content, the specific heat of potatoes was 3600 $\mathrm{J/kg\ K}$, and at $60\%$ water content, the specific heat decreased to 3000 $\mathrm{J/kg\ K}$ [123]. 100 gram (g) mashed potato, 20 g oil ($c$ = 1670 $\mathrm{J/kg\ K}$), and saline (NaCl, Merck AG) were used to prepare a homogeneous breast phantom. Similarly, we produced a female breast tumor phantom using 10 g of gelatin (Bloom 200, Merck AG), 100 ml distilled water, red food coloring, and NaCl. The mixture was homogenized at 50 °C and stored at 8 °C [64].

The specific heat value of vegetables can be determined by employing the ingredient characteristics listed in Table 4.3 based on their content and temperature.

Table 4.3: Specific heat values of vegetable contents considering temperature, t (K) [122].

| **Material** | **Specific Heat (J/kg K)** |
|---|---|
| **Protein** | $2.01 + 1.21\ 10^{-3}\ t - 1.31\ 10^{-6}\ t^2$ |
| **Oil** | $1.98 + 1.47\ 10^{-3}\ t - 4.80\ 10^{-6}\ t^2$ |
| **Carbohydrate** | $1.55 + 1.96\ 10^{-3}\ t - 5.94\ 10^{-6}\ t^2$ |
| **Fiber** | $1.85 + 1.83\ 10^{-3}\ t - 4.65\ 10^{-6}\ t^2$ |
| **Water** | $4.13 - 9.09\ 10^{-3}\ t + 5.47\ 10^{-6}\ t^2$ |

Due to the experimental setup limitations and the desire to minimize the temperature increase in the coil winding, the conductivity of the healthy tissue phantom was increased to 3 $\mathrm{S/m}$. Similarly, the conductivity of the tumor was increased, and a tumorous breast phantom (3 $\mathrm{S/m}$ and 7.5 $\mathrm{S/m}$) was employed, as shown in Figures 4.11 and 4.12. The external heat source $q_{ext}$ and conductivity ratio of the healthy and tumorous tissues were kept constant while the applied current was decreased.

Table 4.4: Ingredients and conductivities of tumor and healthy tissue phantoms used in the experiments.

| **Ingredients** | **Healthy** | **Tumor** |
|---|---|---|
| Distilled water (ml) | – | 100 |
| Gelatine (g) | – | 10 |
| Mashed Potatoes (g) | 100 | – |
| Oil (g) | 20 | – |
| Conductivity (S/m) | 3 | 7.5 |

YÖK

(a) (b)

Figure 4.11: (a) A cubic container was filled with mashed potato, NaCl, and oil to simulate healthy tissues. (b) A phantom mimicking a tumor was prepared using a mixture of gelatin, distilled water, and food coloring agents placed inside a healthy tissue phantom.

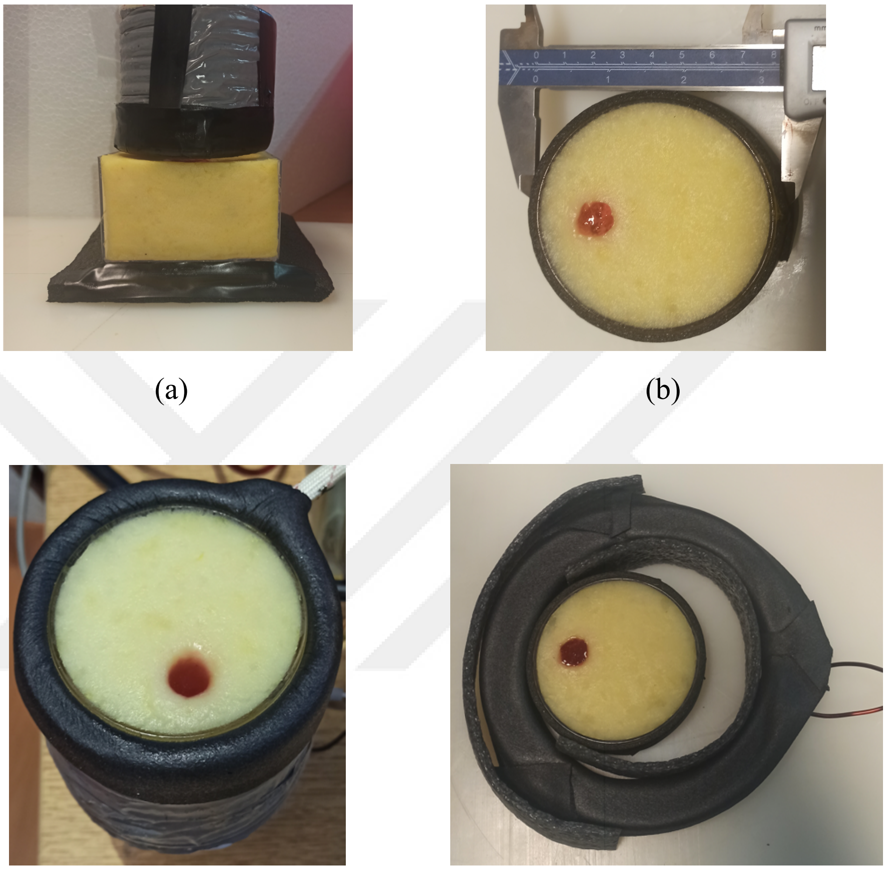

(a) (b)

(c) (d)

Figure 4.12: (a) Phantom and coil positioning of the experimental setup. (b) The tumorous phantom was positioned inside a petri dish. (c) The petri dish containing the tumorous phantom was placed inside the solenoid coil. (d) The experimental setup with a multilayer coil and a tumorous phantom.

## 4.5 Conductivity Measurement

The electrical conductivity was measured using two methods (a four-pin plunge probe circuit and cylindrical syringe), and the amount of NaCl (g) in the mixture (100 ml) was adjusted [124, 125]. A four-pin plunge probe circuit applies current to the outer electrodes (pin-1 and pin-4) [126]. The voltage amplifier card shown in Figure 4.13 measures the voltage ($V$) between the other two pins (pin-2 and pin-3) according to equation (4.6). The conductivity of the phantom was calculated using equation (4.7) [64, 127, 128].

$$V = \frac{I\,\rho}{2\pi\,\alpha} \tag{4.6}$$

$$\sigma = \frac{I\,\tau}{2\,V\,\pi\,\alpha} \tag{4.7}$$

Where $\alpha$ is the distance between the outer electrodes (15 mm), and $\tau$ is the correlation constant (2.9) obtained by comparing the measured conductivity with the conductivity of the reference mixture. The diameters of the electrodes were 0.39 mm. Their depths are 7 mm. The term ($I$) denotes the magnitude of the applied current (0.6 mA).

In the syringe conductivity measurement approach, the serial resistance of the phantom between the circular plates (aluminum) was obtained using an LCR meter, and the conductivity was calculated based on the cylinder syringe geometry shown in Figure 4.14.

The conductivity was determined through resistance measurements, considering the syringe geometry, and using equation (4.8). Where $L$ is the length of the cylinder, $A$ is the electrode surface area, and $R$ is the resistance measured with an LCR meter.

$$\sigma = \frac{L}{R\,A} \tag{4.8}$$

Figure 4.15 illustrates the relationship between the methods used to measure the conductivity. The results of the syringe method were validated against those of the plunge measurement method, which served as a reference.

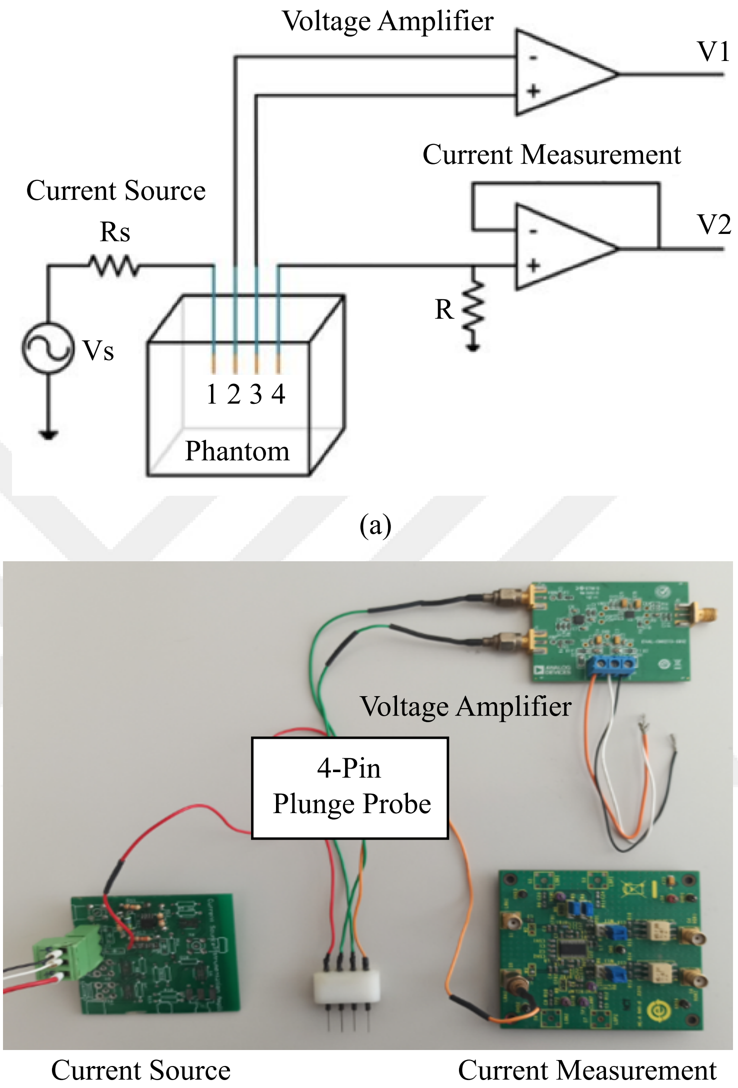

(a)

(b)

Figure 4.13: (a) Diagram illustrating four-pin conductivity measurement circuit. (b) The components of the conductivity measurement circuit consist of a constant current source circuit, four-pin plunge probe, voltage amplifier card that utilizes pin-2 and pin-3, and current measurement card that employs pin-1 and pin-4 [64].

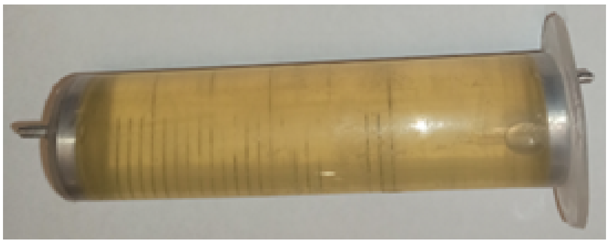

Figure 4.14: The conductivity measurements were performed using a cylindrical syringe. The resistance of the phantom was measured with the pins on the aluminum plates.

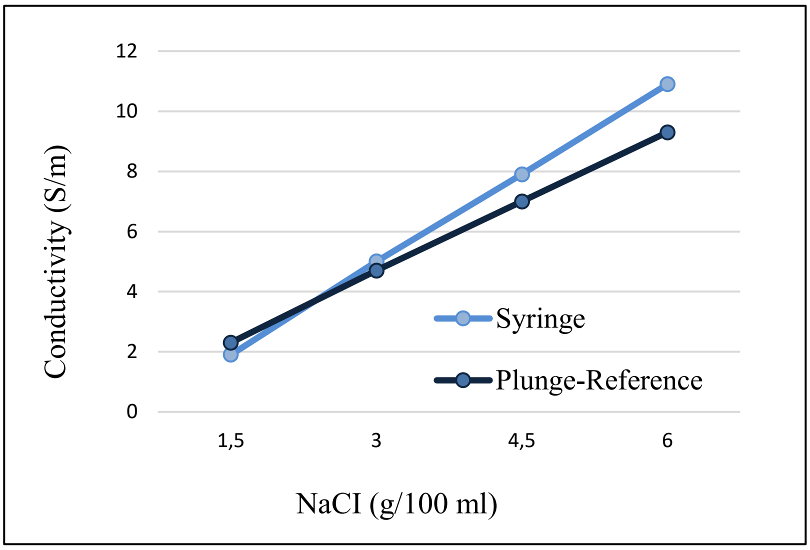

Figure 4.15: The conductivity values of the phantoms based on NaCl concentration (g/100 ml) were plotted using two different measurement methods.

### 4.6 Experimental Results

Three experimental studies were conducted to verify the proposed method. The experimental studies did not involve metabolic heat sources or blood perfusion rates, and only the effects of externally applied fields were observed at room temperature.

In the first experiment (Figure 4.1a), a solenoid coil geometry similar to that shown in Figure 3.1 was implemented. The results obtained using the IR camera are presented in Figure 4.16. We placed the phantom material in a 6.5 cm diameter and 1 cm depth glass petri dish inside the coil, as shown in Figure 4.16a. We used a rubber band around the coil to insulate the phantom from the coil temperature. The coil current was set to 15 A. Figures 4.16b and 4.16c show the temperature distributions of the tumor-free (homogeneous) and tumorous phantoms, respectively. The differences between the temperature distributions of the tumor-free and tumorous phantoms are shown in Figure 4.16d. We normalized the temperature scales and adjusted the temperature contrast of the difference data, revealing a tumorous region with a higher conductivity. A tumorous region with a higher conductivity became visible. The maximum temperature difference (decreased in the tumorous case) owing to the tumor was 0.4 °C.

Figure 4.1b illustrates the second experimental setup. In this experiment, the solenoid coil was positioned above the top surface of the cubic phantom, similar to the simulation setup shown in Figure 3.4a. The lower part of the coil was situated 2 mm above the cubic phantom. The tumorous phantom was housed inside an $8 \times 8 \times 5$ cm plastic container to form a cubic phantom geometry. The upper and imaging sides of the container were open, and the coil was placed on the upper side. A $1.5 \times 1 \times 1$ cm tumor was positioned 4 mm from the surface on the imaging axis, with the top surface of the tumor touching the top surface of the cubic phantom. In the active mode, a 20 A current (solenoid coil resonated at 745 kHz) was applied for 12 min before recording. The results are presented in Figure 4.17. The phantom was viewed from the open side, as shown in Figure 4.17a. To enhance resolution, we adjusted the temperature spectra of the thermal data using the FLIR Thermal Studio tool [129].

The surface-temperature distributions of the tumor-free and tumorous phantoms are

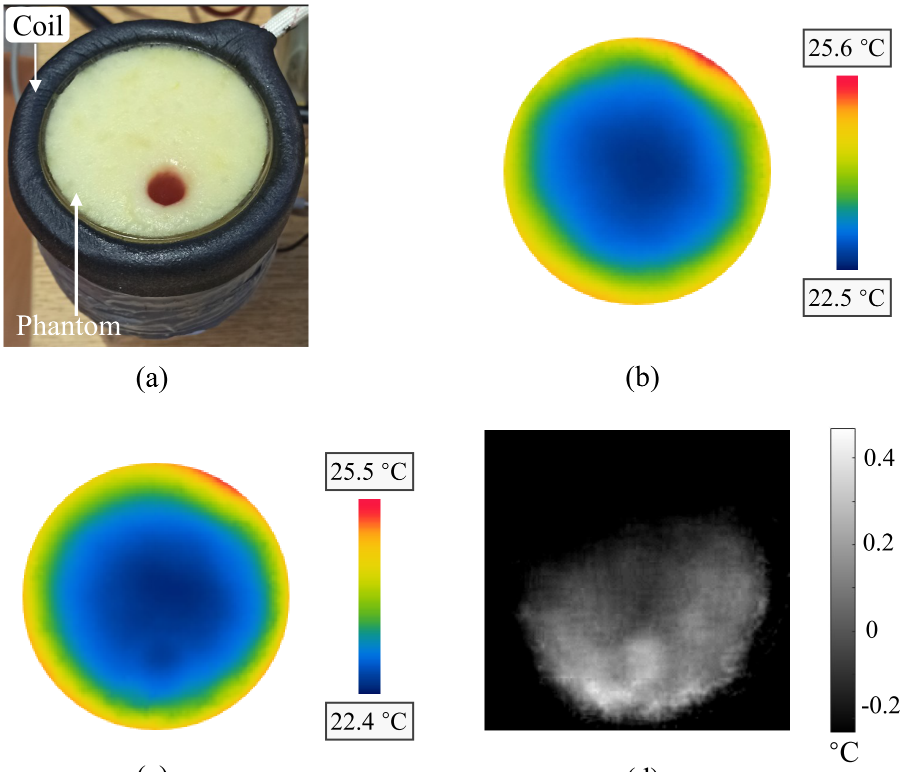

(a) (b)

(c) (d)

Figure 4.16: (a) The experiment was conducted using a circular phantom and solenoid coil. (b) Temperature distribution of the homogeneous (tumor-free) phantom. (c) Temperature distribution of the tumorous phantom. (d) Difference between the temperature distributions of tumorous and tumor-free phantoms.

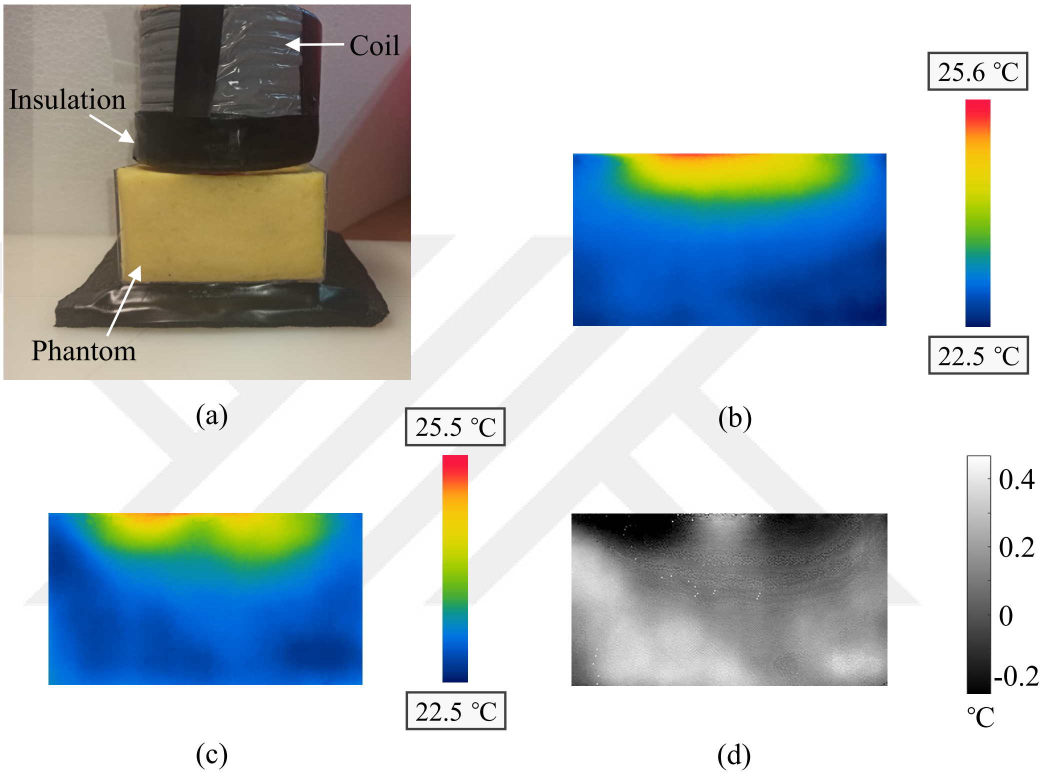

(a) (b) (c) (d)

Figure 4.17: (a) The experiment was conducted using a cubic phantom and solenoid coil. (b) Temperature distribution of the tumor-free phantom. (c) Temperature distribution of the tumorous phantom. (d) Difference between tumor and tumor-free phantom temperature distributions.

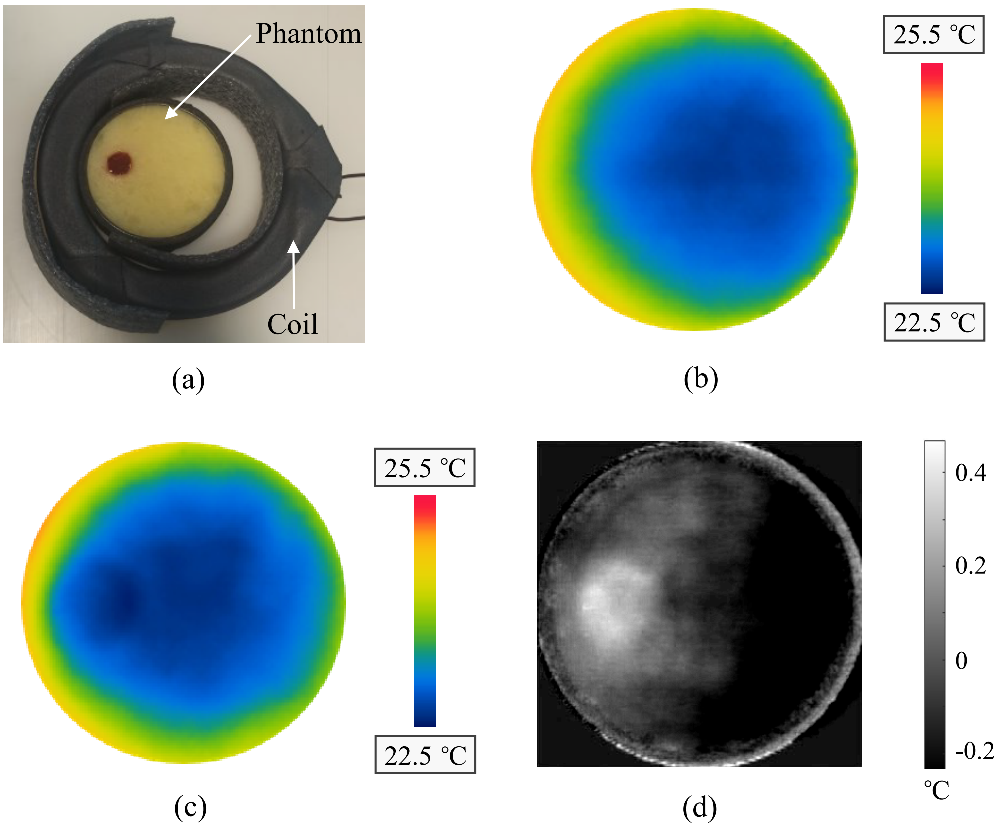

(a) (b)

(c) (d)

Figure 4.18: (a) The experiment utilized a circular phantom and a multilayer coil. (b) Temperature distribution of the tumor-free phantom. (c) Temperature distribution of the tumorous phantom. (d) The difference between the temperature distributions of the tumorous and tumor-free phantoms was determined.

shown in Figures 4.17b and 4.17c, respectively. Figure 4.17d displays the difference between the two images. A tumorous phantom became visible in Figure 4.17d owing to its higher electrical conductivity and specific heat. The maximum temperature difference at the tumor site is 0.4 °C.

In the third experiment, as illustrated in Figure 4.1c, the tumorous phantom was positioned in an 8 cm diameter and 1 cm depth petri dish. The container of the tumorous phantom was placed inside the multilayer coil as shown in Figure 4.18a. A 3.75 A current was applied (multilayer coil resonated at 755 kHz) for 12 min. Figures 4.18b and 4.18c show the surface temperature distributions of tumor-free and tumorous phantoms, respectively. The difference between the thermal data of the tumor-free and tumorous phantoms (the temperature contrast of the difference data was adjusted) is shown in Figure 4.18d. The tumor region became visible owing to the induced currents and specific heat of the tumor. The maximum temperature difference caused by the tumor was 0.4 °C.

### 4.6.1 Time-Dependent Variation in Surface Temperature

Figure 4.19 illustrates the time-dependent variations in the surface temperature of the cubic phantom demonstrated in Figure 4.17. The increasing temperature trend over time, with notably higher temperatures in the region near the coil, is shown in Figure 4.19.

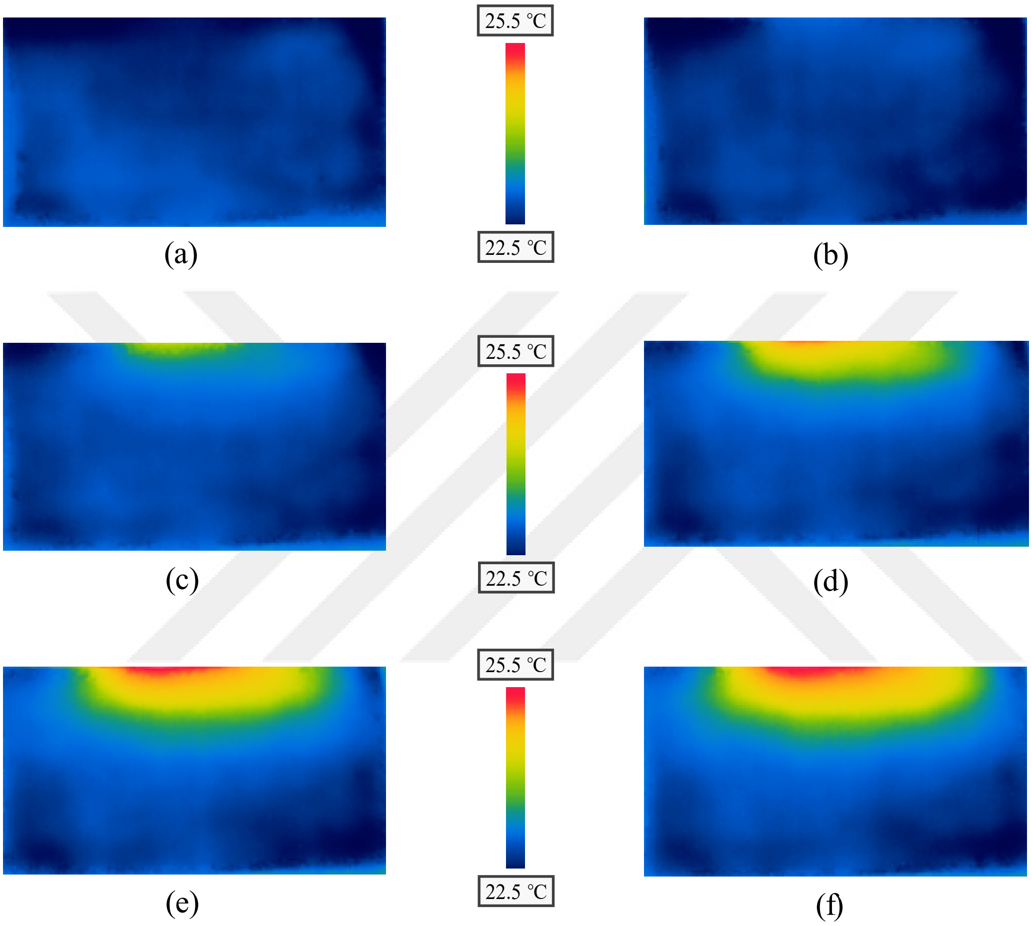

Figure 4.19: (a) Surface temperature of the cubic phantom at the initial time point of 0 min. (b)–(f) Surface temperature measurements of the cubic phantom at 3th, 6th, 9th, 12th, and 15th minutes are displayed, respectively.

## 4.7 Simulations of the Experimental Studies

The IC-ETI method with tumorous breast parameters, including metabolic heat and blood perfusion rates, was simulated using the numerical model discussed in Section 3.1. Simulations of in vitro experimental studies conducted at room temperature (22 °C) are expressed in this section. The purpose of these simulations was to compare experimental and numerical results.

The simulation results (surface temperature distributions) from the first experiment (Figure 4.1) for the tumor-free and tumorous cases are illustrated in Figures 4.20a and 4.20b, respectively. The differences between the two temperature distributions are shown in Figure 4.20c. Similar to the experimental results (Figure 4.16d), the tumorous region became distinguishable in active mode. The simulation results for the second experiment (Figure 4.17), that is, the temperature distributions formed for the tumor-free and tumorous cases, are shown in Figure 4.21a and 4.21b. The tumor was detected easily in the difference image (Figure 4.21c).

The simulation results of the third experiment (Figure 4.18) are shown in Figure 4.22. Figure 4.22a and 4.22b show the temperature distributions of the tumor-free and tumorous cases, respectively. The differences between the temperature distributions (Figure 4.22c) clearly reveal the existence of a tumor owing to its higher electrical conductivity and specific heat. We did not model a petri dish or container in the simulations. However, we used a glass petri dish for the first and third experiments. This difference resulted in slight temperature changes at the phantom boundary. The phantom container in the second experimental setup was open on both sides. Hence, the temperature distribution pattern of the second experiment was similar to that obtained from the simulations. The maximum temperature difference at the tumor location was between 0.35 °C and 0.4 °C in the simulations, and we obtained a temperature difference of 0.4 °C in the experimental studies.

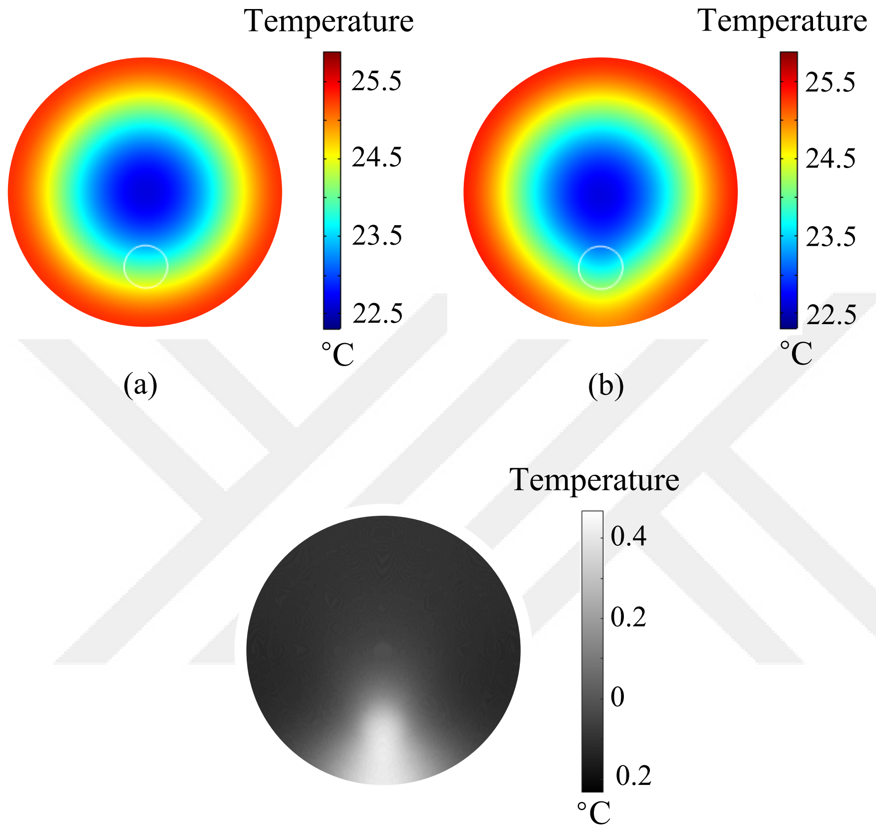

(a) (b)

(c)

Figure 4.20: Simulation results of the experimental studies. *First experiment:* (a) Temperature distribution of tumor-free phantom. (b) Temperature distribution of tumorous phantom. (c) Difference between temperature distributions of tumor-free and tumorous phantoms.

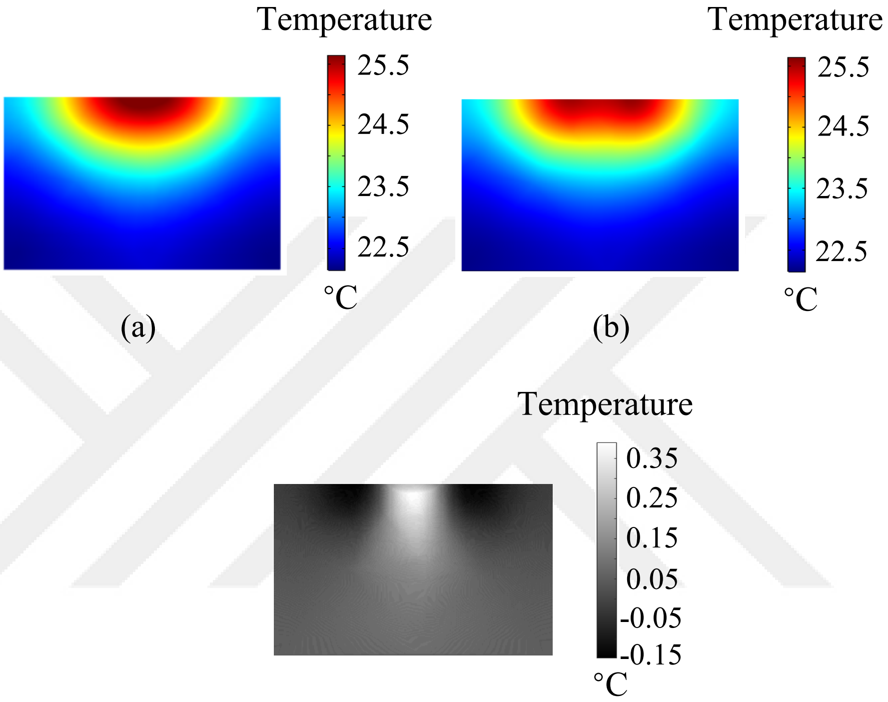

(a) (b)

(c)

Figure 4.21: Simulation results of the experimental studies. *Second experiment:* (a) Temperature distribution of the tumor-free phantom. (b) Temperature distribution of the tumorous phantom. (c) Difference between temperature distributions of tumor-free and tumorous phantoms.

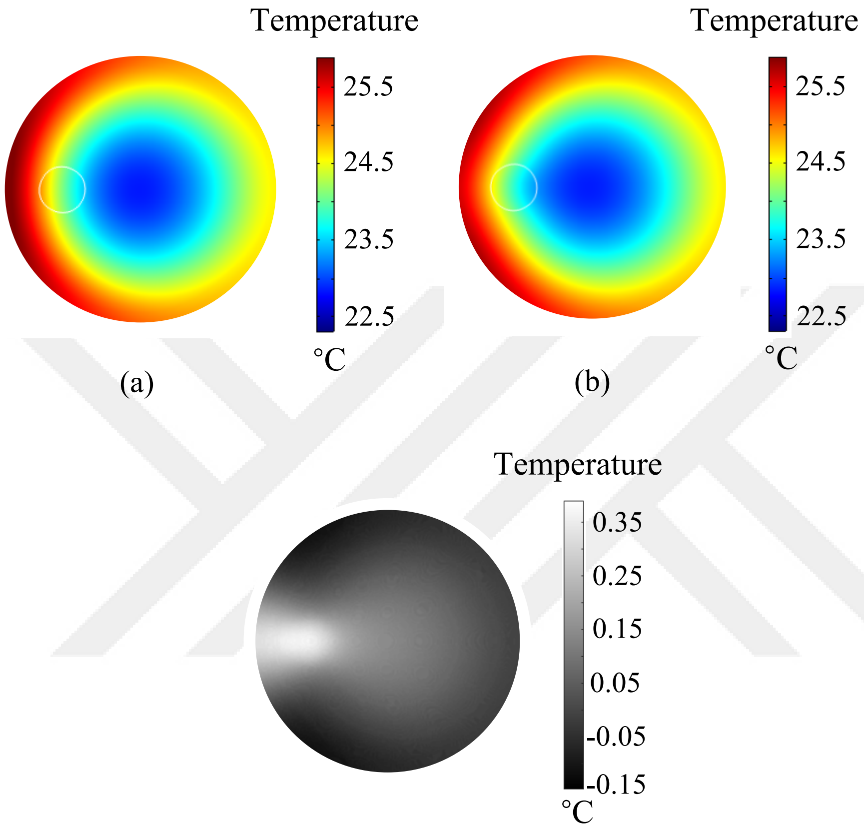

(a) (b) (c)

Figure 4.22: Simulation results of the experimental studies. *Third experiment:* (a) Temperature distribution of tumor-free phantom. (b) Temperature distribution of the tumorous phantom. (c) Difference between the tumor-free and tumorous phantom temperature distributions.

# CHAPTER 5

# CONCLUSION

The thesis study introduces a novel imaging method called IC-ETI. The theoretical basis of induced current electro-thermal imaging was introduced, and its fundamental characteristics were examined through simulations and experimental studies.

- This method predominantly uses the differences in the electrical and thermal properties of malignant breast tumors and the surrounding healthy tissues to improve the diagnostic performance of medical IR imaging. Electromagnetic and thermal problems of the method have been defined. Corresponding differential equations were resolved for the body tissues' electric field and temperature distribution.

- In the simulation study using a cubical body and a deep tumor, a 0.4 $^{\circ}$C temperature rise emerged at the center of the 1 cm$^3$ malignant tumor. When the tumorous tissue was at 10 mm depth, the temperature difference on the surface due to the tumor was 0.09 $^{\circ}$C in the passive mode. A temperature increase from metabolic heat sources was formed on the recording surface in the passive mode, and the tumor detection depth was 17 mm (with a 30 $^{\circ}\mathrm{mC}$ camera NETD).

- In the active simulation mode, an additional temperature difference occurred on the surface compared to the tumor-free case because of the induced current perturbation and specific heat difference on and around the tumor. A solenoid coil with a current of 60.5 A (according to a 10 $\mathrm{W/kg}$ SAR) was applied to induce currents inside the cubical body. The tumor was detected at a depth of 21 mm. The tumor detection depth increased by 4 mm.

- The theory of current density refraction and external heat source distribution was presented. Current density refraction and external heat source were simulated. The external heat sources generated inside the tumor were generally lower owing to the induced current perturbation than those in the homogeneous case. The strength of the heat sources increases outside the tumor region, where the induced current normally enters (or exits) the tumor region. However, tangential currents produce less heat outside the tumor boundary than in the inner region.

- The temperature increase in the tumor was lower because of the higher specific heat. In the active operation mode, the tumorous tissue became a region whose temperature increase was lower than that of the homogeneous case. This difference may help to detect deeper tumors and confirm the presence of tumors in the breast.

- In the experimental study, application-specific tumorous breast phantoms were produced using gelatin and mashed potatoes. The thermal and electrical properties of the phantoms were adjusted for the breast model. A 4-pin plunge probe and cylindrical tube were used to measure the conductivity of the phantoms. Serial resonant circuits were used to reduce the impedance and obtain the desired current from the voltage amplifier.

- The surface temperature distributions of homogeneous and inhomogeneous (tumorous) breast phantoms were analyzed using different body and coil configurations. An 11-turn, 70 mm long solenoid coil was constructed for the experimental studies, and a 20 A current was applied at 745 kHz. A temperature difference of up to 0.4 °C in the tumor location was observed compared to the absence of the tumor on the imaging surface. Similarly, a larger diameter 23-turn multilayer coil was utilized in serial resonance at 755 kHz with a 3.75 A current, and a 0.4 °C temperature difference at the tumor location was observed. The experimental studies were simulated, and the results were consistent.

## 5.1 Discussion

Medical IR imaging is a developing modality with several valuable diagnostic properties. However, the temperature contrast owing to deep and small tumors may be unnoticeable in the passive mode. Electro-thermal imaging is a hybrid IR imaging modality based on malignant tumors' high electrical conductivity and specific heat properties. It has been shown that the currents applied from surface electrodes may improve the temperature contrast [59]. However, performance depends on several parameters related to the electrodes (size, location, and number of electrodes) and excitation properties. Electro-thermal imaging may improve the diagnostic properties of IR imaging; however, using electrodes eliminates one crucial advantage of IR imaging, namely, contactless imaging. In this study, another active thermal imaging method based on the electrical conductivities of tissues was investigated while preserving the contactless imaging properties.

To investigate the basic properties of the method, we initially preferred a cylindrical phantom geometry encircled with a coil and displayed the current density and temperature distributions. Next, cubic body geometry was chosen to reveal the in-depth performance of the technique. In future numerical and experimental studies, application-specific coils and realistic body models can be used to investigate the technique's performance in more detail. The performance of the proposed method is affected by the relevant tissue parameters, metabolic heat source strength, tumor size, coil-body geometry, excitation type, excitation frequency and IR camera properties.

The current density in the phantom was proportional to the applied coil current and conductivity distribution. High-intensity currents should be utilized to perform an experimental study using realistic tissue conductivities (0.3 $\mathrm{S/m}$ for healthy tissues and 0.75 $\mathrm{S/m}$ for malignant tissues). In addition, capacitors should be compatible with high voltages at this current strength. In these primary experimental studies, however, we increased the tissue conductivity tenfold and decreased the coil current by one-third while keeping the induced power almost the same.

The operation mode is considered active as energy is introduced to the body during infrared (IR) recording. In this mode, changes in the surface temperature distribution owing to malignant tissues were barely noticeable. To increase the contrast due to the higher electrical conductivity of the malignant tissues, one may use either of the two reference images: 1) a passive mode image of the same body and 2) an active mode image of the same body without malignant tissue. The difference (or ratio) between the active-mode image and reference image may significantly enhance the contrast.

The metabolic heat sources were reduced when the passive-mode image was used as the reference image. At the same ambient temperature, the resultant distribution was primarily due to the external heat sources imposed by the induced currents. An earlier active-mode image of the same body without malignant tissue can eliminate the effects of high current densities near the coil while preserving the impact of metabolic heat sources in malignant tissues. However, recording such images under the same ambient temperature conditions is challenging. The differences between the two IR image records, owing to the body-coil alignment and camera view angles, may also cause undesired artifacts.

An alternative method is numerically forming an active mode reference image. The surface temperature distribution can be computed using a realistic model of a healthy body under the following conditions: 1) metabolic source distribution for healthy breast tissue, 2) the same coil configuration and excitation, and 3) the same ambient temperature. The advantages and disadvantages of a selected reference image should be explored separately, experimentally, and numerically.

The physics-informed neural network employing deep learning and physical principles to compute the temperature distribution within breast tissue may have several advantages. It may also detect abnormal regions and help differentiate deeper tumors [130]. Evaluating this method and similar artificial intelligence methods regarding active thermal imaging depth performance and reference image forming will be beneficial.

## 5.2 Future Work

The following improvements should be made in future studies:

- This research can serve as a preliminary theoretical basis for future practical investigations that employ the principles of active medical infrared imaging and the phenomenon of refraction in induced current for tissue heating. However, a more extensive theory on this subject should be investigated.
- An alternative reference method that uses artificial intelligence or numerically forms a reference image of a patient should be developed.
- Simultaneous reference images with IR imaging can be obtained by multi-frequency current applications on the tumorous breast using differentiation in the frequency-dependent dielectric parameters of tumors and breasts.
- Simulation studies using more realistic body geometries and further experimental studies will be beneficial to examine the method's practical use.
- Practical implementation of the method with real subjects is the ultimate goal of this study. However, a preliminary study using animal experiments in a temperature-controlled environment may provide practical information before developing a clinical prototype for real subjects.

YÖK

# REFERENCES

[1] E. K. Ng, “A review of thermography as promising non-invasive detection modality for breast tumor,” *International Journal of Thermal Sciences*, vol. 48, no. 5, pp. 849–859, 2009.

[2] D. A. Kennedy, T. Lee, and D. Seely, “A comparative review of thermography as a breast cancer screening technique,” *Integrative Cancer Therapies*, vol. 8, no. 1, pp. 9–16, 2009.

[3] H. Qi and N. A. Diakides, “Thermal infrared imaging in early breast cancer detection-a survey of recent research,” in *IEEE EMBS 25th Annual International Conference*, pp. 1109–1112, 2003.

[4] A. Chanmugam, R. Hatwar, and C. Herman, “Thermal analysis of cancerous breast model,” in *ASME International Mechanical Engineering Congress and Exposition*, pp. 134–143, 2012.

[5] “Realistic human female breast.” https://sketchfab.com/tags/breast. Last accessed date: 4 November 2023.

[6] “Human female breast anatomy.” https://sketchfab.com/3d-models/human-female-breast-anatomy-c429d0bd6e8b422bb1f355657278c159. Last accessed date: 4 November 2023.

[7] R. L. Siegel, K. D. Miller, N. S. Wagle, and A. Jemal, “Cancer statistics, 2023,” *Cancer Journal for Clinicians*, vol. 73, no. 1, pp. 17–48, 2023.

[8] W. H. Organization, “Breast cancer,” tech. rep., Genf, Schweiz, 2023.

[9] J. G. Elmore, K. Armstrong, C. D. Lehman, and S. W. Fletcher, “Screening for Breast Cancer,” *Journal of the American Medical Association*, vol. 293, pp. 1245–1256, 2005.

[10] W. E. Barlow, C. D. Lehman, Y. Zheng, B. B. Y. R Ballard-Barbash, and G. R. Cutter, “Performance of diagnostic mammography for women with signs or

symptoms of breast cancer," *Journal of the National Cancer Institute*, vol. 94, pp. 1151–1159, 2002.

[11] L. F. Smith, "Palpable cancer of the breast and negative mammography: The ongoing dilemma," *Journal of Surgical Oncology*, vol. 96, pp. 451–452, 2007.

[12] A. Sobti, P. Sobti, and L. G. Keith, "Screening and diagnostic mammograms: Why the gold standard does not shine more brightly," *International Journal of Fertility and Women's Medicine*, vol. 50, pp. 199–206, 2005.

[13] Y. Nagao, Y. Kawaguchi, Y. Sugiyama, S. Saji, and Y. Kashiki, "Relationship between mammographic density and the risk of breast cancer in japanese women: A case-control study," *Breast Cancer*, vol. 10, no. 3, pp. 228–233, 2003.

[14] E. Banks, "Hormone replacement therapy and the sensitivity and specificity of breast cancer screening: a review," *Journal of Medical Screening*, vol. 8.1, no. 1, pp. 29–34, 2001.

[15] T. M. Kolb, J. Lichy, and J. H. Newhouse, "Comparison of the performance of screening mammography, physical examination, and breast US and evaluation of factors that influence them: an analysis of 27,825 patient evaluations," *Radiology*, vol. 225, no. 1, pp. 165–175, 2002.

[16] C. K. Kuhl, S. Schrading, C. C. Leutner, N. Morakkabati-Spitz, E. Wardelmann, R. Fimmers, and H. H. Schild, "Mammography, breast ultrasound, and magnetic resonance imaging for surveillance of women at high familial risk for breast cancer," *Journal of Clinical Oncology*, vol. 23, no. 33, pp. 8469–8476, 2005.

[17] E. Warner, H. Messersmith, P. Causer, A. Eisen, R. Shumak, and D. Plewes, "Systematic review: using magnetic resonance imaging to screen women at high risk for breast cancer," *Annals of Internal Medicine*, vol. 148, no. 9, pp. 671–679, 2008.

[18] H. Moss, P. Britton, C. Flower, A. Freeman, D. Lomas, and R. Warren, "How reliable is modern breast imaging in differentiating benign from malignant

breast lesions in the symptomatic population," *Clinical Radiology*, vol. 54, no. 10, pp. 676–682, 1999.

[19] A. M. Hassan and M. El-Shenawee, "Review of electromagnetic techniques for breast cancer detection," *IEEE Reviews in Biomedical Engineering*, vol. 4, pp. 103–118, 2011.

[20] D. Saslow, C. Boetes, and et al, "American Cancer Society guidelines for breast screening with MRI as an adjunct to mammography.," *CA A Cancer Journal for Clinicians*, vol. 57, pp. 75–89, 2007.

[21] N. Aristokli, I. Polycarpou, S. Themistocleous, D. Sophocleous, and I. Mamais, "Comparison of the diagnostic performance of magnetic resonance imaging, ultrasound and mammography for detection of breast cancer based on tumor type, breast density and patient's history: A review," *Radiography*, vol. 28, no. 3, pp. 848–856, 2022.

[22] F. Benard and E. Turcotte, "Imaging breast cancer with single photon computed tomography and positron emission tomography," *Breast Cancer Research*, vol. 7, pp. 153–162, 2005.

[23] H. Schöder and M. Gönen, "Screening for Cancer with PET and PET/CT: Potential and Limitations," *Journal of Nuclear Medicine*, vol. 48, no. 1, pp. 4–18, 2007.

[24] A. Stojadinovic, A. Nissan, and et al., "Electrical Impedance Scanning for the Early Detection of Breast Cancer in Young Women: Preliminary Results of a Multicenter Prospective Clinical Trial," *Journal of Clinical Oncology*, vol. 23, no. 12, pp. 2703–2715, 2005.

[25] J. F. Head and R. L. Elliott, "Infrared imaging: making progress in fulfilling its medical promise," *IEEE Engineering in Medicine and Biology Magazine*, vol. 21, no. 6, pp. 80–85, 2002.

[26] J. D. Bronzino, *Biomedical Engineering Handbook: Medical Devices and Systems*. CRC Press, 2006.

[27] C. Meola and G. M. Carlomagno, “Recent advances in the use of infrared thermography,” *Measurement Science and Technology*, vol. 15, no. 9, p. 27, 2004.

[28] M. F. Modest and S. Mazumder, *Radiative Heat Transfer*. Academic Press: Elsevier, 2021.

[29] A. Plastropoulos, N. Adiuku, N. P. Avdelidis, C. Ibarra-Castanedo, X. P. Maldague, and P. Servais, “A short review on infrared thermography: history, philosophy, approaches, standards, and application examples,” *Thermosense: Thermal Infrared Applications*, vol. 12536, pp. 5–15, 2023.

[30] R. A. Thomas, *The Thermography Monitoring Handbook*. Coxmoor Publishing, 1999.

[31] M. E. Couture, “Challenges in infrared optics,” in *Infrared Technology and Applications*, vol. 4369, pp. 649–661, 2001.

[32] C. Besikci, “Nature allows high sensitivity thermal imaging with type-i quantum wells without optical couplers: a grating-free quantum well infrared photodetector with high conversion efficiency,” *IEEE Journal of Quantum Electronics*, vol. 57, no. 2, pp. 1–12, 2021.

[33] B. F. Jones, “A reappraisal of the use of infrared thermal image analysis in medicine,” *IEEE Transactions on Medical Imaging*, vol. 17, no. 6, pp. 1019–1027, 1998.

[34] R. Joro, A.-L. Lääperi, P. Dastidar, S. Soimakallio, T. Kuukasjärvi, T. Toivonen, R. Saaristo, and R. Järvenpää, “Imaging of breast cancer with mid-and long-wave infrared camera,” *Journal of Medical Engineering and Technology*, vol. 32, no. 3, pp. 189–197, 2008.

[35] J. F. Head, F. Wang, C. A. Lipari, and R. L. Elliott, “The important role of infrared imaging in breast cancer,” *IEEE Engineering in Medicine and Biology*, vol. 19, no. 3, pp. 52–57, 2000.

[36] R. Lawson, “Implications of Surface Temperatures in the Diagnosis of Breast Cancer,” *Canadian Medical Association Journal*, vol. 75, pp. 309–310, 1956.

[37] K. Williams, F. Williams, and R. Handley, “Infrared thermometry in the diagnosis of breast disease,” *Lancet*, vol. 2, pp. 1378–1381, 1961.

[38] M. Gautherie and C. Gros, “Breast thermography and cancer risk prediction,” *Cancer*, vol. 45, pp. 51–56, 1980.

[39] M. Gautherie, P. Haehnel, J. P. Walter, and L. Keith, “Long-term assessment of breast cancer risk by liquid-crystal thermal imaging,” *Progress in Clinical and Biological Research*, pp. 279–301, 1982.

[40] J. Keyserlingk, P. Ahlgren, E. Yu, and N. Belliveau, “Infrared Imaging of the Breast: Initial Reappraisal Using High-Resolution Digital Technology in 100 Successive Cases of State I and II Breast Cancer,” *The Breast Journal*, vol. 4, no. 4, pp. 254–251, 1998.

[41] M. A. Fauci, R. Breiter, W. Cabanski, W. Fick, R. Koch, J. Ziegler, and S. D. Gunapala, “Medical infrared imaging – differentiating facts from fiction, and the impact of high precision quantum well infrared photodetector camera systems, and other factors in its reemergence,” *Infrared Physics and Technology*, vol. 42, no. 3-5, pp. 337–344, 2001.

[42] M. Anbar, “Hyperthermia of the cancerous breast: analysis of mechanism,” *Cancer Letter*, vol. 84, no. 1, pp. 23–29, 1994.

[43] N. Weidner, S. O. Semple, W. R. Welch, and J. Folkman, “Tumor angiogenesis and metastasis: correlation in invasive breast carcinoma,” *New England Journal of Medicine*, vol. 324, pp. 1–8, 1991.

[44] E. Y. K. Ng, S. C. Fok, Y. C. Peh, F. C. Ng, and L. S. J. Sim, “Computerized detection of breast cancer with artificial intelligence and thermograms,” *Journal of Medical Engineering and Technology*, vol. 26, no. 4, pp. 152–157, 2002.

[45] H. Qi and J. F. Head, “Asymmetry analysis using automatic segmentation and classification for breast cancer detection in thermograms,” in *EMBS Proceedings of the 23rd Annual International Conference of the IEEE*, vol. 3, pp. 2866–2869, 2001.

[46] G. Jacob, I. Jose, and S. Sujatha, “Breast cancer detection: A comparative review on passive and active thermography,” *Infrared Physics and Technology*, p. 104932, 2023.

[47] M. Salhab, L. G. Keith, M. Laguens, W. Reeves, and K. Mokbel, “The potential role of dynamic thermal analysis in breast cancer detection,” *International Seminars in Surgical Oncology*, vol. 3, no. 8, pp. 3–8, 2006.

[48] T. M. Button, H. F. Li, and et al., “Dynamic infrared imaging for the detection of maligancy,” *Physics in Medicine and Biology*, vol. 49, pp. 3105–3116, 2004.

[49] Y. Ohashi and I. Uchida, “Applying dynamic thermography in the diagnosis of breast cancer,” *IEEE Engineering in Medicine and Biology Magazine*, vol. 19, no. 3, pp. 42–51, 2000.

[50] M. Anbar, “Modalities and clinical applications of dynamic infrared imaging,” in *EMBS, Proceedings of the 23rd Annual International Conference of the IEEE*, vol. 3, pp. 2820–2822, 2001.

[51] A. W. Guy, “Analysis of electromagnetic fields induced in biological tissues by thermographic studies on equivalent phantom models,” *IEEE Transactions on Microwave Theory and Techniques*, vol. 19, no. 2, pp. 205–214, 1971.

[52] M. Kaczmarek and A. Nowakowski, “Analysis of transient thermal processes for improved visualization of breast cancer using IR imaging,” in *25th Annual International Conference of the IEEE Engineering in Medicine and Biology Society*, pp. 1113–1116, 2003.

[53] M. Kaczmarek and A. Nowakowski, “Active IR-thermal imaging in medicine,” *Journal of Nondestructive Evaluation*, vol. 35, no. 1, pp. 1–16, 2016.

[54] R. Tipa and O. Baltag, “Microwave thermography for cancer detection,” *Romanian Journal of Physics*, vol. 51, no. 3-4, p. 371, 2006.

[55] S. Rahmatinia and B. Fahimi, “Magneto-thermal modeling of biological tissues: a step toward breast cancer detection,” *IEEE Transactions on Magnetics*, vol. 53, no. 6, pp. 1–4, 2017.

[56] B. Jessie, J. Liang, Y. Li, B. Fahimi, *et al.*, “High-frequency excitation and surface temperature analysis of breast tissue for detection of anomaly,” *BioMed Research International*, 2023.

[57] B. Guo, J. Li, H. Zmuda, and M. Sheplak, “Multifrequency microwave-induced thermal acoustic imaging for breast cancer detection,” *IEEE Transactions on Biomedical Engineering*, vol. 54, no. 11, pp. 2000–2010, 2007.

[58] Y. H. El-Sharkawy and A. F. El-Sherif, “High-performance near-infrared imaging for breast cancer detection,” *Journal of Biomedical Optics*, vol. 19, no. 1, pp. 16–18, 2014.

[59] H. F. Carlak, N. G. Gencer, and C. Besikci, “Theoretical assessment of electro-thermal imaging: A new technique for medical diagnosis,” *Infrared Physics and Technology*, vol. 76, pp. 227–234, 2016.

[60] N. G. Gencer, H. F. Carlak, and C. Besikci, *Method and System for Dual-Band Active Thermal Imaging using Multi-Frequency Currents*. Number: WO2015002618A1, 2015.

[61] H. F. Carlak, *Medical electro-thermal imaging*. PhD thesis, Middle East Technical University, 2012.

[62] G. Ozdemir, “Investigating the multi-frequency performance of electro-thermal imaging: An experimental study,” Master’s thesis, Middle East Technical University, 2013.

[63] V. Tanrıverdi and N. G. Gençer, “Induced current thermal imaging in breast cancer detection,” in *Signal Processing and Communication Applications Conference*, pp. 1–4, 2021.

[64] V. Tanrıverdi and N. G. Gençer, “Phantom and solenoid coil development for induced current electro-thermal imaging,” in *IEEE Tıptekno Medical Technologies Congress*, pp. 1–4, 2021.

[65] X. Maldague, *Theory and Practice of Infrared Technology for Nondestructive Testing*. Newyork: Wiley, 2001.

[66] J. Vrana and M. Goldammer, “Induction and conduction thermography: from the basics to application,” in *Thermografie-Anwenderkonferenz*, 2017.

[67] U. Netzelmann, G. Walle, S. Lugin, A. Ehlen, S. Bessert, and B. Valeske, “Induction thermography: Principle, applications and first steps towards standardisation,” *Quantum Information Theory*, vol. 13, no. 2, pp. 170–181, 2016.

[68] J. Wilson, G. Y. Tian, I. Z. Abidin, S. Yang, and D. Almond, “Modelling and evaluation of eddy current stimulated thermography,” *Nondestructive Testing and Evaluation*, vol. 25, no. 3, pp. 205–218, 2010.

[69] M. Peiravi, H. Eslami, M. Ansari, and H. Zare-Zardini, “Magnetic hyperthermia: Potentials and limitations,” *Journal of the Indian Chemical Society*, vol. 99, no. 1, p. 100269, 2022.

[70] H. Fricke and S. Morse, “The electric capacity of tumors of the breast,” *The Journal of Cancer Research*, vol. 10, no. 3, pp. 340–376, 1926.

[71] K. S. Cole and R. H. Cole, “Dispersion and absorption in dielectrics i. alternating current characteristics,” *The Journal of Chemical Physics*, vol. 9, no. 4, pp. 341–351, 1941.

[72] H. P. Schwan and C. F. Kay, “Capacitive properties of body tissues,” *Circulation Research*, vol. 5, no. 4, pp. 439–443, 1957.

[73] A. J. Surowiec, S. S. Stuchly, J. R. Barr, and A. A. S. A. Swarup, “Dielectric properties of breast carcinoma and the surrounding tissues,” *IEEE Transactions on Biomedical Engineering*, vol. 35, no. 4, pp. 257–263, 1988.

[74] S. Chaudhary, R. Mishra, A. Swarup, and J. M. Thomas, “Dielectric properties of normal & malignant human breast tissues at radiowave & microwave frequencies,” *Indian Journal of Biochemistry and Biophysics*, vol. 21, no. 1, pp. 76–79, 1984.

[75] C. Gabriel, S. Gabriel, and E. Corthout, “The dielectric properties of biological tissues: I. Literature survey,” *Physics in Medicine and Biology*, vol. 41, no. 11, pp. 2231–2249, 1996.

[76] D. Andreuccetti and C. Petrucci, “An Internet resource for the calculation of the dielectric properties of body tissues in the frequency range 10 Hz-100 GHz.” http://niremf.ifac.cnr.it/tissprop/. Last accessed date: 4 November 2023.

[77] C. Gabriel, *Compilation of the Dielectric Properties of Body Tissues at RF and Microwave Frequencies*. Texas, USA: Brooks Air Force Base, 1996.

[78] G. Ma and M. Soleimani, “Spectral capacitively coupled electrical resistivity tomography for breast cancer detection,” *IEEE Access*, vol. 8, pp. 50900–50910, 2020.

[79] S. Gabriel, R. W. Lau, and C. Gabriel, “The dielectric properties of biological tissues: II. Measurements in the frequency range 10 Hz to 20 GHz,” *Physics in Medicine and Biology*, vol. 41, no. 11, pp. 2251–2269, 1996.

[80] S. Gabriel, R. W. Lau, and C. Gabriel, “The dielectric properties of biological tissues: III. Parametric models for the dielectric spectrum of tissues,” *Physics in Medicine and Biology*, vol. 41, no. 11, pp. 2271–2293, 1996.

[81] M. Paruch, “Mathematical modeling of breast tumor destruction using fast heating during radiofrequency ablation,” *Materials*, vol. 13, no. 1, p. 136, 2019.

[82] ICNIRP, “International commission on non-ionizing radiation protection guidelines for limiting exposure to time-varying electric, magnetic, and electromagnetic fields (up to 300 gigahertz),” *Health physics*, vol. 74, no. 4, pp. 494–522, 1998.

[83] H. Griffiths, W. R. Stewart, and W. Gough, “Magnetic induction tomography. A measuring system for biological tissues,” *Annals of the New York Academy of Sciences*, vol. 873, no. 1, pp. 335–345, 1999.

[84] L. Ma and M. Soleimani, “Magnetic induction tomography methods and applications: A review,” *Measurement Science and Technology*, vol. 28, no. 7, p. 072001, 2017.

[85] K. R. Demarest, *Engineering Electromagnetics*. New Jersey: Prentice Hall, 1998.

[86] D. K. Cheng, *Fundamentals of Engineering Electromagnetics*. MA: Addison-Wesley, 1994.

[87] R. M. Gulrajani, *Bioelectricity and Biomagnetism*. Newyork: J. Wiley, 1998.

[88] D. M. Pozar, *Microwave Engineering*. Newyork: J. Wiley, 2011.

[89] Z. Xu, Q. Li, and W. He, "Analytical solution for the forward problem of magnetic induction tomography with multi-layer sphere model," *Life System Modeling and Intelligent Computing*, pp. 42–50, 2010.

[90] W. C. Chew, "Vector potential electromagnetics with generalized gauge for inhomogeneous media: Formulation," *Progress in Electromagnetics Research*, vol. 149, pp. 69–84, 2014.

[91] E. H. Wissler, "Pennes' 1948 paper revisited," *Journal of Applied Physiology*, vol. 85, no. 1, pp. 35–41, 1998.

[92] A. Singhvi, K. C. Boyle, M. Fallahpour, B. T. Khuri-Yakub, and A. Arbabian, "A microwave-induced thermoacoustic imaging system with non-contact ultrasound detection," *IEEE Transactions on Ultrasonics Ferroelectrics and Frequency Control*, vol. 66, no. 10, pp. 1587–1599, 2019.

[93] T. M. Fiedler, M. E. Ladd, and A. K. Bitz, "SAR simulations and safety," *Neuroimage*, vol. 168, pp. 33–58, 2018.

[94] K. Budnik and W. Machczynski, "Analytical magnetic field calculation of helical current conductors," *Elektryka*, vol. 4, pp. 17–28, 2010.

[95] G. Temple, "Static and dynamic electricity," *Nature*, vol. 146, no. 3701, p. 446, 1940.

[96] "Infrared-spectrum." https://www.infratec.eu/sensor-division/servicesupport/glossary/infrared-radiation/. Last accessed date: 4 November 2023.

[97] F. J. Sanchez-Marin, S. Calixto-Carrera, and C. Villaseñor-Mora, "Novel approach to assess the emissivity of the human skin," *Journal of Biomedical Optics*, vol. 14, no. 2, pp. 024006–024006, 2009.

[98] J. Steketee, “Spectral emissivity of skin and pericardium,” *Physics in Medicine and Biology*, vol. 18, no. 5, p. 686, 1973.

[99] J. Huh and et al, “Detectability of Delamination in Concrete Structure Using Active Infrared Thermography in Terms of Signal-to-Noise Ratio,” *Applied Sciences*, vol. 8, no. 10, 2018.

[100] “Collected Power by an IR Camera.” http://acl.digimat.in/nptel/courses/video/112107256/lec40.pdf. Last accessed date: 4 November 2023.

[101] A. Amri, S. H. Pulko, and A. J. Wilkinson, “Potentialities of steady-state and transient thermography in breast tumour depth detection: A numerical study,” *Computer Methods and Programs in Biomedicine*, vol. 123, pp. 68–80, 2016.

[102] F. P. Incropera, D. P. DeWitt, T. L. Bergman, and A. S. Lavine, *Fundamentals of Heat and Mass Transfer*. New York: Wiley, 2007.

[103] A. V. Vorst, A. Rosen, and Y. Kotsuka, *RF/Microwave Interaction with Biological Tissues*. NJ, USA: Wiley, 1 ed., 2006.

[104] Q. A. Pankhurst, J. Connolly, S. K. Jones, and J. Dobson, “Applications of magnetic nanoparticles in biomedicine,” *Journal of Physics D: Applied Physics*, vol. 36, no. 13, p. 167, 2003.

[105] COMSOL, *Comsol multiphysics reference manual v5.3*. Burlington, COMSOL Inc., 2017.

[106] F. J. González, “Thermal simulation of breast tumors,” *Revista Mexicana de Fisica*, vol. 53, no. 4, pp. 323–326, 2007.

[107] T. J. C. Faes, H. A. V. D. Meij, J. C. Munck, and R. M. Heethaar, “The electric resistivity of human tissues (100 Hz-10 MHz): a meta-analysis of review studies,” *Physiological Measurement*, vol. 20, no. 4, pp. 1–10, 1999.

[108] P. A. Hasgall, F. D. Gennaro, C. Baumgartner, E. Neufeld, B. Lloyd, M. C. Gosselin, D. Payne, A. Klingenböck, and N. Kuster, “IT’IS Database for thermal and electromagnetic parameters of biological tissues, version 4.1.” Last accessed date: 4 November 2023.

[109] J. S. Camillari, L. Farrugia, and et al, “Review of Thermal and Physiological Properties of Human Breast Tissue,” *Sensors*, vol. 22, no. 10, p. 3894, 2022.

[110] IEC, *Medical electrical equipment part: Particular requirements for the basic safety and essential performance*. IEC 60601-2-33, 2015.

[111] E. G. M. et al., “Radiological audit of interval breast cancers: Estimation of tumour growth rates.,” *The Breast*, vol. 51, pp. 114–119, 2020.

[112] E. Y. K. Ng and N. M. Sudharsan, “An improved three-dimensional direct numerical modelling and thermal analysis of a female breast with tumour,” in *Proceedings of the Institution of Mechanical Engineers, Part H: Journal of Engineering in Medicine*, vol. 215, pp. 25–37, 2001.

[113] J. B. Mercer and L. D. Weerd, “Thermography and thermal symmetry,” in *IEEE International Symposium on Medical Measurements and Applications*, pp. 1–3, 2014.

[114] S. Hossain and F. Mohammadi, “Numerical simulation and thermal analysis of tumor in the human body,” in *Proceedings of the 2016 COMSOL Conference in Boston*, 2016.

[115] FLIR, *FLIR T420 user manuel*. Wilsonville, FLIR Sys. Inc., 2014.

[116] Amp-Line, *ALC AL-1400-HF-A High frequency power amplifier user manuel*. Newyork, Amp-Line Corp., 2022.

[117] “Single Layer Coil Inductance.” http://electronbunker.ca/eb/ CalcMethods3b.html. Last accessed date: 4 November 2023.

[118] “Inductance of a Solenoid.” https://images.app.goo.gl/ZfVPqggn4gdsfT1H9.

[119] “Coil 32 Multilayer Coil Inductance.” https://coil32.net/multi-layer-coil.html. Last accessed date: 4 November 2023.

[120] MATLAB, *Version (R2016b)*. Massachusetts, The MathWorks Inc., 2016.

[121] E. G. Murakami, “The thermal properties of potatoes and carrots as affected by thermal processing 1,” *Journal of Food Process Engineering*, vol. 20, no. 5, pp. 415–432, 1997.

[122] ASHRAE, *Handbook-Refrigeration: Thermal Properties of Foods*. Atlanta: American Society of Heating Refrigerating and Air-Conditioning Engineers, 2006.

[123] I. Lamberg and B. Hallström, “Thermal properties of potatoes and a computer simulation model of a blanching process,” *International Journal of Food Science and Technology*, vol. 21, no. 5, pp. 577–585, 1986.

[124] C. Gabriel, A. Peyman, and E. H. Grant, “Electrical conductivity of tissue at frequencies below 1 MHz,” *Physics in Medicine and Biology*, vol. 54, no. 16, p. 4863, 2009.

[125] D. Bennett, “NaCl doping and the conductivity of agar phantoms,” *Materials Science and Engineering: C* , vol. 31, no. 2, pp. 494–498, 2011.

[126] D. Haemmerich, S. T. Staelin, J. Z. Tsai, S. Tungjitkusolmun, D. M. Mahvi, and J. G. Webster, “In vivo electrical conductivity of hepatic tumours,” *Physiological Measurement*, vol. 24, no. 2, p. 251, 2003.

[127] P. Steendijk, G. Mur, E. T. V. D. Velde, and J. Baan, “The four-electrode resistivity technique in anisotropic media: theoretical analysis and application on myocardial tissue in vivo,” *IEEE Transactions on Biomedical Engineering*, vol. 40, no. 11, pp. 1138–1148, 1993.

[128] J. Z. Tsai, H. Cao, S. Tungjitkusolmun, E. J. Woo, V. R. Vorperian, and J. G. Webster, “Dependence of apparent resistance of four-electrode probes on insertion depth,” *IEEE Transactions on Biomedical Engineering*, vol. 47, no. 1, pp. 41–48, 2000.

[129] FLIR, *FLIR thermal studio user manuel*. Wilsonville, FLIR Sys. Inc., 2021.

[130] O. Mukhmetov, Y. Zhao, A. Mashekova, V. Zarikas, E. Y. K. Ng, and N. Aidossov, “Physics-informed neural network for fast prediction of temperature distributions in cancerous breasts as a potential efficient portable artificial intelligence-based diagnostic tool,” *Computer Methods and Programs in Biomedicine*, vol. 242, p. 107834, 2023.

[131] V. Rudnev, D. Loveless, and R. L. Cook, *Handbook of Induction Heating*. CRC Press, 2017.

[132] S. Hossain and F. A. Mohammadi, "Development of an estimation method for interior temperature distribution in live biological tissues of different organs," *International Journal of Engineering*, vol. 3, no. 2, p. 8269, 2013.

[133] A. Constantin and R. Johnson, "Large gyres as a shallow-water asymptotic solution of euler's equation in spherical coordinates," *Proceedings of the Royal Society A: Mathematical, Physical and Engineering Sciences*, vol. 473, no. 2200, p. 20170063, 2017.

# APPENDICES

## A. Electromagnetic Field Equations and Assumptions

The derivation of the electromagnetic field equations and the $\boldsymbol{A} - \phi$ formulation, the flux density of the N-turn circular loop, and the electromagnetic assumptions at 750 kHz are presented in this section.

### A.1 Derivation of Electromagnetic Field Equations

The solution of magnetically induced current in low-conductivity, inhomogeneous linear media, such as biological tissue, can be obtained by solving the partial differential equations (A.7) and (A.14). The first equation is determined by using Maxwell's equations, which are derived from the fundamental electromagnetic field and constitutive equations given below:

$$\boldsymbol{B} = \nabla \times \boldsymbol{A} \tag{A.1}$$

$$\boldsymbol{B} = \mu \boldsymbol{H} \tag{A.2}$$

$$\boldsymbol{H} = \frac{1}{\mu} \nabla \times \boldsymbol{A} \tag{A.3}$$

$$\nabla \times \boldsymbol{E} = -jw\mu \boldsymbol{H} \tag{A.4}$$

$$\nabla \times \boldsymbol{H} = (\sigma + jw\epsilon)\, \boldsymbol{E} + \boldsymbol{J}_s \tag{A.5}$$

$$\sigma \frac{d\boldsymbol{A}}{dt} + \nabla \times (\mu^{-1} \nabla \times \boldsymbol{A}) + \sigma \nabla \phi = \boldsymbol{J}_s + \epsilon \frac{d^2\boldsymbol{A}}{dt^2} \tag{A.6}$$

In phasor notation, by employing the Coulomb gauge ($\nabla.\boldsymbol{A} = 0$), the first expression becomes [61, 85, 87]:

$$\nabla^2 \boldsymbol{A} - jw\mu\, (\sigma + jw\epsilon)\, \boldsymbol{A} - \mu\, (\sigma + jw\epsilon)\, \nabla\phi = -\mu \boldsymbol{J}_s \tag{A.7}$$

The following steps are employed to derive the second expression.

$$\nabla.\, \boldsymbol{D} = q \tag{A.8}$$

where $q$ is the volume charge density and $\boldsymbol{D}$ is the electric displacement vector [85].

$$\nabla.(\epsilon \boldsymbol{E}) = q \tag{A.9}$$

$$\nabla.(\epsilon \, \frac{\partial}{\partial t} \, \boldsymbol{E}) = \frac{\partial q}{\partial t} = -\nabla.\boldsymbol{J} = \nabla.(\boldsymbol{J}_s + \sigma \boldsymbol{E}) \tag{A.10}$$

$$\nabla.(\sigma + \, \epsilon \frac{\partial}{\partial t})\, \boldsymbol{E} = -\nabla.\boldsymbol{J}_s \tag{A.11}$$

Since,

$$\boldsymbol{E} \; = \; -\frac{\partial \boldsymbol{A}}{\partial t} - \nabla\phi \tag{A.12}$$

The electric field given in equation (A.12) can be inserted into equation (A.11) to derive the second partial differential equation:

$$\nabla \cdot \left[ \left( \sigma + \epsilon \, \frac{\partial}{\partial t} \right) \nabla \phi \right] + \nabla \cdot \left( \sigma + \epsilon \, \frac{\partial}{\partial t} \right) \, \frac{\partial \boldsymbol{A}}{\partial t} \;=\; \nabla \cdot \boldsymbol{J}_{\mathrm{s}} \qquad \text{(A.13)}$$

The resulting equation in phasor form is as follows [61]:

$$\nabla \cdot \left[ (\sigma + j\omega\epsilon) \, \nabla \phi \right] + \nabla \, (\sigma + j\omega\epsilon) \cdot j\omega \boldsymbol{A} \;=\; \nabla \cdot \boldsymbol{J}_{\mathrm{s}} \qquad \text{(A.14)}$$

The boundary conditions are magnetic insulation along the domain boundary and continuity of magnetic fields at the interior boundaries, as shown in Figure A.1.

$$\boldsymbol{n} \, \times \boldsymbol{A} = 0 \qquad \text{(A.15)}$$

$$\boldsymbol{n} \, \times (\boldsymbol{A}_2 - \boldsymbol{A}_1) = 0 \qquad \text{(A.16)}$$

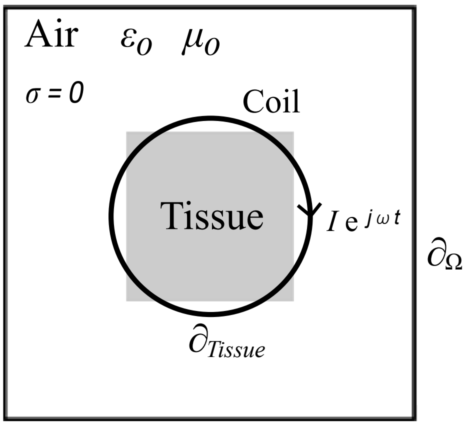

Figure A.1: Diagram to visualize electromagnetic boundary conditions, ($\partial_{Tissue}$ denotes the tissue boundary and $\partial_{\Omega}$ is the outer boundary).

## A.2 Flux Density (With $N$ Circular Loops)

The magnetic flux density at point $P$ can be compared using the outcomes of equation (A.17) with those obtained from simulations to assess the coil's accuracy in magnetics. $P$ denotes a point on the z-axis between $0$ and $L$, as shown in Figure A.2 [131].

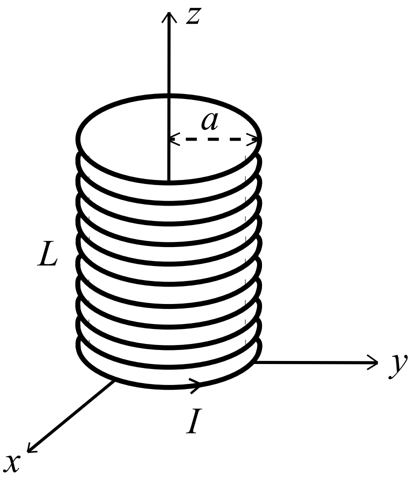

Figure A.2: $N$ parallel loops of radius ($a$) and length ($L$) carrying current ($I$) for calculating the magnetic flux density ($\boldsymbol{B}$).

$$B_z = \frac{\mu_0 N I}{2L}\left(\frac{z}{\left(z^2+a^2\right)^{0.5}} + \frac{L-z}{\left((L-z)^2+a^2\right)^{0.5}}\right) \tag{A.17}$$

When point $P$ was at the midpoint of the z-axis ($L/2$),

$$B_z = \frac{\mu_0 \; N \; I}{2\left(\left(\frac{L}{2}\right)^2 + a^2\right)^{0.5}} \; a_z \tag{A.18}$$

$P$ is positioned on a uniform cylindrical geometry (inner radius: 35.5 mm, outer radius: 42 mm, length: 72.5 mm) in the middle of the z-axis at ($L/2$). When a current with an amplitude of 65 A was applied, the analytical solution was 8.466 mT, considering the average radius (R = 38.75 mm). Employing the same parameters, including a uniform cylindrical geometry comprising 11 loops ($N$) in COMSOL, the result obtained at the exact location was 8.47 mT. These findings indicate a high degree of agreement between analytical and numerical solutions.

## A.3 Tissue Properties and Assumptions (750 kHz)

- In the cases where ($w\epsilon/\sigma$ « 1), the effects of capacitance and displacement currents may be neglected. The effects of capacitance and displacement currents were considered in the breast model ($w\epsilon/\sigma = 0.123$ for the healthy tissue and 0.095 for the tumor). It should be noted that this problem is not considered quasi-static.

- In the cases where ($|kR|$ « 1), propagation effects may be neglected. The propagation term ($e^{-jkR}$) was neglected for the healthy tissue and tumor. $R$ is the distance between the phantom and IR camera, and $k$ is the wave number.
  $k = (w\mu\sigma/2)^{0.5} =$ 0.94.
  $R = 0.15$ m and $|kR| = 0.14$.
- The skin depth ($\delta$) is sufficient to penetrate the breast at the excitation current frequency.
  $\delta = (\pi f \mu\sigma)^{-0.5}$ =1.06 m.
- The wavelength for tumorous tissue in the breast model was 9.6 m.
- The wavelength for healthy tissue in the breast model was 13.5 m.

YÖK

## B. Heat Flow and Temperature Distribution

The heat flow generated by a metabolic heat source, the temperature distribution of a spherical tissue model, the RGB image of the IR camera, and the associated temperature distribution are presented in this section.

### B.1 Heat Flow Created by Metabolic Heat Source

The heat source in Figure B.1 was located at the sphere's center. When the magnitude of heat flow is known, the temperature gradient between various layers and the temperature difference between layers can be calculated.

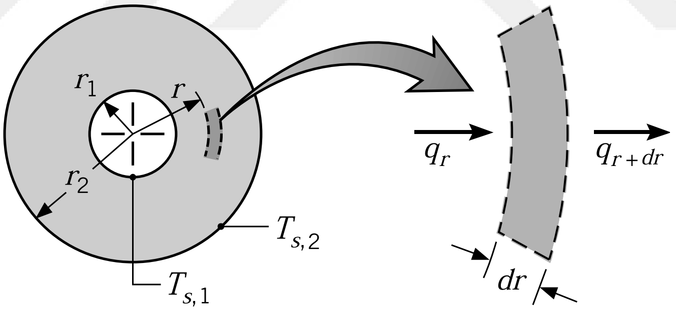

Figure B.1: Heat transfer associated with a metabolic heat source [102].

The one-dimensional heat flow under steady-state conditions can be calculated using the suitable integral form. Where the heat flux $q_r$ is constant ($q_r = q_{r+dr}$) and the surface area is $4\pi r^2$.

$$\frac{-q_r}{4\pi}\int_{r_1}^{r_2}\frac{dr}{r^2}=\int_{T_{s,\,1}}^{T_{s,\,2}}k\left(T\right)dT \tag{B.1}$$

When $k(T)$ remains constant for all the layers given by equation (B.1), the following equation can be derived for the heat flux [102]:

$$q_r=\frac{4\pi k(T_{s,1}-T_{s,2})}{\frac{1}{r_1}-\frac{1}{r_2}} \tag{B.2}$$

The thermal resistance ($R_r$) of each layer was calculated using equation (B.3).

$$R_r=\frac{1}{4\pi k}(\frac{1}{r_1}-\frac{1}{r_2}) \tag{B.3}$$

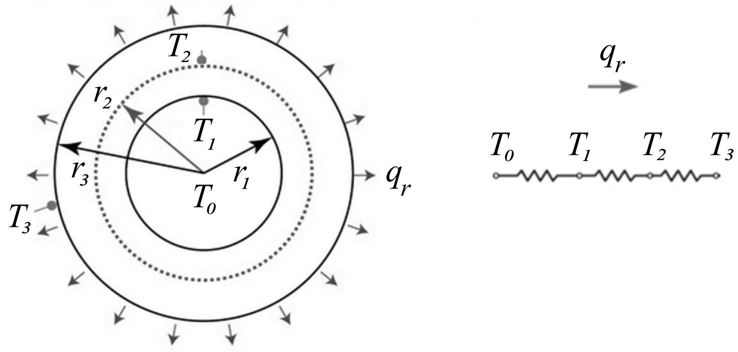

Figure B.2: Temperature distribution of a spherical tumor and its surroundings [102].

The heat source shown in Figure B.2 has a radius of $r_1$ = 15 mm, and the heat flux is $q_r$. The temperatures of the layers were $T_0, T_1, T_2$. Where $R_r$ ($^{\circ}\mathrm{C/W}$) denotes the thermal resistance of the layers. $q_r$ was 25000 $\mathrm{W/m^3}$ as the heat flux. The radius of the spheres is $r_2$ = 25 mm and $r_3$ = 35 mm. $R_r$ was calculated as 7.073 ($^{\circ}\mathrm{C/W}$).

$$Q=q_r\frac{4}{3}\pi r_1^3 \tag{B.4}$$

$$Q=\frac{T_1-T_2}{R_r} \tag{B.5}$$

$(T_1 - T_2) = 2.49$ °C which were analytically calculated. $T_1 = 7.55$ °C, $T_2 = 5.1$ °C, and $(T_1 - T_2) = 2.45$ °C which are numerical results. Based on the results, the correlation between the analytical and numerical solutions was strong.

## B.2 Temperature Distribution of the Tissue

A one-dimensional equation for biological tissues under steady-state conditions can be employed based on Pennes' bio-heat transfer equation. An analytical solution of the bio-heat transfer equation using Bessel's equation can be obtained [132].

$$\rho\, c\, \frac{\partial T}{\partial t} = k\, \nabla^2 T + w_b\, c_b\, (T_a - T) + q_m \tag{B.6}$$

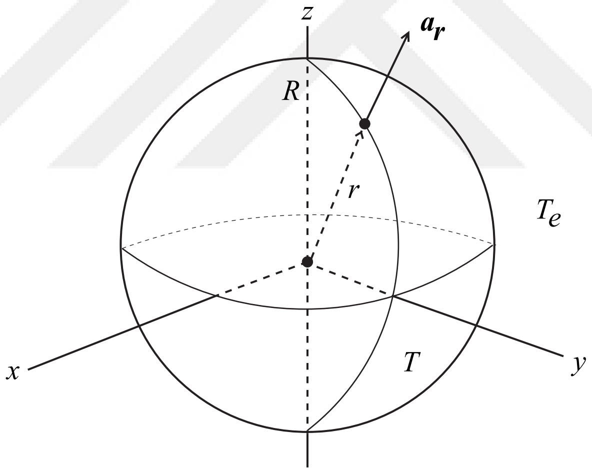

Figure B.3: The illustration depicts spherical coordinates and spherical tissue geometry, which are employed to calculate the temperature of tissue ($T_e$ is the environmental temperature) [133].

Under steady-state conditions, the time-derivative part of the equation (B.6) becomes zero. For spherical coordinates shown in Figure B.3, the equation (B.6) becomes:

$$\frac{1}{r^2}\,\frac{d}{dr}\left(r^2\,\frac{dT}{dr}\right) + \frac{w_b\, c_b}{k}\,(T_a - T) + \frac{q_m}{k} = 0 \tag{B.7}$$

The generalized boundary conditions, for $n = 0$:

$$\frac{dt}{dn} = 0 \tag{B.8}$$

for $n = R$:

$$-k\frac{dt}{dn} = h_a\left(T - T_e\right) \tag{B.9}$$

These two variables are defined as follows:

$$T^* = \frac{T - T_e}{T_a - T_e} \tag{B.10}$$

$$r^* = \frac{r}{R} \tag{B.11}$$

$T_e$ is the environmental temperature, and $T_a$ is the arterial temperature. When equation (B.7) is solved, the temperature distribution in equation (B.12) is determined [132].

$$T = T_e + \left(T_a - T_e\right)\frac{\beta}{\alpha}\left(1 - \frac{h_a^*}{\sqrt{\alpha}\, I_{\frac{3}{2}}\left(\sqrt{\alpha}\right) + h_a^*\, I_{\frac{1}{2}}\left(\sqrt{\alpha}\right)}\frac{I_{\frac{1}{2}}\left(\sqrt{\alpha}\, r^*\right)}{\sqrt{r^*}}\right) \tag{B.12}$$

$$\alpha = w_b^* = \frac{w_b c_b\, R^2}{k} \tag{B.13}$$

$$h_a^* = \frac{h_a\, R}{k} \tag{B.14}$$

$$q_m^* = \frac{q_m\, R^2}{k\ \left(T_a - T_e\right)} \tag{B.15}$$

$$\beta = w_b^* + q_m^* \tag{B.16}$$

*I*, is a modified Bessel function of the first kind with orders of $(1/2)$ and $(3/2)$. The parameters, $w_b = 0.002\ \mathrm{s}^{-1}$, $R = 0.4$ m, $q_m = 700\ \mathrm{W/m}^3$, $T_a = 310\ ^{\circ}\mathrm{C}$ and $T_e = 298\ ^{\circ}\mathrm{C}$ were used in the numerical study. $T$ (at $r = 0.02$) was calculated as 36.8 $^{\circ}\mathrm{C}$ with the analytical solution and 36.9 $^{\circ}\mathrm{C}$ with the numerical solution.

### B.3 IR Camera RGB Image and Temperature Distribution

Figure B.4 illustrates the temperature distribution obtained using MATLAB [120]. Thermal images in RGB color acquired from FLIR Studio were cropped and processed with a temperature color bar that displayed the minimum and maximum temperature values in RGB color [129]. This graphical user interface enabled the formation of a grayscale temperature distribution.

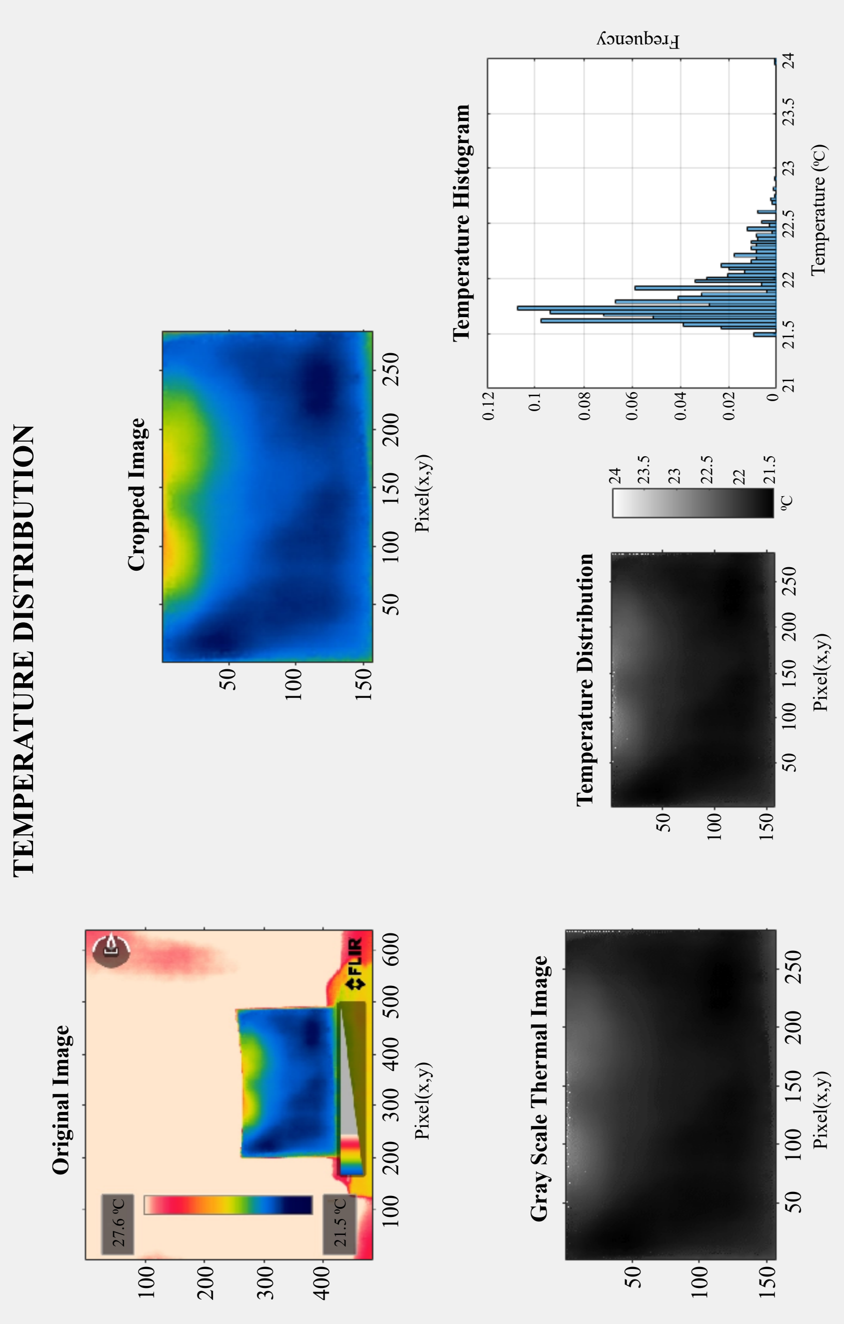

Figure B.4: From left to right in the graphical interface: (a) The Original thermal image is shown in RGB color with a min-max color bar. (b) Cropped image. (c) The thermal image is displayed on a grayscale. (d) Image illustrating the temperature distribution in grayscale. (e) Graphical representation of temperature histogram.

# CURRICULUM VITAE

## PERSONAL INFORMATION

**Surname, Name:** Tanrıverdi, Volkan
**Nationality:** Turkish (TC)

## EDUCATION

| Degree | Institution | Year of Grad. |
|---|---|---|
| M.S. | METU Electrical–Electronics Engineering | 2006 |
| B.S. | Anadolu Uni. Business Administration | 2016 |
| B.S. | Gazi Uni. Electrical–Electronics Engineering | 2003 |
| High School | Malatya Science High School | 1999 |

## PROFESSIONAL EXPERIENCE

| Year | Place | Enrollment |
|---|---|---|
| 2004-2005 | TPAO | Engineer |
| 2005-2006 | METU | Engineer |
| 2006-Present | TCMB | Senior Engineer |

## PUBLICATIONS

### Journals

V. Tanrıverdi and N. G. Gençer, “Induced current electro-thermal imaging for breast tumor detection: A numerical and experimental study,” *Annals of Biomedical Engineering*, (Accepted: 5 January 2024).

### Conference Papers

V. Tanrıverdi and N. G. Gençer, “Induced current thermal imaging in breast cancer detection,” *IEEE SIU Signal Processing and Communication Applications Conference*, pp. 1–4, 2021.

V. Tanrıverdi and N. G. Gençer, “Phantom and solenoid coil development for induced current electro-thermal imaging,” *IEEE Tıptekno Medical Technologies Congress*, pp. 1–4, 2021.